

AD-A243 889



1

**DTIC**  
**ELECTE**  
**JAN 06 1992**  
**S D D**

This document has been approved  
for public release and sale; its  
distribution is unlimited.

DEPARTMENT OF THE AIR FORCE  
AIR UNIVERSITY  
**AIR FORCE INSTITUTE OF TECHNOLOGY**

92-00189



Wright-Patterson Air Force Base, Ohio

02 1 2 123

AFIT/EN/ENG/91D-40

DTIC  
ELECTE  
JAN 06 1992  
S D D

INVESTIGATION OF THE EFFECTS OF  
AEROELASTIC DEFORMATIONS ON THE  
RADAR CROSS SECTION OF  
AIRCRAFT

THESIS

Samuel D. McKenzie, Captain, USAF

GE  
AFIT/EN/ENG/91D-40

Approved for public release; distribution unlimited

1

INVESTIGATION OF THE EFFECTS OF AEROELASTIC DEFORMATIONS ON  
THE RADAR CROSS SECTION OF AIRCRAFT

THESIS

Presented to the Faculty of the School of Engineering  
of the Air Force Institute of Technology  
Air University  
In Partial Fulfillment of the  
Requirements for the Degree of  
Master of Science in Electrical Engineering

Samuel D. McKenzie  
Captain, USAF

December 1991



Accession For	
NTIS CRA&I	<input checked="checked" type="checkbox"/>
DTIC TAB	<input type="checkbox"/>
Unannounced	<input type="checkbox"/>
Justification	
By	
Distribution /	
Availability Codes	
Dist	Avail and/or Special
A-1	

Approved for public release; distribution unlimited

## Preface

This work was sponsored by the 6585th Test Group/RX, Holoman AFB NM, and ASD/YS, Wright-Patterson AFB OH. I would like to thank both organizations for their support. The purpose of this study was to model changes in the radar cross section (RCS) of several Air Force aircraft when structurally deformed by the dynamics of flight. The need for this type of modeling stems from the fact that dynamic measurement ranges are expensive and limited in terms of availability.

In performing this study and writing this thesis, I have had a lot of help from others. I am indebted to my thesis advisor, Dr. Andrew Terzuoli, for his guidance and support throughout this effort. I would also like to thank my thesis committee members, Dr. Peter Torvik, Capt Howard Gans and Capt Bryon Welsh for their continued patience and advice. A special debt of gratitude is owed to Mr. Alan Brown and Mr. Jerry Akins, of Lockheed Corporation and the Lockheed-Georgia Company respectively, for their assistance in obtaining the C-5A structural models, and also to Mr. Eli Collas of SA-ALC/LADD for his help in obtaining the T-38 structural model. And finally, I wish to thank my wife Diana for her understanding and complete support during those many hours I had to spend away from home doing research.

Samuel D. McKenzie

## Table of Contents

Preface .....	ii
List of Figures .....	iii
Abstract .....	xii
I. Introduction .....	1.1
1.1 Background .....	1.1
1.2 Problem .....	1.2
1.3 Scope .....	1.3
1.4 Summary of Current Knowledge .....	1.3
1.5 Approach .....	1.6
1.6 Development .....	1.6
II. Structural Analysis .....	2.1
2.1 Introduction .....	2.1
2.2 NASTRAN .....	2.1
2.2.1 Finite Element Analysis .....	2.1
2.2.2 Linear Static Analysis .....	2.2
2.2.3 Input/Output Files .....	2.7
2.3 Static Structural Analysis .....	2.9
2.3.1 T-38 Airframe .....	2.9
2.3.2 C-5A Airframe .....	2.11
2.4 Summary .....	2.14
III. Radar Cross Section Analysis .....	3.1
3.1 Introduction .....	3.1
3.2 RCS Analysis Software .....	3.1
3.2.1 Uniform Geometric Theory of Diffraction .....	3.2
3.3 Data Processing .....	3.7
3.4 Summary .....	3.13
IV. Results .....	4.1
4.1 Introduction .....	4.1
4.2 Methodology .....	4.1
4.2.1 T-38 Modeling .....	4.1
4.2.2 C-5A Modeling .....	4.4
4.2.3 General Analysis Methodology .....	4.8
4.3 T-38 Analysis Results .....	4.8
4.4 C-5A Analysis Results .....	4.16
4.4.1 Positive Symmetric Maneuver .....	4.16

4.4.2 Negative Symmetric Maneuver .....	4.21
4.5 Summary .....	4.26
V. Conclusions and Recommendations .....	5.1
5.1 Introduction .....	5.1
5.2 Conclusions .....	5.1
5.3 Recommendations .....	5.3
5.4 Summary .....	5.4
Appendix A .....	A.6
Appendix B .....	B.1
Appendix C .....	C.1
Appendix D .....	D.1
Bibliography .....	BIB.1
Vita .....	V.16

## List of Figures

Figure 2.1. Common Element Types .....	2.2
Figure 2.2. Single rod element. ....	2.3
Figure 2.3. Two rod elements to be joined. ....	2.5
Figure 2.4. T-38 Structural Model .....	2.10
Figure 2.5. T-38 Structural Deformations .....	2.11
Figure 2.6. C-5A Structural Wing Model .....	2.12
Figure 2.7. C-5A in a positive symmetric maneuver. ....	2.13
Figure 2.8. C-5A in a negative symmetric maneuver. ....	2.13
Figure 2.9. A Typical Wing Station .....	2.14
Figure 3.1. Conducting Half Plane .....	3.3
Figure 3.2. Conducting Plane Wedge [13] .....	3.4
Figure 3.3. Computed Raw RCS Data for a T-38 Airframe .....	3.8
Figure 3.4. Medianized RCS Data for a T-38 .....	3.9
Figure 3.5. Medianized and Averaged RCS of a T-38 Airframe .....	3.10
Figure 3.6. Comparison of Non-deformed versus Deformed Raw RCS Data for a T-38 Airframe .....	3.11
Figure 3.7. Comparison of the Averaged Data for the Non-deformed Versus Deformed T-38 Airframe .....	3.11
Figure 3.8. Fractional (Delta) Change Between the Non-deformed and Deformed T-38 Airframe .....	3.12
Figure 4.1. RCS Model for the T-38 Airframe .....	4.2
Figure 4.2. RCS Model of the C-5A Airframe .....	4.3

Figure 4.3. Deformed Versus Non-deformed RCS Model of the T-38 .....	4.5
Figure 4.4 (a). Deformed (PSM) Versus Non-deformed RCS Model of the C-5A ..	4.6
Figure 4.4 (b). Deformed (NSM) Versus Non-deformed RCS Model of the C-5A .	4.7
Figure 4.5. Angular Dimensions for the T-38 RCS Model .....	4.9
Figure 4.6. Percent Change Between the Non-deformed and Deformed T-38 Airframe for Elevations of 0, 10, 20 and 30 Degrees Respectively. Vertical Polarization .....	4.11
Figure 4.7. Percent Change Between the Non-deformed and Deformed T-38 Airframes for Elevations of 0, -10, -20 and -30 Degrees Respectively. Vertical Polarization .....	4.13
Figure 4.8. Percent Change Between the Non-deformed and Deformed T-38 Airframes for Elevations of 0, 10, 20 and 30 Degrees Respectively. Horizontal Polarization .....	4.14
Figure 4.9. Percent Change Between the Non-deformed and Deformed T-38 Airframes for Elevations of 0, -10, -20 and -30 Degrees Respectively. Horizontal Polarization .....	4.15
Figure 4.10. Angular Dimensions of the C-5A RCS Model .....	4.17
Figure 4.11. Percent Change Between the Non-deformed and Deformed C-5A Airframes for Elevations of 0, 10 ,20 and 30 Degrees Respectively. PSM : Vertical Polarization .....	4.18
Figure 4.12. Percent Change Between the Non-deformed and Deformed C-5A Airframes for Elevations of 0, -10, -20 and -30 Degrees Respectively. PSM : Vertical Polarization .....	4.19
Figure 4.13. Percent Change Between the Non-deformed and Deformed C-5A Airframes for Elevations of 0, 10, 20 and 30 Degrees Respectively. PSM : Horizontal Polarization .....	4.20
Figure 4.14. Percent Change Between the Non-deformed and Deformed C-5A Airframes for Elevations of 0, -10, -20 and -30 Degrees Respectively. PSM : Horizontal Polarization .....	4.21
Figure 4.15. Percent Change Between the Non-deformed and Deformed C-5A Airframes for Elevations of 0, 10 ,20 and 30 Degrees Respectively. NSM : Vertical Polarization .....	4.22



Figure 4.16. Percent Change Between the Non-deformed and Deformed C-5A Airframes for Elevations of 0, -10, -20 and -30 Degrees Respectively. NSM : Vertical Polarization .....	4.23
Figure 4.17. Percent Change Between the Non-Deformed and Deformed C-5A Airframes for Elevations of 0, 10, 20 and 30 Degrees Respectively. NSM : Horizontal Polarization .....	4.25
Figure 4.18. Percent Change Between the Non-deformed and Deformed C-5A Airframes for Elevations of 0, -10, -20 and -30 Degrees Respectively. NSM : Horizontal Polarization .....	4.26
Figure A.1. Medianized, Averaged RCS Data Comparisons Between the Non-deformed (solid line) and Deformed (dashed line) T-38 Airframes for: (a) Vertical Polarization, and (b) Horizontal Polarization. 0 Degrees Elevation .	A.2
Figure A.2. Medianized, Averaged RCS Data Comparisons Between the Non-deformed (solid line) and Deformed (dashed line) T-38 Airframes for: (a) Vertical Polarization, and (b) Horizontal Polarization. 10 Degrees Elevation .....	A.3
Figure A.3. Medianized, Averaged RCS Data Comparisons Between the Non-deformed (solid line) and Deformed (dashed line) T-38 Airframes for: (a) Vertical Polarization, and (b) Horizontal Polarization. 20 Degrees Elevation .....	A.4
Figure A.4. Medianized, Averaged RCS Data Comparisons Between the Non-deformed (solid line) and Deformed (dashed line) T-38 Airframes for: (a) Vertical Polarization, and (b) Horizontal Polarization. 30 Degrees Elevation .....	A.5
Figure A.5. Medianized, Averaged RCS Data Comparisons Between the Non-deformed (solid line) and Deformed (dashed line) T-38 Airframes for: (a) Vertical Polarization, and (b) Horizontal Polarization. -10 Degrees Elevation .....	A.6
Figure A.6. Medianized, Averaged RCS Data Comparisons Between the Non-deformed (solid line) and Deformed (dashed line) T-38 Airframes for: (a) Vertical Polarization, and (b) Horizontal Polarization. -20 Degrees Elevation .....	A.7
Figure A.7. Medianized, Averaged RCS Data Comparisons Between the Non-deformed (solid line) and Deformed (dashed line) T-38 Airframes for: (a) Vertical Polarization, and (b) Horizontal Polarization. -30 Degrees Elevation .....	A.8

Figure B.1. Medianized, Averaged RCS Data Comparisons for the Non-deformed (solid line) versus Deformed (dashed line) C-5A Airframes for: (a) Vertical Polarization, and (b) Horizontal Polarization. PSM : 0 Degrees Elevation . .	B.2
Figure B.2. Medianized, Averaged RCS Data Comparisons for the Non-deformed (solid line) versus Deformed (dashed line) C-5A Airframes for: (a) Vertical Polarization, and (b) Horizontal Polarization. PSM : 10 Degrees Elevation .	B.3
Figure B.3. Medianized, Averaged RCS Data Comparisons for the Non-deformed (solid line) versus Deformed (dashed line) C-5A Airframes for: (a) Vertical Polarization, and (b) Horizontal Polarization. PSM : 20 Degrees Elevation .	B.4
Figure B.4. Medianized, Averaged RCS Data Comparisons for the Non-deformed (solid line) versus Deformed (dashed line) C-5A Airframes for: (a) Vertical Polarization, and (b) Horizontal Polarization. PSM : 30 Degrees Elevation .	B.5
Figure B.5. Medianized, Averaged RCS Data Comparisons for the Non-deformed (solid line) versus Deformed (dashed line) C-5A Airframes for: (a) Vertical Polarization, and (b) Horizontal Polarization. PSM : -10 Degrees Elevation . . . . .	B.6
Figure B.6. Medianized, Averaged RCS Data Comparisons for the Non-deformed (solid line) versus Deformed (dashed line) C-5A Airframes for: (a) Vertical Polarization, and (b) Horizontal Polarization. PSM : -20 Degrees Elevation . . . . .	B.7
Figure B.7. Medianized, Averaged RCS Data Comparisons for the Non-deformed (solid line) versus Deformed (dashed line) C-5A Airframes for: (a) Vertical Polarization, and (b) Horizontal Polarization. PSM : -30 Degrees Elevation . . . . .	B.8
Figure B.8. Medianized, Averaged RCS Data Comparisons for the Non-deformed (solid line) versus Deformed (dashed line) C-5A Airframes for: (a) Vertical Polarization, and (b) Horizontal Polarization. NSM : 0 Degrees Elevation . .	B.9
Figure B.9. Medianized, Averaged RCS Data Comparisons for the Non-deformed (solid line) versus Deformed (dashed line) C-5A Airframes for: (a) Vertical Polarization, and (b) Horizontal Polarization. NSM : 10 Degrees Elevation	B.10
Figure B.10. Medianized, Averaged RCS Data Comparisons for the Non-deformed (solid line) versus Deformed (dashed line) C-5A Airframes for: (a) Vertical Polarization, and (b) Horizontal Polarization. NSM : 20 Degrees Elevation	B.11

Figure B.11. Medianized, Averaged RCS Data Comparisons for the Non-deformed (solid line) versus Deformed (dashed line) C-5A Airframes for: (a) Vertical Polarization, and (b) Horizontal Polarization. NSM : 30 Degrees Elevation	B.12
Figure B.12. Medianized, Averaged RCS Data Comparisons for the Non-deformed (solid line) versus Deformed (dashed line) C-5A Airframes for: (a) Vertical Polarization, and (b) Horizontal Polarization. NSM : -10 Degrees Elevation	B.13
Figure B.13. Medianized, Averaged RCS Data Comparisons for the Non-deformed (solid line) versus Deformed (dashed line) C-5A Airframes for: (a) Vertical Polarization, and (b) Horizontal Polarization. NSM : -20 Degrees Elevation	B.14
Figure B.14. Medianized, Averaged RCS Data Comparisons for the Non-deformed (solid line) versus Deformed (dashed line) C-5A Airframes for: (a) Vertical Polarization, and (b) Horizontal Polarization. NSM : -30 Degrees Elevation	B.15
Figure C.1. Raw RCS of a T-38 Aircraft for: (a) Non-deformed Airframe, and (b) Deformed Airframe. 0 Degrees Elevation : Vertical Polarization	C.2
Figure C.2. Raw RCS of a T-38 Aircraft for: (a) Non-deformed Airframe, and (b) Deformed Airframe. 10 Degrees Elevation : Vertical Polarization	C.3
Figure C.3. Raw RCS of a T-38 Aircraft for: (a) Non-deformed Airframe, and (b) Deformed Airframe. 20 Degrees Elevation : Vertical Polarization	C.4
Figure C.4. Raw RCS of a T-38 Aircraft for: (a) Non-deformed Airframe, and (b) Deformed Airframe. 30 Degrees Elevation : Vertical Polarization	C.5
Figure C.5. Raw RCS of a T-38 Aircraft for: (a) Non-deformed Airframe, and (b) Deformed Airframe. -10 Degrees Elevation : Vertical Polarization	C.6
Figure C.6. Raw RCS of a T-38 Aircraft for: (a) Non-deformed Airframe, and (b) Deformed Airframe. -20 Degrees Elevation : Vertical Polarization	C.7
Figure C.7. Raw RCS of a T-38 Aircraft for: (a) Non-deformed Airframe, and (b) Deformed Airframe. -30 Degrees Elevation : Vertical Polarization	C.8
Figure C.8. Raw RCS of a T-38 Aircraft for: (a) Non-deformed Airframe, and (b) Deformed Airframe. 0 Degrees Elevation : Horizontal Polarization	C.9

Figure C.9. Raw RCS of a T-38 Aircraft for: (a) Non-deformed Airframe, and (b) Deformed Airframe. 10 Degrees Elevation : Horizontal Polarization . . . . .	C.10
Figure C.10. Raw RCS of a T-38 Aircraft for: (a) Non-deformed Airframe, and (b) Deformed Airframe. 20 Degrees Elevation : Horizontal Polarization . . . . .	C.11
Figure C.11. Raw RCS of a T-38 Aircraft for: (a) Non-deformed Airframe, and (b) Deformed Airframe. 30 Degrees Elevation : Horizontal Polarization . . . . .	C.12
Figure C.12. Raw RCS of a T-38 Aircraft for: (a) Non-deformed Airframe, and (b) Deformed Airframe. -10 Degrees Elevation : Horizontal Polarization . . . . .	C.13
Figure C.13. Raw RCS of a T-38 Aircraft for: (a) Non-deformed Airframe, and (b) Deformed Airframe. -20 Degrees Elevation : Horizontal Polarization . . . . .	C.14
Figure C.14. Raw RCS of a T-38 Aircraft for: (a) Non-deformed Airframe, and (b) Deformed Airframe. -30 Degrees Elevation : Horizontal Polarization . . . . .	C.15
Figure D.1. Raw RCS of a C-5A Aircraft for: (a) Non-deformed Airframe, (b) PSM deformation, and (c) NSM deformation. 0 Degrees Elevation : Vertical Polarization . . . . .	D.2
Figure D.2. Raw RCS of a C-5A Aircraft for: (a) Non-deformed Airframe, (b) PSM deformation, and (c) NSM deformation. 10 Degrees Elevation : Vertical Polarization . . . . .	D.3
Figure D.3. Raw RCS of a C-5A Aircraft for: (a) Non-deformed Airframe, (b) PSM deformation, and (c) NSM deformation. 20 Degrees Elevation : Vertical Polarization . . . . .	D.4
Figure D.4. Raw RCS of a C-5A Aircraft for: (a) Non-deformed Airframe, (b) PSM deformation, and (c) NSM deformation. 30 Degrees Elevation : Vertical Polarization . . . . .	D.5
Figure D.5. Raw RCS of a C-5A Aircraft for: (a) Non-deformed Airframe, (b) PSM deformation, and (c) NSM deformation. -10 Degrees Elevation : Vertical Polarization . . . . .	D.6
Figure D.6. Raw RCS of a C-5A Aircraft for: (a) Non-deformed Airframe, (b) PSM deformation, and (c) NSM deformation. -20 Degrees Elevation : Vertical Polarization . . . . .	D.7
Figure D.7. Raw RCS of a C-5A Aircraft for: (a) Non-deformed Airframe, (b) PSM deformation, and (c) NSM deformation. -30 Degrees Elevation : Vertical Polarization . . . . .	D.8

Figure D.8. Raw RCS of a C-5A Aircraft for: (a) Non-deformed Airframe, (b) PSM deformation, and (c) NSM deformation. 0 Degrees Elevation : Horizontal Polarization .....	D.9
Figure D.9. Raw RCS of a C-5A Aircraft for: (a) Non-deformed Airframe, (b) PSM deformation, and (c) NSM deformation. 10 Degrees Elevation : Horizontal Polarization .....	D.10
Figure D.10. Raw RCS of a C-5A Aircraft for: (a) Non-deformed Airframe, (b) PSM deformation, and (c) NSM deformation. 20 Degrees Elevation : Horizontal Polarization .....	D.11
Figure D.11. Raw RCS of a C-5A Aircraft for: (a) Non-deformed Airframe, (b) PSM deformation, and (c) NSM deformation. 30 Degrees Elevation : Horizontal Polarization .....	D.12
Figure D.12. Raw RCS of a C-5A Aircraft for: (a) Non-deformed Airframe, (b) PSM deformation, and (c) NSM deformation. -10 Degrees Elevation : Horizontal Polarization .....	D.13
Figure D.13. Raw RCS of a C-5A Aircraft for: (a) Non-deformed Airframe, (b) PSM deformation, and (c) NSM deformation. -20 Degrees Elevation : Horizontal Polarization .....	D.14
Figure D.14. Raw RCS of a C-5A Aircraft for: (a) Non-deformed Airframe, (b) PSM deformation, and (c) NSM deformation. -30 Degrees Elevation : Horizontal Polarization .....	D.15

Abstract

The effects of aeroelastic deformations on the radar cross section (RCS) of a T-38 trainer jet and a C-5A transport aircraft are examined and characterized. Realistic representations of structural wing deformations are obtained from a mechanical/computer aided design software package called "NASTRAN". NASTRAN is used to evaluate the structural parameters of the aircraft as well as the restraints and loads associated with realistic flight conditions. Geometries for both the non-deformed and deformed airframes are obtained from the NASTRAN models and translated into RCS models. The RCS is analyzed using a numerical modeling code called the "Radar Cross Section - Basic Scattering Code, version 2" which was developed at Ohio State University and is based on the uniform geometric theory of diffraction. The code is used to analyze the effects of aeroelastic deformations on the RCS of the aircraft by comparing the computed RCS representing the deformed airframe to that of the non-deformed airframe and characterizing the differences between them.

# INVESTIGATION OF THE EFFECTS OF AEROELASTIC DEFORMATIONS ON THE RADAR CROSS SECTIONS OF AIRCRAFT

## I. Introduction

### 1.1 Background

With increased emphasis on the application of low observables technology to military aircraft, the ability to accurately predict the radar cross section (RCS) of those aircraft in a dynamic environment has become increasingly important. Accurate predictions of the dynamic RCS of an aircraft must include modeling variations in aspect angle and frequency, as well as any other variables imposed by the dynamics of flight which might effect or alter its RCS, such as aeroelastic deformations of the airframe. "Radar cross section is very sensitive to the geometry of the vehicle. Consequently, any changes in the vehicle shape may change its RCS properties" [1:2]. These variations in radar cross section could severely limit the aircraft's survivability if their effects are unknown or unaccounted for.

Capt Allan Beck, a graduate of the Air Force Institute of Technology's School of Engineering, investigated the effects of static aeroelastic deformations on the predicted radar cross section of typical aircraft wings [1]. Beck developed analytical models to predict realistic twisting and bending deformations of both swept and unswept wings. He then analyzed the changes

in RCS due to those deformations. He concluded that

... a wings internal properties and structural behavior can affect, adversely or beneficially, its radar cross section. RCS designers and analysts must be aware of the effect aeroelastic deformations have on the RCS predictions and include them in the prediction of the total signature. [1:120]

In Beck's investigation, he used numerical modeling techniques to study the RCS properties of generic wings isolated in space. Accurate predictions of the radar cross section of complex structures such as aircraft using numerical modeling techniques is more difficult. The many scattering mechanisms on an aircraft include various flat and curved surfaces, antenna apertures, engine cavities and a variety of structural materials. In addition, the numerical model must be able to interpret a geometrical description of the vehicle giving the size, shape, and locations of the scattering elements and their orientation with respect to the radar [2:253]. Unfortunately, none of the numerical models currently available can account for all of these scattering mechanisms. However, to investigate the effects of aeroelastic deformations on an aircraft's RCS, many of these mechanisms can be assumed constant and ignored. This thesis will extend Beck's study by investigating the effects of aeroelastic deformations on the radar cross section of complete aircraft structures.

## 1.2 Problem

Determine the effects of aeroelastic deformations on an aircraft radar cross section under specified conditions of pitch, yaw and roll representing a realistic flight scenario.



### 1.3 Scope

This thesis studied the effects of realistic aeroelastic deformations on the RCS of two typical Air Force aircraft. The study was limited to examining the net change in RCS between the non-deformed and deformed airframes. No attempt was made to model the RCS of the aircraft accurately, however, the aircraft models used in the RCS analysis were dimensionally correct. Realistic aeroelastic deformations were obtained from structural computer aided design (CAD) characterizations. The study was limited to static deformations which were representative of realistic flight conditions.

### 1.4 Summary of Current Knowledge

There have been a number of numerical modeling techniques developed in recent years for predictions of electromagnetic scattering. Unfortunately, few can accurately predict the RCS of an entire aircraft over the full range of aspect and elevation angles. However, some of the more recent numerical models do look promising. The following review will address some of the recently published research efforts.

Engineers at Boeing Aerospace Company have developed a high frequency numerical modeling computer coded called "RECOTA" which stands for "return from complex target" [3:722]. Nazih Youssef with Radar Cross Section Technology, Boeing Aerospace Company, describes the code as follows:

The code utilizes a computer-aided design package for modeling target geometry in terms of facets and wedges. It is based on physical

optics, physical theory of diffraction, ray tracing, and semiempirical formulations, and it accounts for shadowing, multiple scattering, and discontinuities for monostatic calculations. [3:722]

In his paper, Youssef demonstrates how RECOTA "may be utilized to provide an effective computational tool to aid in the analysis and design of complex targets from the RCS point of view" [3:722]. He concludes with "the overall predictions of RECOTA are in good agreement with range measurements as well as with moment method predictions" [3:733].

The Ohio State University Electrosience Laboratory (OSU-ESL) has also developed a high frequency RCS numerical modeling code based on the uniform geometrical theory of diffraction. "The uniform geometrical theory of diffraction (UTD) is a high-frequency asymptotic solution that follows a scattering center interpretation of the returns from complex shapes" [4:703]. UTD is an extension of the geometrical theory of diffraction (GTD) developed by Keller, which is a ray-based solution which corrects geometrical optics [4:703]. The authors describe the advantage of UTD as its ability to handle large sized objects efficiently. Complex objects can be systematically built up using the major local scattering centers based on the diffraction coefficients [4:704]. Newman and Marhefka also note that "the disadvantages of UTD hinge on the fact that it is assumed a priori that the most important mechanisms are known. If some terms are left out on purpose or by oversight, the accuracy of the total solution may diverge" [4:703].

Diverging from the more traditional high frequency asymptotic solutions to complex target electromagnetic scattering problems, engineers at Rockwell International have been researching another approach.

A novel time-domain differential solver for Maxwells equations utilizing proven numerical algorithms of computational fluid dynamics (CFD) has been developed and applied to solve the two-dimensional transverse magnetic and transverse electric wave equations. [5:720]

The approach taken at Rockwell was to apply the same numerical algorithms that have proven successful in solving the time dependent equations of fluid dynamics to electromagnetic problems [5:709]. The authors state that

... computational algorithms to solve these nonlinear equations of fluid dynamics have progressed rapidly over the last 20 years, and many of these computational fluid dynamics (CFD) methods are directly applicable to computational electromagetics (CEM) in solving Maxwell's equations. [5:709]

Another technique is being researched by A. Taflove at Northwestern University and K. Umashankar at the University of Illinois. It is called the finite-difference time-domain (FD-TD) method for numerical modeling of electromagnetic interactions. Taflove and Umashankar attempt to demonstrate that

... recent advances in FD-TD modeling concepts and software implementation, combined with advances in supercomputer technology, have expanded the scope, accuracy, and speed of FD-TD modeling to the point where it may be the preferred choice for scattering problems involving complex, electrically large, three dimensional structures. [6:682]

FD-TD is a direct solution to Maxwell's time-dependent curl equations. "It applies simple second-order accurate central-difference approximations for the space and time derivatives of the electric and magnetic fields directly to the

respective differential operators of the curl equations" [6:683]. Taflove and Umashankar conclude that

In all cases studied to date where rigorous analytical, code-to-code, or experimental validations were possible, FD-TD predictive data for near fields and RCS were in excellent agreement with the benchmark data. [6:697]

### 1.5 Approach

Realistic aeroelastic deformations were obtained from a mechanical modeling/CAD software package called "NASTRAN." NASTRAN was used to evaluate the structural parameters of the aircraft as well as the restraints and loads associated with realistic flight conditions. Part of the NASTRAN output file includes the airframe deformation data. SDRC's "IDEAS", a graphical CAD package, was used to post-process the NASTRAN output and obtain both the non-deformed and deformed geometries in a form which could be converted into a model for the RCS code.

The numerical modeling code chosen to analyze the RCS was RCSBSC2. As stated in section 1.4, this code was developed at OSU-ESL and is based on the Uniform Geometrical Theory of Diffraction. Both the non-deformed and deformed geometry files obtained from IDEAS were used to create input files for RCSBSC2. The deformed aircraft RCS was then compared to the non-deformed RCS and the differences between them characterized.

### 1.6 Development

The structure of this thesis is outlined below:

Chapter II presents the structural analysis theory and a general discussion on the use of the NASTRAN mechanical CAD software. A review of finite element analysis theory is included.

Chapter III presents a review of radar cross section analysis theory. Included are discussions on the uniform geometric theory of diffraction and statistical post-processing methods used to reduce the RCS data.

Chapter IV provides the RCS analysis for the deformed versus non-deformed aircraft. The RCS was computed at various aspect angles for each deformation imposed, and any variations in the RCS are analyzed.

Chapter V presents the conclusions of this study and recommendations for further research.

## II. Structural Analysis

### 2.1 Introduction

This chapter presents the structural analysis of the airframes modeled. First, an introduction to NASTRAN is presented, including a brief discussion of finite element theory and its application to linear static analysis. Then the static structural analysis of the airframes modeled is presented and discussed.

### 2.2 NASTRAN

To obtain airframe deformations which were representative of realistic structural loading, a general purpose structural analysis program called "NASTRAN" (NASTRAN is a registered trademark of the National Aeronautics and Space Administration) was used. NASTRAN can solve both linear and nonlinear static and dynamic structural problems. For the purposes of this thesis, NASTRAN was used to solve linear, static structural problems associated with the wing loading of two airframes: a T-38 Talon trainer jet and a C-5A Galaxy transport. The T-38 is a small, compact jet and was chosen to represent rigid body airframes. The C-5A represents large flexible airframes.

2.2.1 Finite Element Analysis. NASTRAN solves structural problems via finite element theory. A finite element can be defined as: "a hypothetical subdivision of a structure or system possessing a regular shape which can be analyzed" [7:1]. Some examples of common elements are shown in Figure 2.1. Using the finite element method involves: (1) subdividing the structure to

be analyzed into an assemblage of these finite elements, all connected by a finite number of discrete points or nodes; (2) developing an analytical model of each individual element, often with concepts from classical mechanics; and (3) algebraically summing each finite element to form the total solution.

This approach can greatly simplify complex structural analysis problems.

"Restated, the finite element method is one wherein the difficulty of mathematically solving large complex geometric problems (say doing the stress analysis of a Boeing 747) is transformed from a differential equation approach to an algebraic problem, wherein the building blocks or finite elements have all the complex equations solved for their simple shape (say a triangle, rod, beam, etc). [8:4]

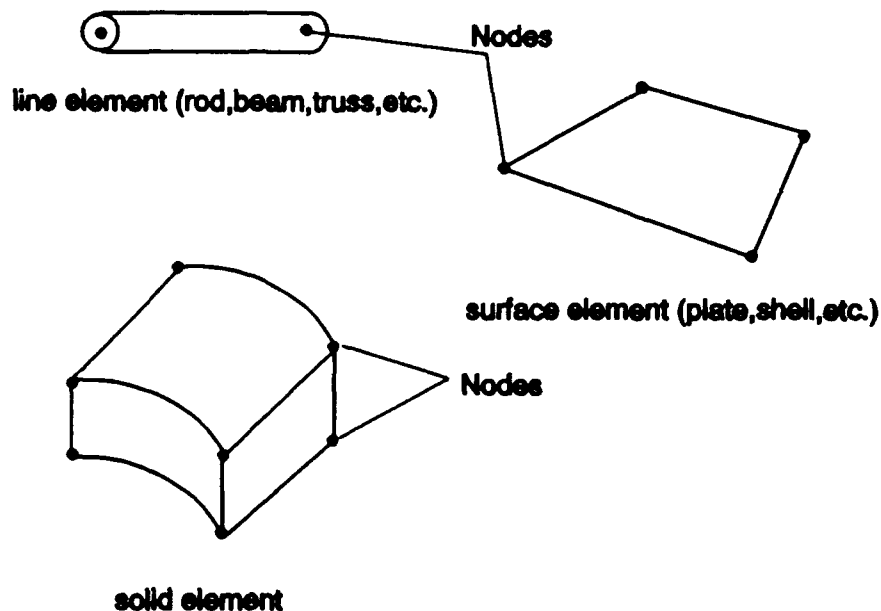


Figure 2.1. Common Element Types

**2.2.2 Linear Static Analysis.** Modern finite element theory is based on the use of the stiffness method for structural analysis. "An element is viewed as a conductor of forces from one node to another and the stiffness is a measure

of how much force can be conducted per unit nodal displacement" [7:15]. A convenient way to introduce the concepts involved in this stiffness method (the way most texts on the subject introduce it) is through an example. Consider the uniform, linearly elastic rod element shown in Figure 2.2. The element has nodal forces  $(f_1, f_2)$  and nodal displacements  $(u_1, u_2)$  associated with each end and is of constant area.

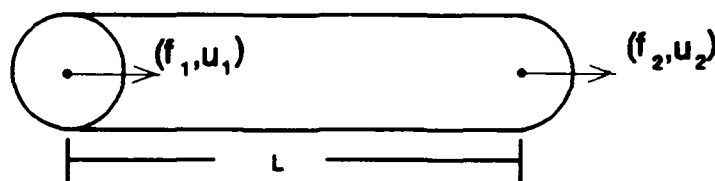


Figure 2.2. Single rod element.

"Linear static analysis assumes that stress is proportional to strain (i.e. the materials follow Hooke's law) for the entire load history" [8:26]. Hooke's law for the one-dimensional (1-D) rod is given by

$$\sigma_x(x) = E \epsilon_x(x) \quad (2.1)$$

where  $\sigma_x(x)$  is the  $x$  directed stress,  $\epsilon_x(x)$  is the  $x$  directed strain, and  $E$  is Young's modulus. If the rod is assumed to be in equilibrium, then  $f_1 = -f_2$  and the 1-D strain displacement law is given by

$$\epsilon_x(x) = \frac{d}{dx} u_x(x) \quad (2.2)$$



however, if the strain is assumed constant within the element, Eq (2.2) can be rewritten as

$$e_x(x) = \frac{\Delta L}{L} = \frac{u_2 - u_1}{L} \quad (2.3)$$

Substituting Eq (2.3) into Eq (2.1) yields

$$\sigma_x(x) = \frac{E}{L}(u_2 - u_1) \quad (2.4)$$

From equilibrium at the nodes and using Eq (2.4)

$$f_1 = -\sigma_x A = \frac{-EA}{L}(u_2 - u_1) \quad (2.5)$$

$$f_2 = \sigma_x A = \frac{EA}{L}(u_2 - u_1) \quad (2.6)$$

These equations can now be put in matrix form:

$$\begin{bmatrix} f_1 \\ f_2 \end{bmatrix} = \frac{EA}{L} \begin{bmatrix} 1 & -1 \\ -1 & 1 \end{bmatrix} \begin{bmatrix} u_1 \\ u_2 \end{bmatrix} \quad (2.7)$$

or written in short form

$$[f] = [K][u] \quad (2.8)$$

The matrix  $[K]$  above relating the applied loads to the nodal displacements is defined as the stiffness matrix for the 1-D rod in 1-D space. The stiffness matrix could also be derived for a 3-D problem by allowing each node to have three degrees of freedom along three orthogonal axes.

Now that the basic stiffness matrix has been derived, two or more elements can be assembled to form a structure. The assembled stiffness matrix has some attractive attributes. First, it is computationally efficient because stiffnesses exhibit a "local" nature, meaning the assembled matrix has many zero terms. Gaussian elimination techniques can then be employed to form banded or triangular matrices which can be solved algebraically for the unknown coefficients. Second, stiffnesses represent paths of force, therefore, they can be vectorially added using the properties of matrix algebra [7:17]. To illustrate, consider the two rod elements shown in Figure 2.3.

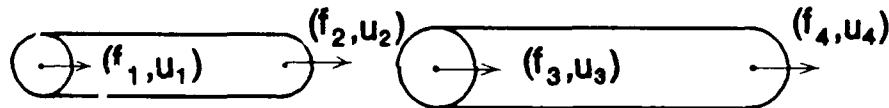


Figure 2.3. Two rod elements to be joined.

The matrix equations for the two rods are given by

$$\begin{bmatrix} f_1 \\ f_2 \end{bmatrix} = \frac{E_1 A_1}{L_1} \begin{bmatrix} 1 & -1 \\ -1 & 1 \end{bmatrix} \begin{bmatrix} u_1 \\ u_2 \end{bmatrix} \quad (2.9)$$

$$\begin{bmatrix} f_3 \\ f_4 \end{bmatrix} = \frac{E_2 A_2}{L_2} \begin{bmatrix} 1 & -1 \\ -1 & 1 \end{bmatrix} \begin{bmatrix} u_3 \\ u_4 \end{bmatrix} \quad (2.10)$$

Referring to Figure 2.3, if the two rods are to be assembled at nodes 2 and 3, then  $u_2 = u_3$ . The resultant matrix will therefore be a 3X3 matrix. To add equations (2.9) and (2.10), imbed each in a 3X3 vector space as follows:

$$\begin{bmatrix} f_1 \\ f_2 \\ 0 \end{bmatrix} = \frac{E_1 A_1}{L_1} \begin{bmatrix} 1 & -1 & 0 \\ -1 & 1 & 0 \\ 0 & 0 & 0 \end{bmatrix} \begin{bmatrix} u_1 \\ u_2 \\ u_4 \end{bmatrix} \quad (2.11)$$

$$\begin{bmatrix} 0 \\ f_3 \\ f_4 \end{bmatrix} = \frac{E_2 A_2}{L_2} \begin{bmatrix} 0 & 0 & 0 \\ 0 & 1 & -1 \\ 0 & -1 & 1 \end{bmatrix} \begin{bmatrix} u_1 \\ u_2 \\ u_4 \end{bmatrix} \quad (2.12)$$

Using the distributive properties of matrix addition, equations (2.11) and (2.12) can be added term by term to yield

$$\begin{bmatrix} p_1 \\ p_2 \\ p_3 \end{bmatrix} = \begin{bmatrix} k_{11} & k_{12} & k_{13} \\ k_{21} & k_{22} & k_{23} \\ k_{31} & k_{32} & k_{33} \end{bmatrix} \begin{bmatrix} u_1 \\ u_2 \\ u_4 \end{bmatrix} \quad (2.13)$$

or

$$[P] = [K][U] \quad (2.14)$$

where P represents the sum of nodal forces, K represents the sum of stiffnesses and U represents the nodal displacements. Although Eq (2.14) was

derived for a very simple case, the process described for determining the finite element stiffness matrix and assemblage of the individual elements to form a structure is the basis for linear static analysis using finite element theory [7].

2.2.3 Input/Output Files. As stated in section 2.2.1, NASTRAN uses finite element theory to solve linear static analysis problems. However, the structural characteristics of each finite element, such as physical and material properties, nodal connectivities, constraints and loads, must be provided by the user. This information is provided to NASTRAN via a data file called a "data deck".

The data deck consists of three basic subdecks: the Executive Control deck, the Case Control deck, and the Bulk Data deck.

The Executive Control deck is the first of the three subdecks and has the following functions: it provides control over the interface between NASTRAN and the computer operating system; it identifies the type of solution to be preformed (i.e. static,dynamic,etc.) and any alterations to that solution sequence that may be desired; and it declares the general conditions of job execution such as execution time and any system diagnostics desired.[9]

The Case Control deck is the second of the three subdecks. It is used to: define the subcase structure; specify the set of Bulk Data input to be included with each subcase; and control output requests for printing and plotting.[9]

The Bulk Data deck contains all of the details of the structural model. It is used to define grid point locations, element connectivity information, an element's physical and material properties, applied loads and constraints. This

subdeck is typically quite large, especially for complex models like aircraft structures. Because of its size, the Bulk Data deck is usually generated with a CAD pre-processor. There are a variety of pre-processors available which can generate a NASTRAN compatible input file.

The NASTRAN output data file is also a lengthy file. It contains a complete echo of the input file in addition to information on nodal displacements, strain displacements, stresses in individual elements, status of output requests and a variety of warning and error messages. Again, because of its size, a post-processor is generally used to sort through the data and only display those segments of data that are of interest.

A widely used pre-post processing CAD package, developed by Structural Dynamics Research Corporation (SDRC), is called "IDEAS". IDEAS was used to post-process the NASTRAN output files presented in this analysis. The IDEAS package contains a file translator program which is capable of converting the NASTRAN output file into a universal file which IDEAS can then interpret. As shown in the next section, IDEAS can present the results of the structural analysis in both graphical and report formats.

### 2.3 Static Structural Analysis

To perform a structural analysis of either the T-38 or C-5A airframe, NASTRAN structural models representing both aircraft had to be obtained. Fortunately, a structural analysis of both airframes using NASTRAN had been

previously performed by the organizations responsible for their development, therefore, NASTRAN models were available for both aircraft.

Since the finite element structural model of an aircraft can be very complex, the structure is generally segmented into functional components for modeling purposes. This decreases the computation time required by NASTRAN and is much more efficient than trying to model a complete structure at once. An initial assumption of this study was that only the wing structural models were required because the wings are the most flexible components of an aircraft and therefore experience the greatest deformations during flight. The fuselage and tail section were represented as rigid bodies for this study.

2.3.1 T-38 Airframe. An MSC/NASTRAN model for the T-38 was provided by SA-ALC/LADD, Kelly AFB TX. MSC/NASTRAN is a commercially available NASTRAN software package from the MacNeil Schwendler Corporation (MSC). The model included the right wing and a short section of the fuselage where the wing attached. An IDEAS graphical representation of the model is shown in Figure 2.4.

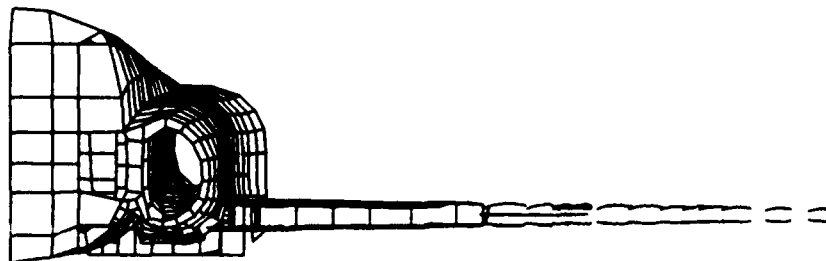


Figure 2.4. T-38 Structural Model

Along with a description of the structure, the MSC/NASTRAN file also included two load subcases representing realistic wing loads for subsonic and supersonic flight conditions. After completing the structural analysis for both subcases, it was apparent that the supersonic loads caused the greatest bending and twisting deformations in the wings. Therefore, those deformations were used in the radar cross section (RCS) analysis. The maneuver causing these deformations was a 7G pull-up at sea-level at Mach 1.2. The deformed versus non-deformed airframe for the supersonic wing loads is shown in Figure 2.5. The maximum displacement of the wing (occurring at the wingtip) was 10.35 inches which is under ten percent of the half-wing span of the T-38 (151.5 inches). The displacement data, as well as nodal locations in the non-deformed configuration were obtained from data listings written in report format by IDEAS. The nodes were located graphically by turning on a node label switch in IDEAS and then magnifying and translating the plot until the node(s) of interest, and their associated labels were visible.



Figure 2.5. T-38 Structural Deformations

A problem encountered with the T-38 model (because of its age) was that some of the finite element data cards included in the Bulk Data deck of the

MSC/NASTRAN file were being phased out by MSC and were no longer supported by IDEAS. This caused some of the element connectivity data to be lost when the MSC/NASTRAN output file was translated to IDEAS, which is why only a portion of the elements are shown in Figures 2.4 and 2.5. However, all of the non-deformed nodal locations were translated correctly and most of the nodal displacement data was captured. If a node's displacement was required for the RCS model but was unavailable in the IDEAS nodal displacement report, the node's displacement was linearly extrapolated from other nodes in its vicinity. As will be shown later, this linear extrapolation method was reasonable considering the RCS modeling limitations.

2.3.2 C-5A Airframe. The NASTRAN model for the C-5A's wing was unavailable because of proprietary elements in the model. The C-5A's developer, Lockheed-Georgia Company, Marietta Ga, has developed their own unique finite elements for use in structural analysis. Lockheed generously agreed, however, to support this academic study by providing IDEAS universal files, proprietary elements removed, containing approximately 50 load cases representing a variety of realistic flight conditions. The non-deformed structural model of the C-5A wing, as provided in the IDEAS files, is shown in Figure 2.6. Of the 50 load cases, two were chosen for use in the RCS analysis. The first was a Positive Symmetric Maneuver (PSM) representing a vertical bending displacement in the wingtips. It is a symmetric maneuver caused by a 2.5G pull-up at sea-level with the aircraft traveling at Mach .428. During the maneuver, the fuselage experiences a downward directed acceleration which



deforms both wings equally. The deformation induced by the PSM is shown in Figure 2.7. The second load case chosen was a Negative Symmetric Maneuver



Figure 2.6. C-5A Structural Wing Model



Figure 2.7. C-5A in a positive symmetric maneuver.

(NSM) representing a twisting deformation of the wing with only a slight vertical displacement. The symmetric twisting is caused by a 0G descent from an altitude of 24,500 feet at a velocity of Mach .8. The effects of the NSM are shown graphically in Figure 2.8. The maximum displacement caused by the PSM on the airframe structure was 114.23 inches in the vertical direction. For the NSM, the maximum displacement was only 20.64 inches vertically, but it occurred at the trailing point of the wingtip because of the twisting effect. It should be noted here, that the structural model of the C-5A wing does not



Figure 2.8. C-5A in a negative symmetric maneuver.

include the leading or trailing loft surfaces of the wing. To illustrate this point, refer to figure 2.9 which shows a typical wing station. The bold rectangular box in the center of the wing is the only part of the structure required for a structural analysis. Again, not modeling the aerodynamic surfaces of the wing decreases the computation time required by NASTRAN. However, since the loft surfaces were not included, displacements of nodes on the leading and trailing edges of the wings had to be extrapolated from the nodal displacement data provided by the structural analysis of the structural model. The non-deformed nodal

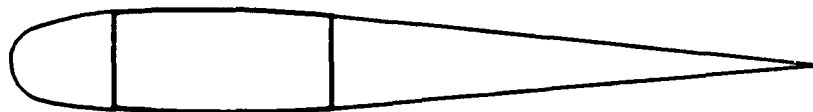


Figure 2.9. A Typical Wing Station

locations for the entire surface of the wing, including the loft data, were provided by Lockheed in hardcopy reports.

#### 2.4 Summary

This chapter has presented the methodology used to perform an static structural analysis of two airframes: a T-38 and a C-5A. It included a discussion of NASTRAN, the structural analysis tool used for this study, and the finite element theory NASTRAN employs for linear static analysis. There are also brief descriptions of the NASTRAN input/output file structures along with some pre-post processing options that are available. Finally, the results of the analysis are presented and discussed.

### III. Radar Cross Section Analysis

#### 3.1 Introduction

This chapter presents the radar cross section (RCS) analysis theory. A review of the RCS analysis software, called "RCSBSC2", is provided along with a brief discussion of the uniform geometric theory of diffraction. Also, the post-processing methods used to reduce the RCS data are presented and discussed.

#### 3.2 RCS Analysis Software

The RCS of a target is a characterization of its electromagnetic scattering properties for a given observation angle. The three-dimensional RCS is mathematically defined by the following relationship:

$$\sigma = \lim_{R \rightarrow \infty} 4\pi R^2 \frac{|E^s|^2}{|E^i|^2} \quad (3.1)$$

where  $E^s$  is the scattered electromagnetic field,  $E^i$  is the incident field and  $R$  is the distance from target to observation point. The limit as  $R$  approaches infinity in Eq (3.1) indicates that the RCS is defined under plane wave illumination. The unit of  $\sigma$  is area (typically square meters). A common designation for the RCS of a target is in dB referenced to a square meter (dBsm) which is found by

$$\sigma(\text{dBsm}) = 10 * \log_{10}\left(\frac{\sigma(m^2)}{m^2}\right) \quad (3.2)$$

If the radar's transmitter and receiver are collocated, the RCS is referred to as monostatic, however, if they are at different locations, it is referred to as bistatic. For the purposes of this study, the monostatic RCS was calculated for the airframes modeled. The electromagnetic scattering from those airframes was found by using the "Radar Cross Section - Basic Scattering Code, version 2," or in short form "RCSBSC2" [10]. The code is capable of modeling complicated structures (such as aircraft) by arbitrarily oriented, perfectly conducting, flat plates, elliptic cylinders, elliptic cone frustum sections and finite composite ellipsoids. It can be used to solve for both monostatic and bistatic scattering for all incident and scattered field polarizations [10:1]. As stated in chapter 1, section 5, the code was developed by the Ohio State University's Electroscience Laboratory, and it solves electromagnetic scattering problems by applying the uniform geometric theory of diffraction.

3.2.1 Uniform Geometric Theory of Diffraction. The uniform geometric theory of diffraction (UTD) is a high frequency, uniform asymptotic technique used to solve for the scattered electromagnetic field from an object or structure arbitrarily located in space. It is an extension of the geometric theory of diffraction (GTD) developed by Keller. "The geometric theory of diffraction is an extension of geometric optics which accounts for diffraction. It introduces diffracted rays in addition to the usual rays of geometrical optics" [11:116]. Referring to Figure 3.1, these usual rays of geometrical optics (GO) include those rays directly illuminating the receiver and those that are specularly reflected from the half-plane to the receiver.

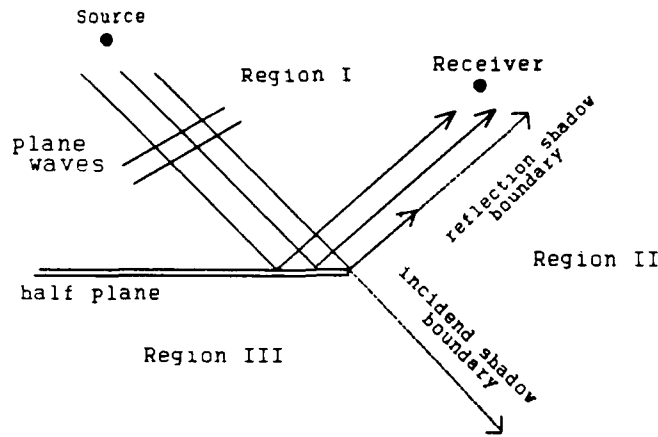


Figure 3.1. Conducting Half Plane

GO theory assumes that the field in region III is zero and that the field in regions I and II are due entirely to the incident and reflected fields. Both assumptions are false. Keller attempted to correct the GO solution by introducing diffracted rays, which when added to the GO rays provide the correct total solution. "Diffracted rays are produced by incident rays which hit edges, corners, or vertices of boundary surfaces, or which graze such surfaces" [11:116]. As an example, consider the 2-dimensional plane wedge shown in Figure 3.2. Keller's theory can be stated mathematically as

$$u^t = u^i + u^r + u^d \quad (3.3)$$

where  $u^t$  is the total field,  $u^i$  is the incident field,  $u^r$  is the reflected field and  $u^d$  is the diffracted field. The plane wave incident field is given by

$$u^i = C \frac{e^{-jk\rho_i}}{\sqrt{\rho_i}} \quad (3.4)$$

where  $k$  is the propagation constant,  $\rho_i$  is the distance from source to receiver,

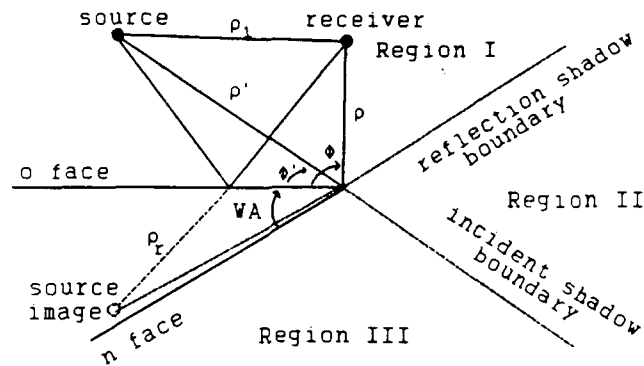


Figure 3.2. Conducting Plane Wedge [13]

and  $C$  is a complex constant. The reflected field (from a planar surface) is given by

$$u' = \pm C \frac{e^{-jk\rho_r}}{\sqrt{\rho_r}} \quad (3.5)$$

where  $\rho_r$  is the distance from the source image to the receiver. The  $\pm$  sign is used to signify either an electric line source (-) or magnetic line source (+).

Keller's diffracted field can be expressed as [11:119]

$$u^d = u'(Q_0) D \frac{e^{-jk\rho}}{\sqrt{\rho}} \quad (3.6)$$

where  $u'(Q_0)$  is the incident field at the point of diffraction,  $\rho$  is the distance from  $Q_0$  to receiver, and  $D$  is the diffraction coefficient. The coefficient is given by

$$D = \frac{e^{-j\pi/4} \sin(\pi/n)}{n\sqrt{2\pi k} \sin\beta} \left[ \frac{[(\cos(\pi/n) - \cos(\frac{\phi - \phi'}{n}))]^{-1}}{+ [(\cos(\pi/n) - \cos(\frac{\phi + \phi' + \pi}{n}))]^{-1}} \right] \quad (3.7)$$

where  $n=2\text{-WA}/\pi$ ,  $\beta$  is the angle between the plane of incidence and the edge ( $\pi/2$  in this example), and the angles  $\text{WA}$ ,  $\phi$  and  $\phi'$  are defined in Figure 3.2.

Unfortunately, the diffraction coefficient given in Eq (3.7) is valid everywhere except at the shadow boundaries, where the diffractions have the greatest effects. It was this discontinuity that lead Kouyoumjian and Pathak to develop the uniform theory of diffraction. The diffraction coefficient of UTD "remains valid in the transition regions adjacent to shadow and reflection boundaries, where the diffraction coefficients of Keller's original theory fail" [12:1448]. The UTD diffraction coefficient, for the perfectly conducting wedge, is given by [12:1453]

$$D_{s,h}(\phi, \phi'; \beta) = \frac{-e^{-j\pi/4}}{2n\sqrt{2\pi k} \sin\beta} \left[ \begin{aligned} & \left\{ \cot \left[ \frac{\pi + (\phi - \phi')}{2n} \right] F[kL^I a^+(\phi - \phi')] + \right. \\ & \left. \cot \left[ \frac{\pi - (\phi - \phi')}{2n} \right] F[kL^I a^-(\phi - \phi')] \right\} \\ & + \left\{ \cot \left[ \frac{\pi + (\phi + \phi')}{2n} \right] F[kL^m a^+(\phi + \phi')] + \right. \\ & \left. \cot \left[ \frac{\pi - (\phi + \phi')}{2n} \right] F[kL^{ro} a^-(\phi + \phi')] \right\} \end{aligned} \right] \quad (3.8)$$

where  $D_{s,h}$  are the soft (s) and hard (h) polarizations and  $F(x)$  is a transition function defined by



$$F(x) = 2/\sqrt{x} \, e^{ix} \int_{\sqrt{x}}^{\infty} e^{-t^2} dt \quad (3.9)$$

in which the positive branch of the square root is used, and

$$a^{\pm} = 2 \cos^2 \left[ \frac{2n\pi N^{\pm} - \alpha}{2} \right] \quad (3.10)$$

where  $N^{\pm}$  are the integers which most closely satisfy

$$2n\pi N^{\pm} - \alpha = \pm \pi \quad (3.11)$$

and

$$\alpha = \phi \pm \phi' \quad (3.12)$$

The  $L$  parameters in the diffraction coefficient are called the distance parameters, and are given by

$$L^I = \frac{\rho' \rho}{\rho' + \rho} \quad (3.13)$$

$$L^m = \frac{\rho_c^n \rho}{\rho_c^n + \rho} \quad (3.14)$$

and

$$L^o = \frac{\rho_c^o \rho}{\rho_c^o + \rho} \quad (3.15)$$

where  $\rho_c^n$  and  $\rho_c^o$  are the caustic distances for those rays reflected from the

edge of the  $n$  and  $o$  faces, respectively (for a planar wedge,  $\rho_c^n = \rho_c^o = \rho'$ ) [13].

A caustic is a point at which two or more rays converge or appear to converge.

An example of an apparent caustic is the source image created by the reflected rays in Figure 3.2.

The transition function  $F(x)$ , as given by equations (3.9) through (3.15), has a magnitude of one for regions away from the incident or reflection shadow boundaries. However, in regions at or near the boundaries, it allows the GO discontinuity to be compensated separately by one of the four terms in the diffraction coefficient [12:1454]. Therefore, it tends to smooth out the discontinuity at the shadow boundaries and provides a uniform total solution.

### 3.3 Data Processing

Once the scattered field has been determined and the RCS computed, there are a variety of statistical processing methods that can be applied to assist in reducing the data into a useable form. "Reduced data is not only easier for the analyst to work with but is also easier to comprehend and present" [14]. Two methods that were used in this study involved obtaining a sliding window median and sliding window average of the raw RCS data. A sliding window is a fixed range (window) of data, typically defined in aspect angles, which is allowed to slide across the full extent of data available. The median is that RCS value for which half of the data values in the window lie above and half below. The average however, is the sum of the magnitudes of the data in the window divided by the number of data points [14].

To illustrate the effect of these methods, consider the raw RCS data shown plotted in Figure 3.3. This RCS data was computed using RCSBSC2 and represents the raw RCS of a T-38 airframe. The angular resolution of the data is .5 degrees and the nose of the aircraft is at 180 degrees. A sliding window median was applied to the raw data (in units of square meters) with a

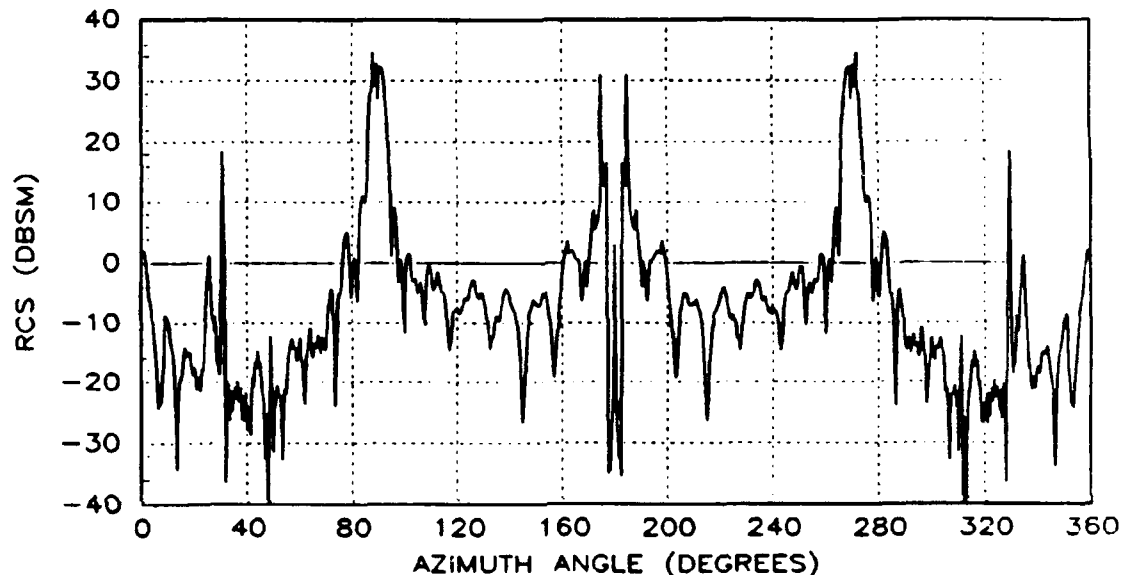


Figure 3.3. Computed Raw RCS Data for a T-38 Airframe

width of 1.5 degrees (3 data points). The result, displayed in dBsm, is shown in Figure 3.4. The narrow range was used because the only purpose of medianizing was to eliminate erroneous, single data point spikes caused by software simulation anomalies. As the author of the code points out, "the shadowing algorithms can sometimes fail when plates join. This is more likely to happen at very pointed vertices, that is, with narrow angles" [10:90]. The

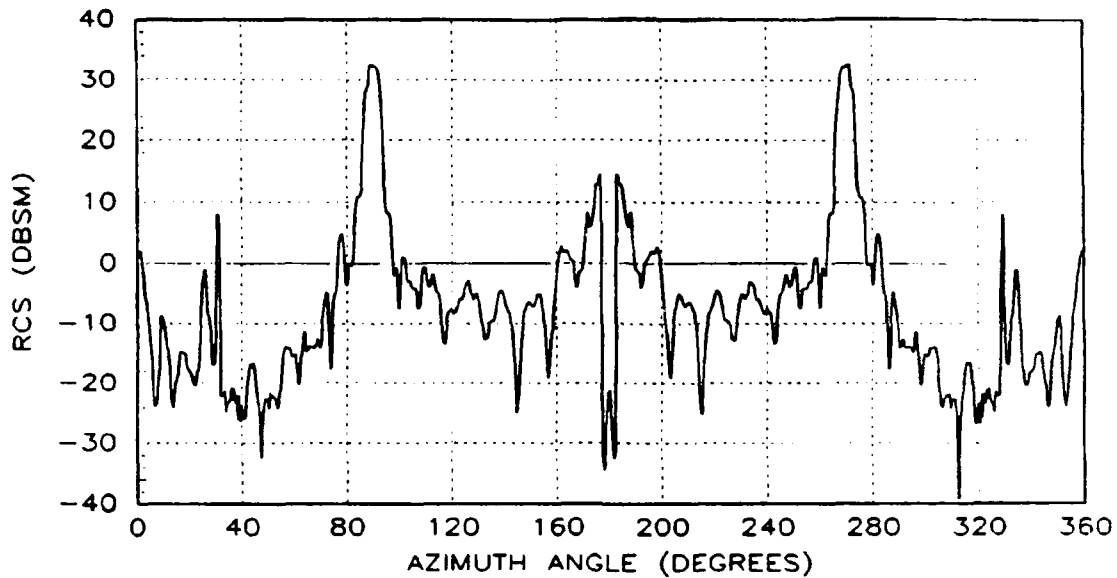


Figure 3.4. Medianized RCS Data for a T-38

small median window eliminates the spikes but preserves the integrity of the original data.

Once the medianized data was obtained, a sliding window average was applied to the data (in units of square meters) with a window of 3 degrees. The medianized, averaged RCS data for the T-38 is shown in Figure 3.5. The reason for averaging the data was strictly for presentation. Since this study is concerned with analyzing the changes in an airframe's RCS due to aeroelastic deformations, it was necessary to compare the non-deformed RCS pattern to that of the deformed. In presenting comparisons of the raw data, it was difficult to see the full effects of the deformations. Presenting comparisons of averaged data however, provided a clear indication of the changes in RCS caused by deforming the airframe. To illustrate, the plot shown in Figure 3.6 is a comparison of non-deformed versus deformed raw RCS data for the T-38.

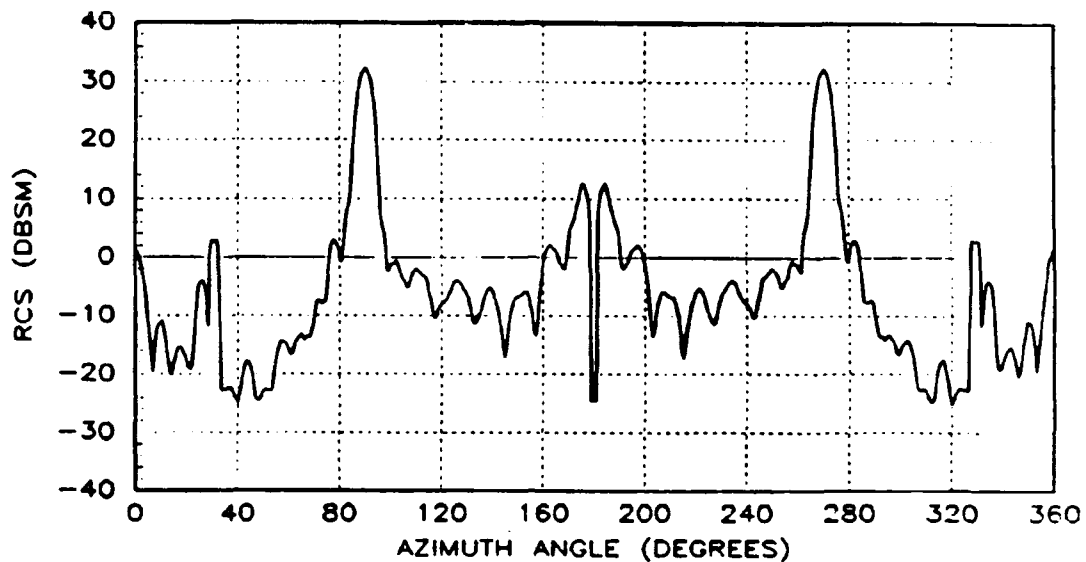


Figure 3.5. Medianized and Averaged RCS of a T-38 Airframe

Figure 3.7 is a comparison plot of the averaged data. Although the large scale changes in RCS are apparent in both plots, the small scale changes (the percentage change could still be relatively large) are lost in the raw data but are clearly evident in the average data comparison.

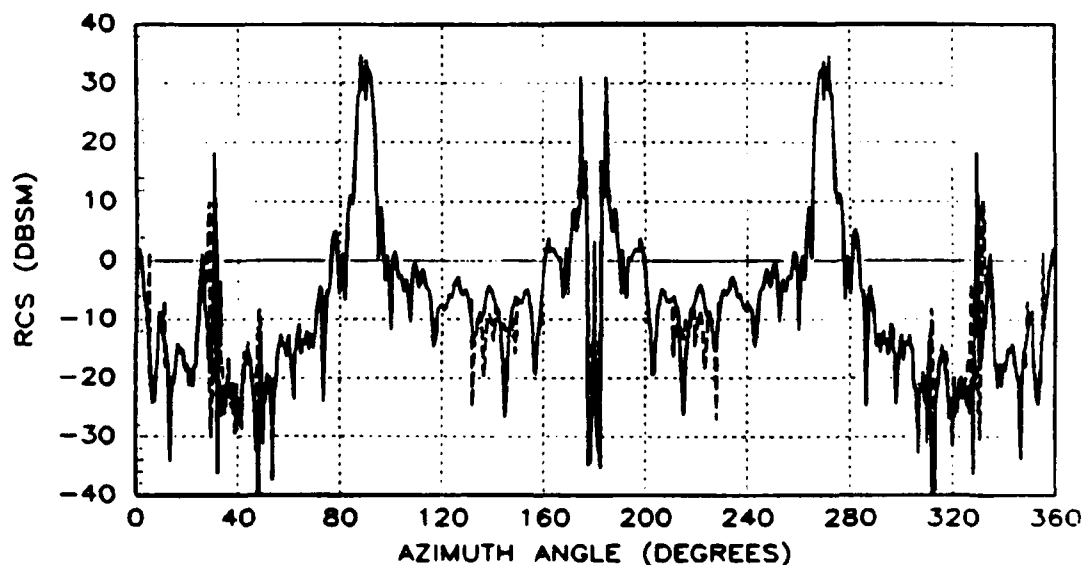


Figure 3.6. Comparison of Non-deformed versus Deformed Raw RCS Data for a T-38 Airframe

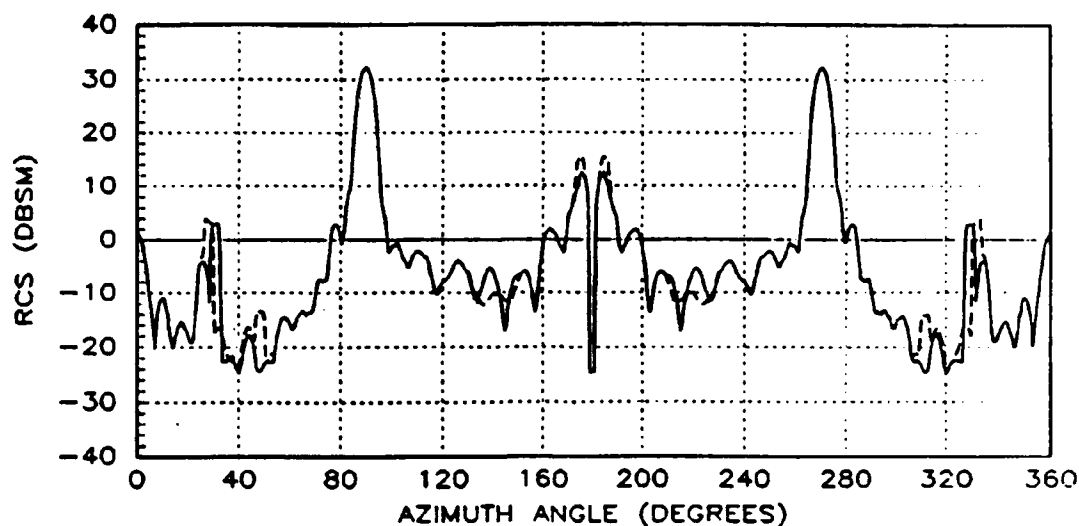


Figure 3.7. Comparison of the Averaged Data for the Non-deformed Versus Deformed T-38 Airframe

Because the fractional change in RCS can provide an effective yardstick in determining the effects of deformations, especially for low observable aircraft where the values of RCS data have been reduced, it was also selected as a means of presenting data. The fractional change is determined by simply dividing the deformed airframes medianized RCS data (in  $m^2$ ) by the non-deformed airframes medianized data (in  $m^2$ ). This delta change in RCS is then presented in dBsm by the following relationship.

$$\delta = 10 * \log_{10} \frac{\text{deformed rcs}}{\text{non-deformed rcs}} \quad (3.16)$$

The results for the T-38, horizontal and vertical field polarizations, are shown in Figure 3.8. Note that the significance of the small scale changes seen in the

averaged data of Figure 3.7 are clearly demonstrated when coupled with the fractional change form of presentation.

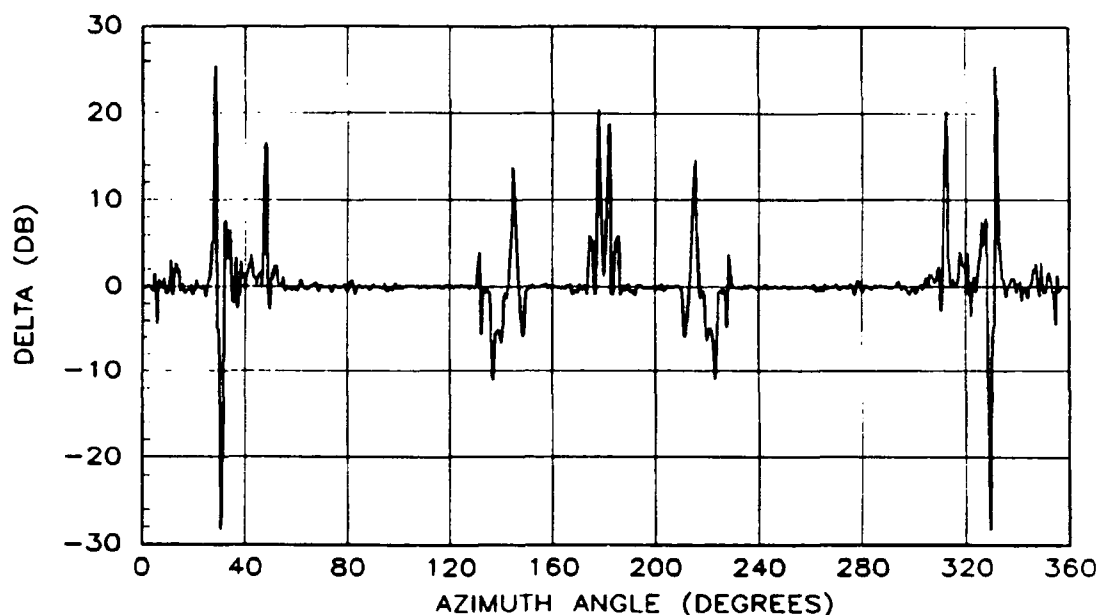


Figure 3.8. Fractional (Delta) Change Between the Non-deformed and Deformed T-38 Airframe

### 3.2 Summary

This chapter has presented the approach used to perform the radar cross section analysis. A description of the RCS analysis software was provided including a discussion of the uniform geometric theory of diffraction which is the basis for the analysis. Post-processing techniques were also presented. A sliding window median and sliding window average were two methods used to reduce the raw RCS data. In addition, several forms of data presentation were reviewed, such as average data comparisons and fractional change plots.

## IV. Results

### 4.1 Introduction

This chapter presents the results of the radar cross section (RCS) analysis for the non-deformed versus deformed airframes. First the methodology used to incorporate the results of the structural analysis into the RCS model are discussed. Then the variations in RCS caused by the aeroelastic deformation of the airframes are presented and analyzed.

### 4.2 Methodology

As stated in the last chapter, the RCS analysis software, RCSBSC2, is capable of modeling aircraft by a combination of flat plates, elliptic cylinders, elliptic cone frustum sections and finite composite ellipsoids. Using these geometries, RCS models for both the T-38 and C-5A aircraft were constructed. The models are shown graphically in Figures 4.1 and 4.2 respectively.

4.2.1 T-38 Modeling. Referring to the T-38 model, Figure 4.1, the fuselage was constructed of three truncated elliptic cone frustums. The engine housings on either side of the fuselage were also modeled with truncated elliptic cone frustums. The engine cavities were modeled as flat plates as were the elevators and vertical stabilizer. Since the wings had to be capable of deforming, they were modeled as a collection of triangular flat plates with each corner of every triangle corresponding to a node, or the median distance between two nodes, of the structural model. The median distance between



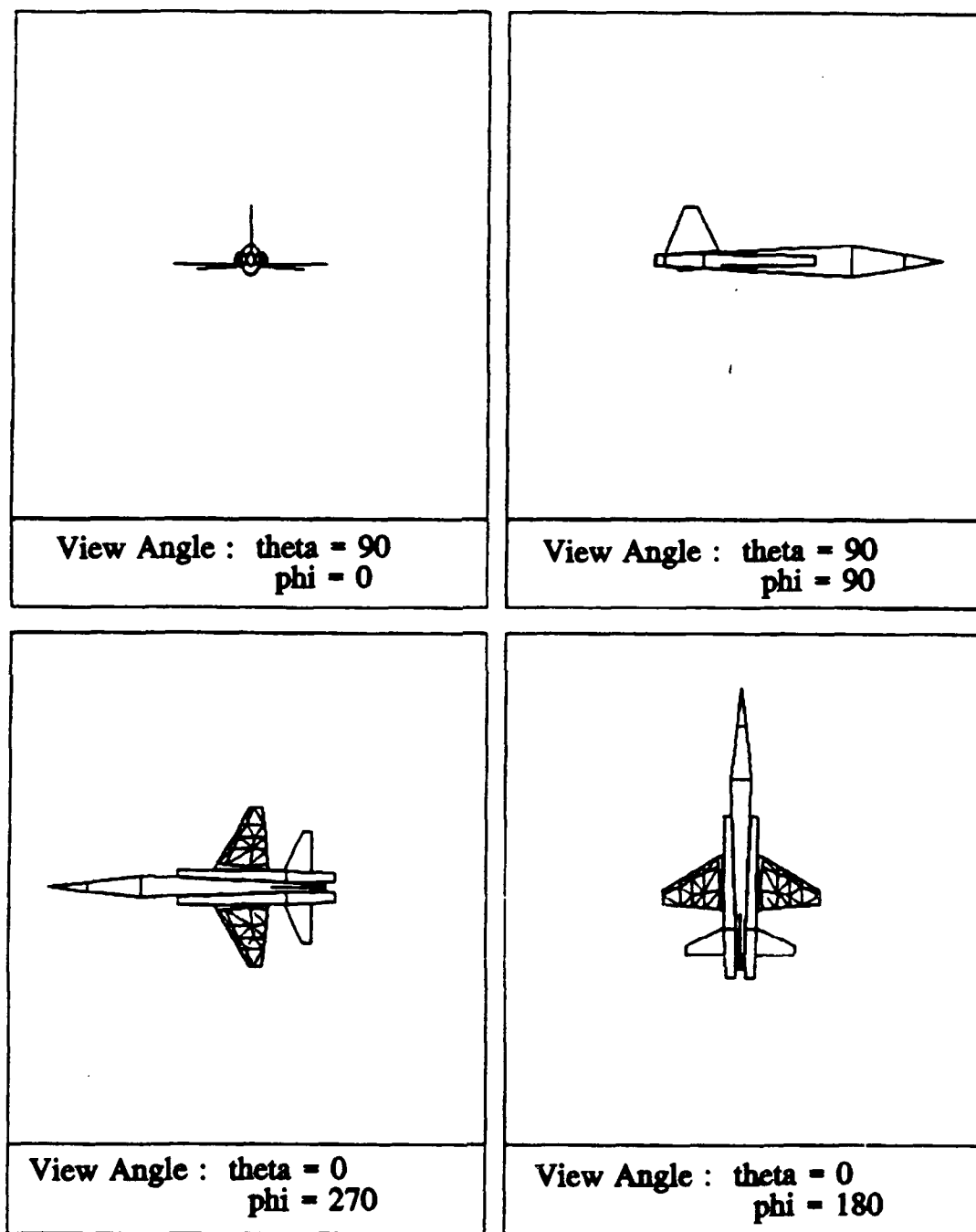


Figure 4.1. RCS Model for the T-38 Airframe

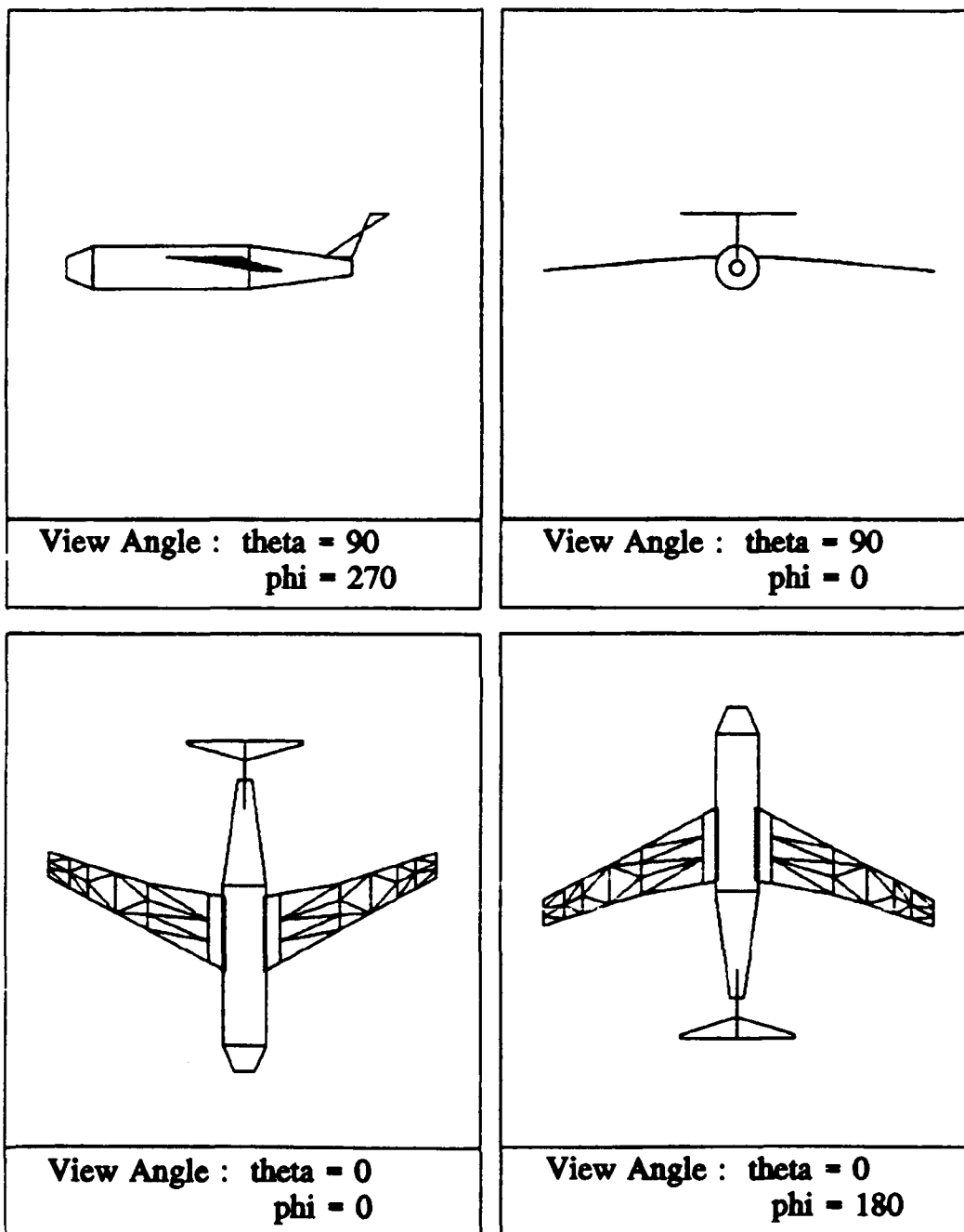


Figure 4.2. RCS Model of the C-5A Airframe

nodes lying on the upper and lower surfaces of the wing were used except along the leading and trailing edges. The triangular facets allowed the wing to bend or twist by simply redefining the position of the nodes to correspond to the deformed nodal locations provided by the structural analysis. The maximum deformation experienced by the T-38 was 10.35 inches at the rear outer wingtip. Although most of the nodal displacement occurred in the vertical direction, most nodes also experienced some displacement toward the fuselage. All displacements in the aft direction were negligible and not included in the RCS model. The deformed airframe, as modeled by HCSBSC2, is shown graphically in Figure 4.3 where it is compared to the non-deformed airframe.

4.2.2 C-5A Modeling. Referring to Figure 4.2, the fuselage of the C-5A model was composed of a circular cylinder with truncated circular cone frustums on each end. The vertical stabilizer and elevators of the tail section were modeled as flat plates and the wings, as with the T-38 model, were modeled with triangular flat plates to allow deformation.

The maximum nodal deformation of the C-5A wing engaged in a positive symmetric maneuver (PSM) was 114.23 inches. For the negative symmetric maneuver (NSM), the maximum displacement was 20.64 inches. Like the T-38, most of the nodes comprising the C-5A wing structural model did experience a displacement toward the fuselage and all aft-directed displacements were negligible. The deformed C-5A airframes are compared graphically to the non-deformed airframe in Figure 4.4.

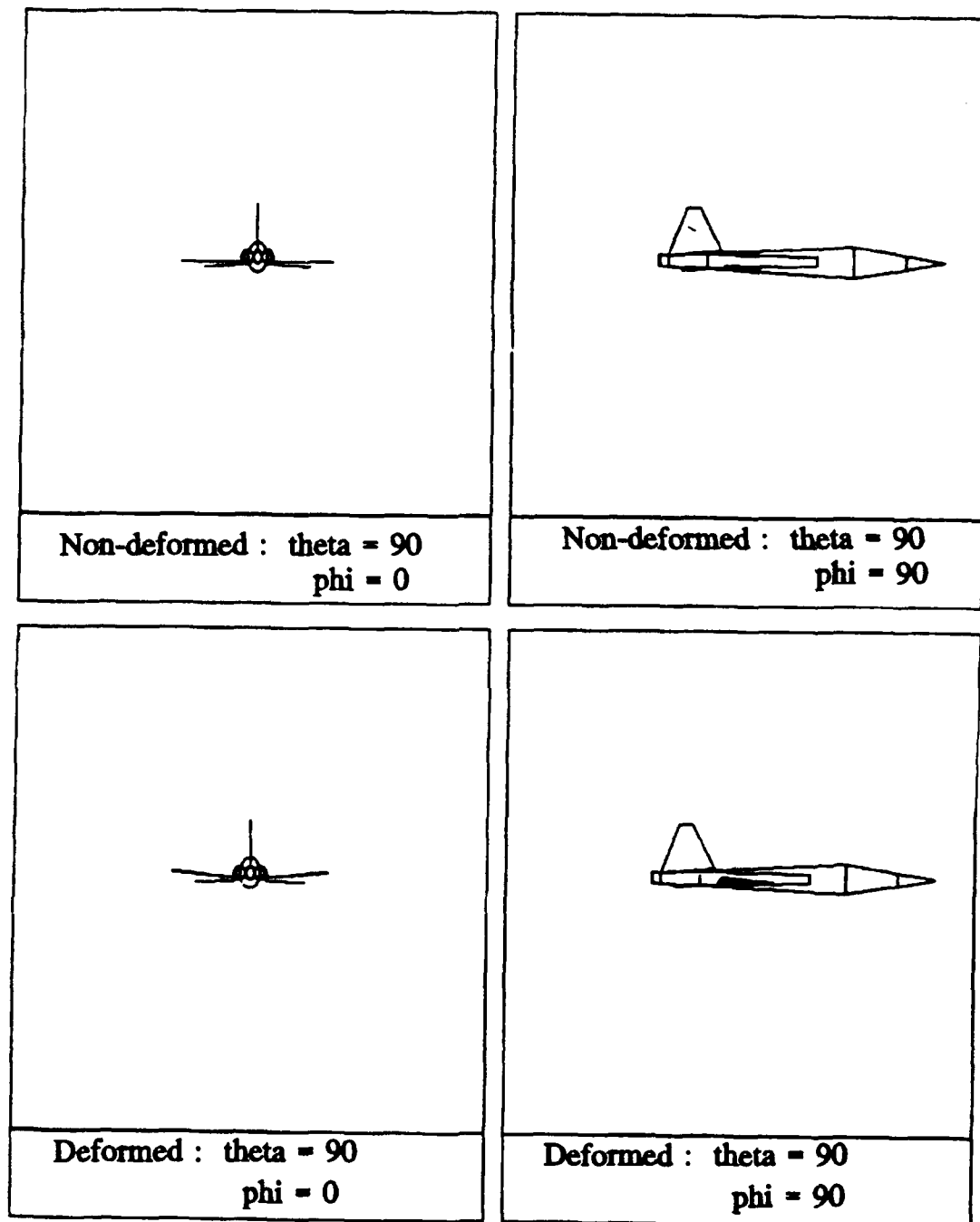


Figure 4.3. Deformed Versus Non-deformed RCS Model of the T-38

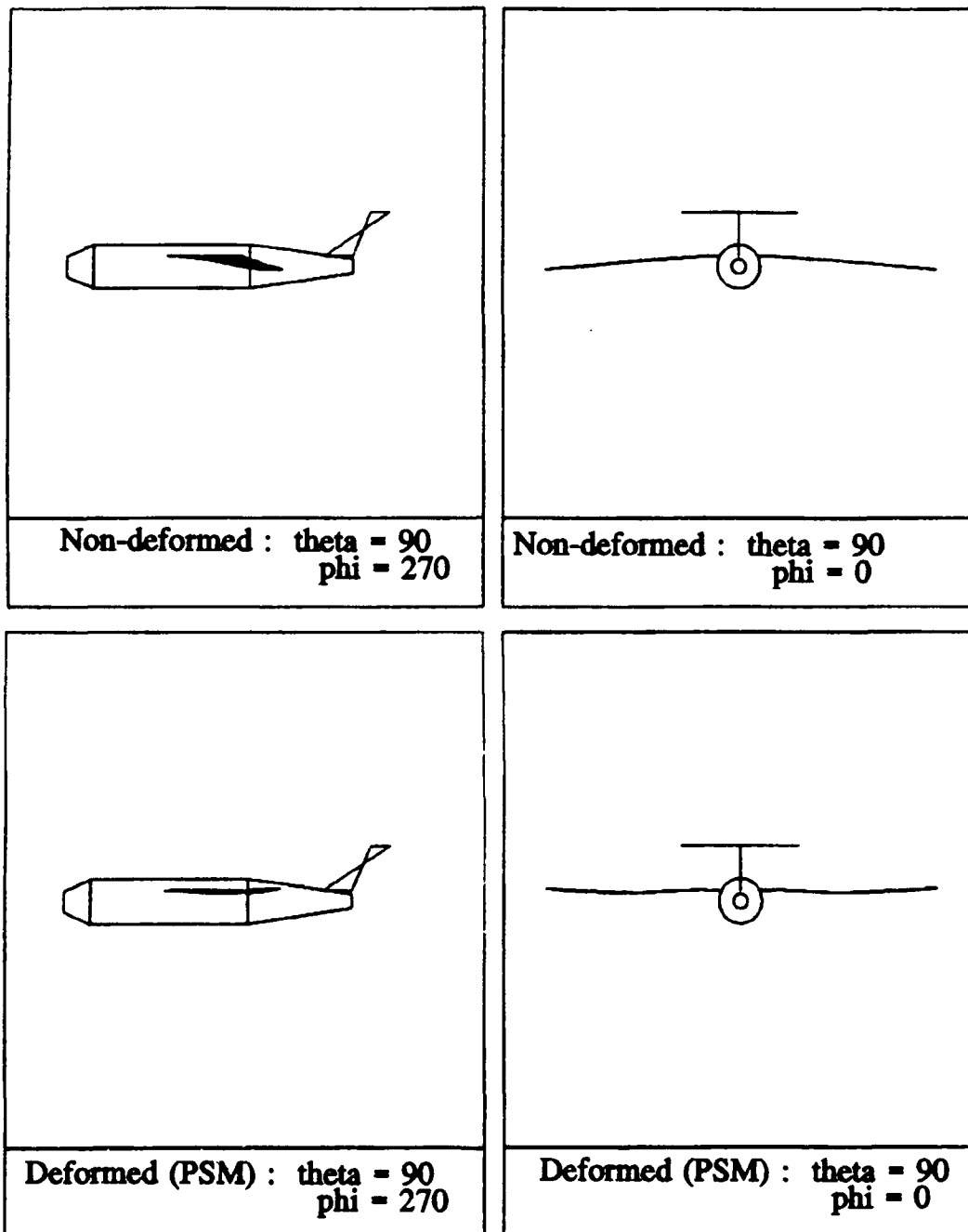


Figure 4.4 (a). Deformed (PSM) Versus Non-deformed RCS Model of the C-5A

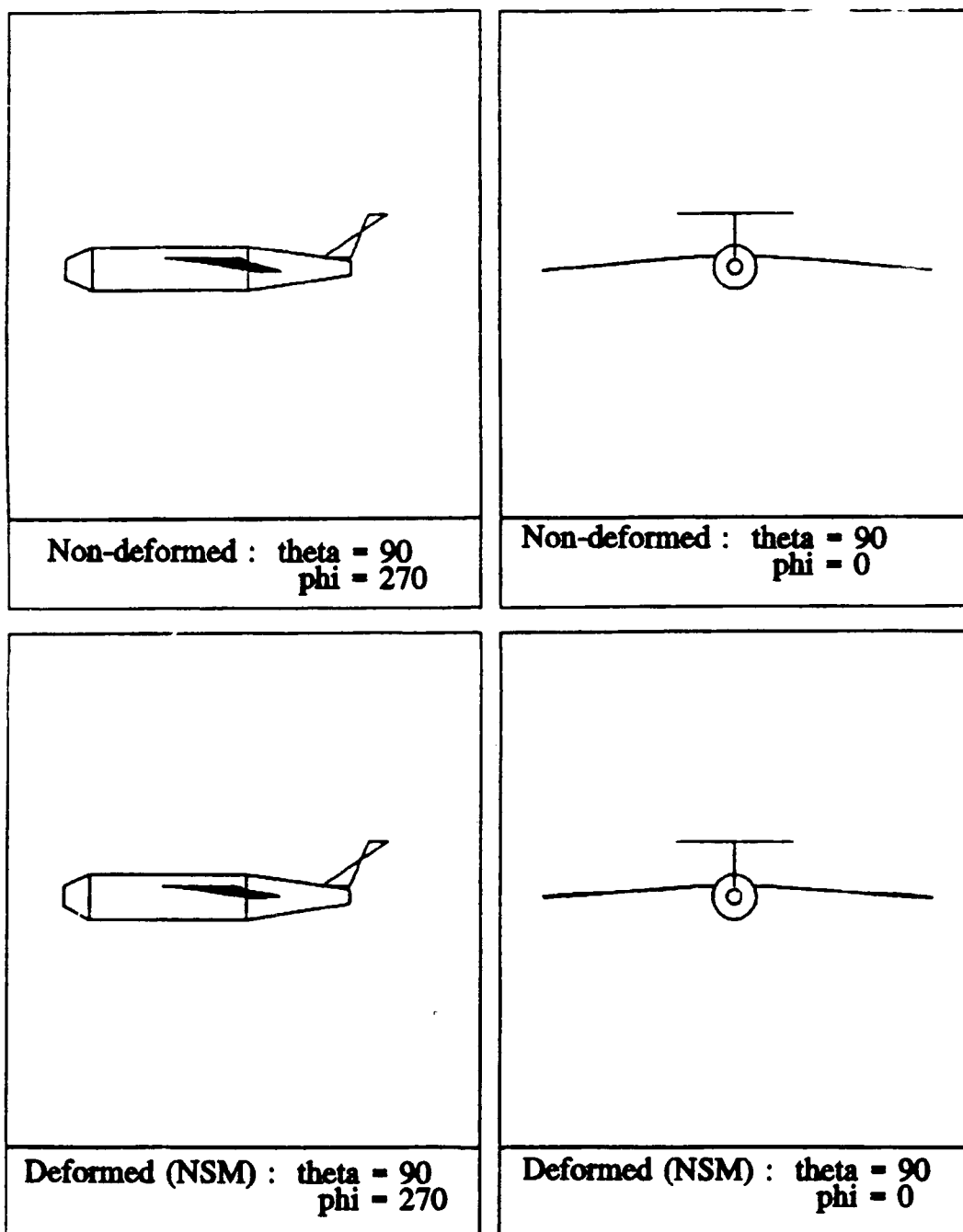


Figure 4.4 (b). Deformed (NSM) Versus Non-deformed RCS Model of the C-5A

**4.2.3 General Analysis Methodology.** The overall strategy for performing this analysis was straightforward: compute the RCS of the non-deformed airframes over a variety of aspect angles, then make the same RCS computation for the deformed airframe and characterize the differences between them. Each RCS computation was made for 360 degrees of azimuth angle at elevations ranging from -30 to 30 degrees in 10 degree increments. In all data plots, the nose of the aircraft is located at 180 degrees and positive elevation angles indicate that the observer is below the aircraft. Characterizing the differences in RCS signatures resulted in a variety of options for displaying the data. Several were examined including simply plotting the delta between the non-deformed and deformed RCS patterns. As stated in chapter 3 however, the two forms of presentation chosen were average data comparisons and fractional change plots.

### **4.3 T-38 Analysis Results**

The T-38 was analyzed for an incident field frequency of 1 GHz, which has a wavelength of twelve inches. Therefore the maximum wing deformation of 10.35 inches is less than one wavelength of displacement. Both horizontal (H-pol) and vertical (V-pol) polarizations were analyzed with the incident and scattered fields having the same polarizations for a given RCS computation. The raw RCS data for the T-38 analysis is shown in Appendix C and the average data comparison plots are provided in Appendix A.

To analyze the RCS of the T-38 airframe, it is convenient to define the

angular orientation of some of the dominant scatterers as shown in Figure 4.5. Note that the leading edge of the wings are swept back 31 degrees from nose-on. Referring to the raw RCS data in Figure C.8(a), this swept angle translate

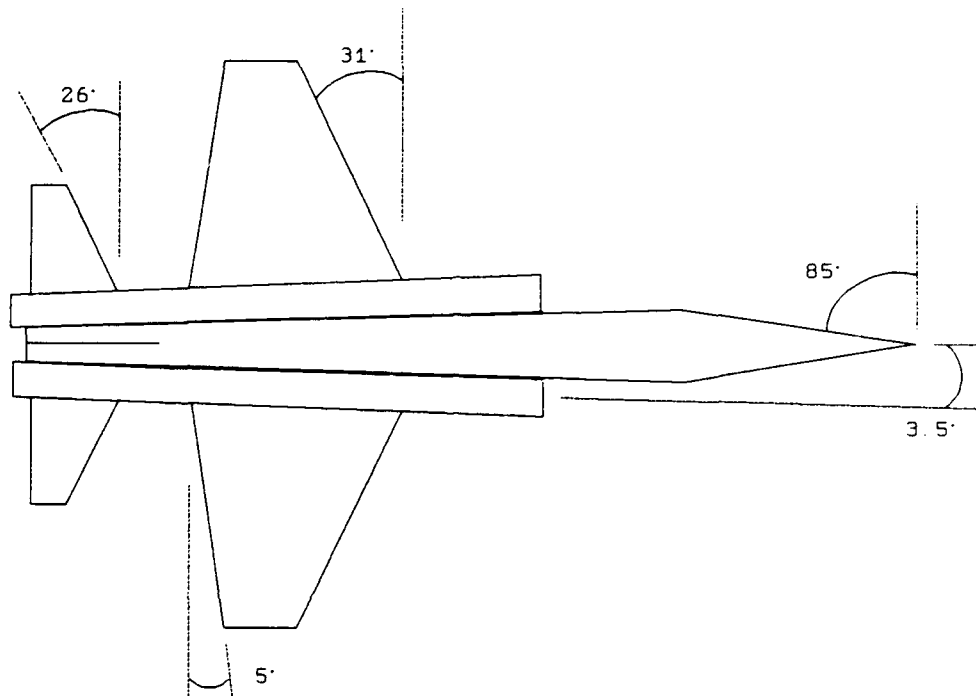
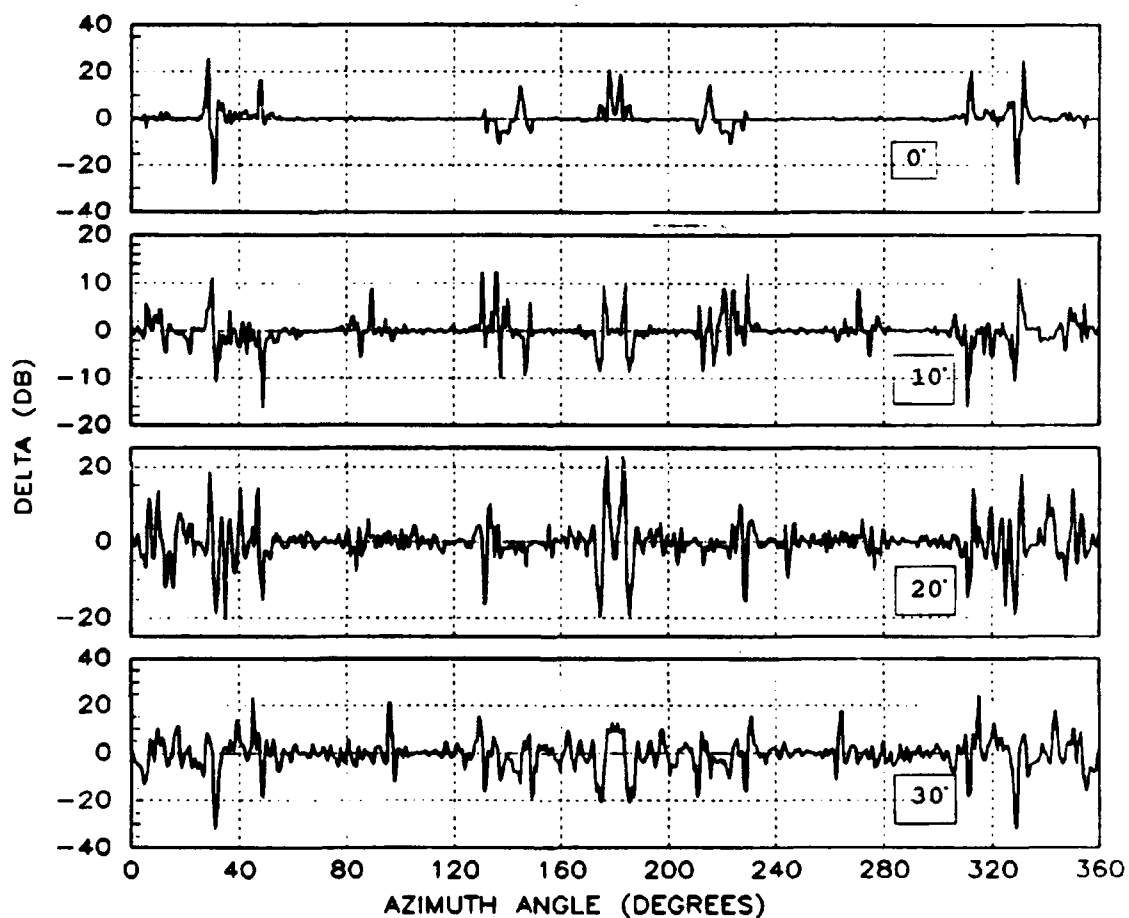


Figure 4.5. Angular Dimensions for the T-38 RCS Model to an H-pol return of 24 dBsm at zero degrees elevation but is barely distinguishable in the V-pol plot of Figure C.1(a). The difference arises from the fact that at zero elevation, the non-deformed flat plate wing has no vertical components from which the vertically polarized incident plane wave can diffract. However, the electric field component of the H-pol field is parallel to the edge and therefore diffracts along its entire length, causing a much higher level return signal.

Based on the preceding discussion, it is reasonable to assume that if the wing were deformed in a manner such that it now had a small vertical



component, the V-pol RCS data would reflect that deformation in the form of higher RCS values at that aspect angle. Referring to the top plot of Figure 4.6, which shows the percent change between the non-deformed and deformed airframe at zero degrees elevation, it is evident that adding a vertical component to the wing geometry has had a significant effect. Comparing this plot to its averaged data counterpart, Figure A.1(a), it can be seen that the relative scale of the change is small but the fractional change caused by the deformation is large. The effect is compounded by the fact that the wing is



**Figure 4.6. Percent Change Between the Non-deformed and Deformed T-38 Airframe for Elevations of 0, 10, 20 and 30 Degrees Respectively. Vertical Polarization**

not only bent upward, it is also twisted so that a short section of the rear edge of the wingtip is higher than the leading edge. This short section is now directly illuminated by the incident field which diffracts at the discontinuity between the edge and free space causing the small spikes at 5 degrees off nose-on. The two center spikes appear to be caused by increased constructive phase interference between the scattered field from the deformed wingtip and one or more of the other scattering points on the airframe. This analysis is reinforced as the elevation of the aircraft is increased because the upward bent rear edge of the wing becomes shadowed and the spikes at 5 degrees disappear, however, the two center spikes tend to both vary in magnitude and shift slightly in azimuth as the elevation changes, finally merging into one large center lobe at 30 degrees elevation. It should be noted that these center lobes at the upper elevations are not necessarily the result of small scale changes, as comparisons with Figures A.2(a) through A.4(a) reveals. At 30 degrees elevation the deformed airframe has a nose-on averaged RCS return 10 dBsm (an order of magnitude) higher than that of the non-deformed airframe. In addition to the variations around nose-on, there are also variations in RCS at other aspect angles which become more pronounced as the elevation increases. These variations represent both increases and reductions (negative dBsm) in RCS values caused by the aeroelastic deformation of the airframe.

If the observer is re-positioned above the aircraft (negative elevation angles), the rear edge of the wing becomes more visible to the observer as the

elevation decreases. Referring to Figure 4.7, the RCS around nose-on incidence is only marginally affected by the deformations as the elevation decreases. However, the rear edge contributions clearly become more significant although they are small scale. Comparison with the averaged RCS data in Figures A.5(a) through A.7(a) reveals that only at -10 degrees elevation are the RCS values of the rear edge lobes increased in magnitude by the deformation. At the lower elevations, the magnitudes are the same or less than those of the non-deformed airframe. However, the lobes are shifted

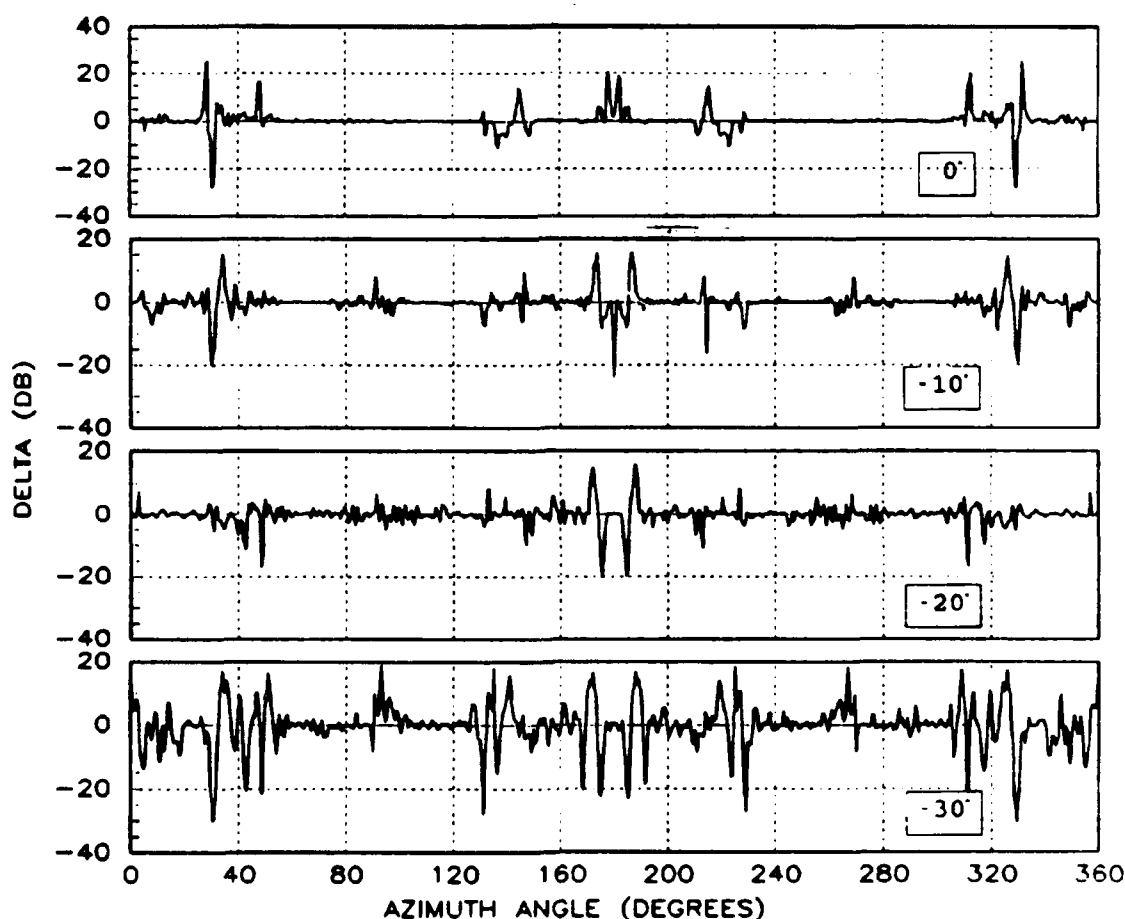


Figure 4.7. Percent Change Between the Non-deformed and Deformed T-38 Airframes for Elevations of 0, -10, -20 and -30 Degrees Respectively. Vertical Polarization

slightly in azimuth angle, due to the twisting of the wing changing its spatial orientation with respect to the observer, which causes the fractional change to be a significant value even though the relative levels of the return signal have not changed.

From the preceding discussion it is clear that deforming the airframe causes a variety of fluctuations in RCS for the vertically polarized fields because of the addition of vertical components to the geometry of the wings. The horizontally polarized fields also experience variations in RCS as the airframe is deformed. Figure 4.8 shows H-pol plots for the percent change in positive

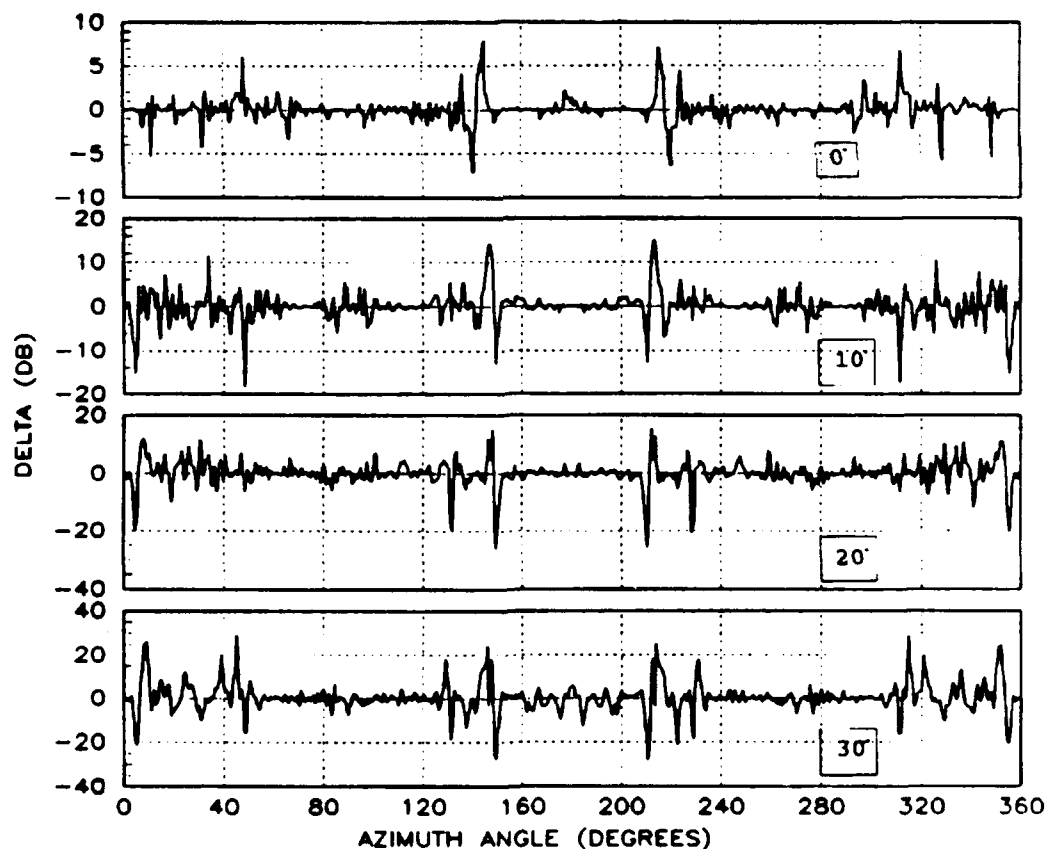
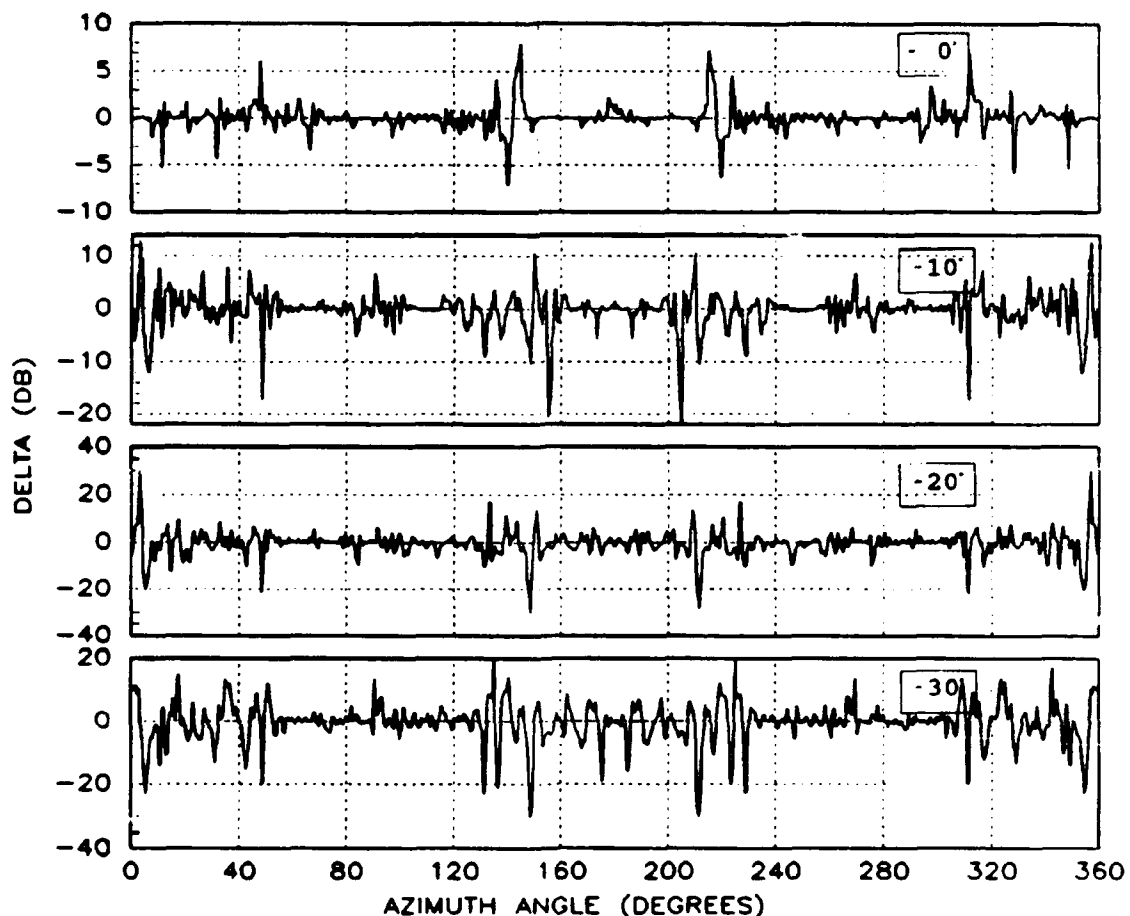


Figure 4.8. Percent Change Between the Non-deformed and Deformed T-38 Airframes for Elevations of 0, 10, 20 and 30 Degrees Respectively. Horizontal Polarization

elevation angles. At zero degrees elevation, the deformations have little effect on the H-pol return. However, their effects become more pronounced as the elevation increases. Comparing the plots of Figure 4.8 with their respective averaged data plots in Appendix A, it can be seen that most of the large fractional changes occur because of angular shifts or angular broadening of the lobing structure in the return signals. The same is basically true of the negative elevation angles, shown plotted in Figure 4.9, with a few exceptions. Examining the averaged data plots for the negative elevations, Figures A.5(b) through



**Figure 4.9. Percent Change Between the Non-deformed and Deformed T-38 Airframes for Elevations of 0, -10, -20 and -30 Degrees Respectively. Horizontal Polarization**

A.7(b), shows a greater fluctuation in magnitude at azimuth angles near nose-on ( $\pm 30$  degrees) for -20 and -30 degree elevations. These fluctuations suggest that the deformed wing appears shorter at those elevations, which reduces the magnitude of the scattered field from the leading edge of the wing as well as modifying the phase interactions from the various scatterers on the airframe.

#### 4.4 C-5A Analysis Results

To analyze the RCS of the C-5A using RCSBSC2 it was necessary to scale down all of its dimensions by a factor of ten. Therefore, the incident field frequency was also scaled by ten to 10 GHz, which is a wavelength of 1.2 inches. At that wavelength the maximum nodal displacement of the C-5A wing in a positive symmetric maneuver is 9.5 wavelengths, and for the negative symmetric maneuver it is 1.7 wavelengths. The raw RCS data for the C-5A analysis is shown in Appendix D and the averaged data comparison plots are provided in Appendix B. The angular geometry definitions needed for the C-5A analysis are shown in Figure 4.10.

4.4.1 Positive Symmetric Maneuver. As stated in chapter 3, in a PSM the fuselage experiences a downward directed force which tends to bend both wings symmetrically upward, thereby modifying their vertical components in relation to the incident field. Since the wings are canted downward in their non-deformed state, see Figure 4.4, the effect of the PSM is to flatten them out in

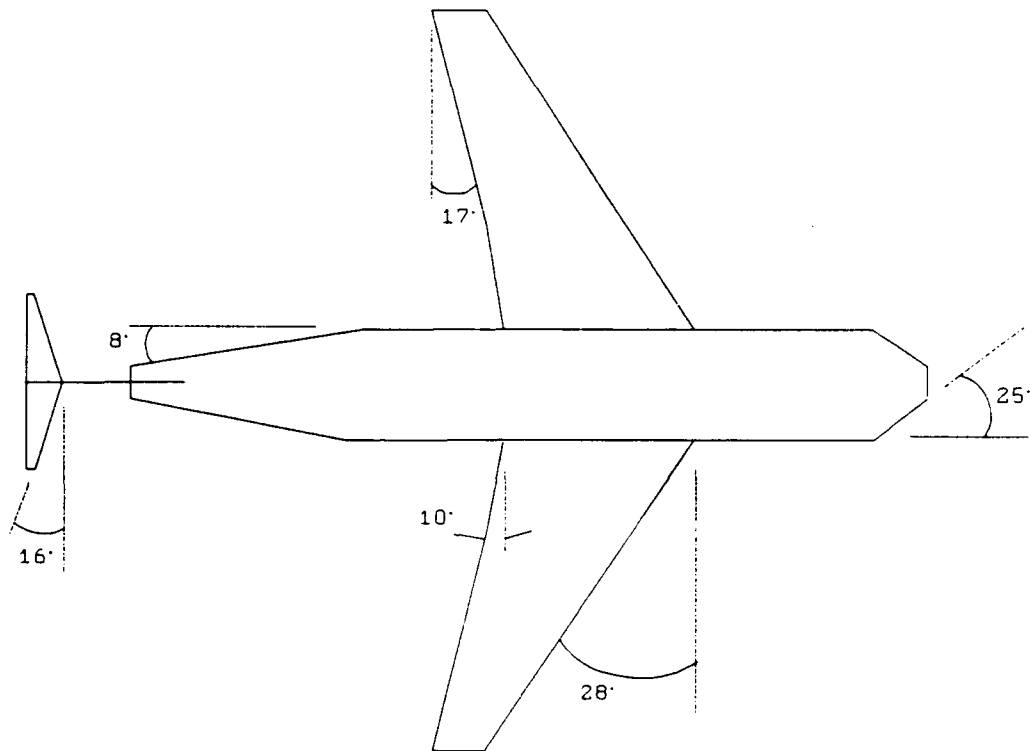


**Figure 4.10. Angular Dimensions of the C-5A RCS Model**

the horizontal plane. As shown in the zero elevation plot of Figure 4.11, this flattening of the wings has little impact on the overall RCS pattern except for some noticeable changes in the diffractions from the rear edges, occurring at 17 degrees off nose-on, and at broadside where the lobe structure of the return signal is shifted slightly. As the elevation increases, the rear edge diffractions become more dominant and the variation at broadside disappears. In addition, large fractional changes appear at approximately 28 degrees from tail-on which corresponds to the leading edge of the wing as seen from the rear of the airframe. Apparently more of the leading edge has become visible from the rear of the aircraft due to the deformation. Referring to the corresponding averaged data plots of Appendix B, these variations in RCS from both the

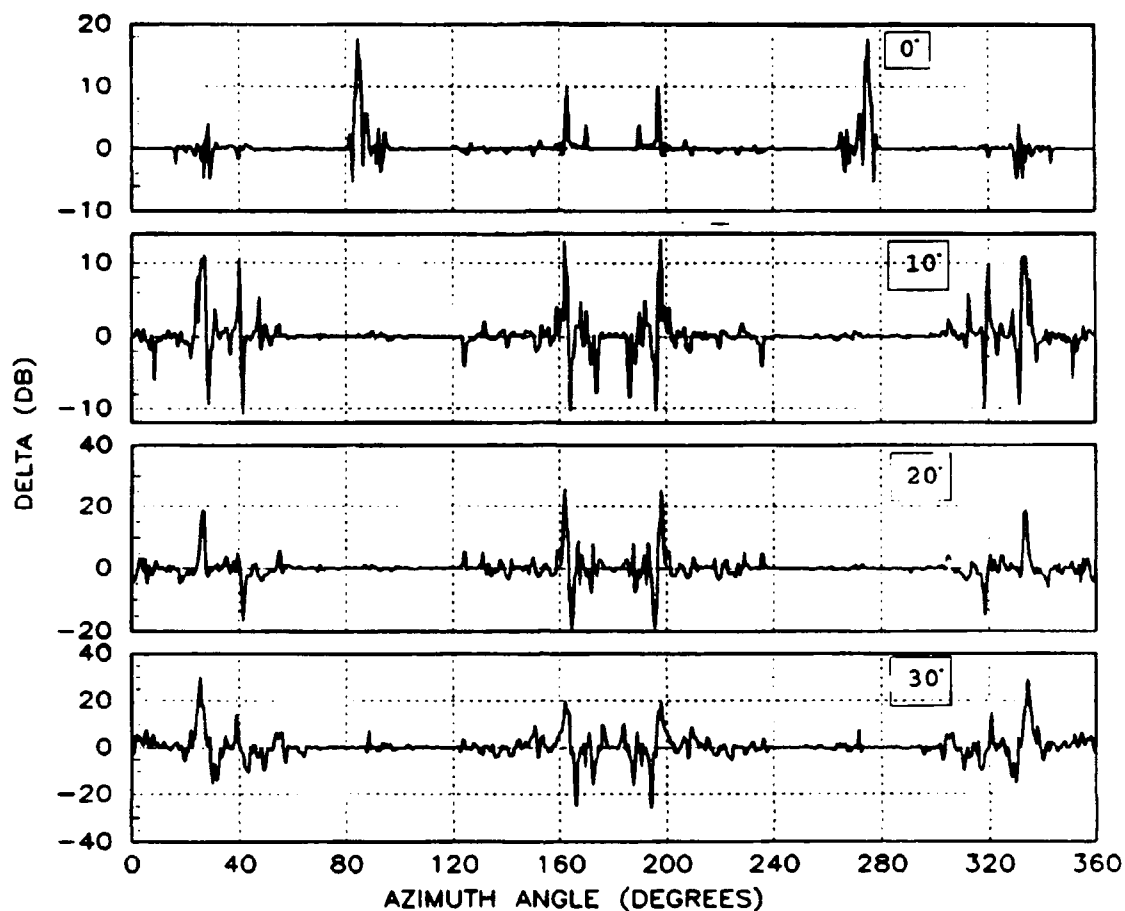


Figure 4.11. Percent Change Between the Non-deformed and Deformed C-5A Airframes for Elevations of 0, 10, 20 and 30 Degrees Respectively. PSM : Vertical Polarization

leading and rear edges of the wings are primarily due to increased magnitudes in the return signals coupled with small shifts in azimuth angle. The same basic analysis applies for the negative elevation angles. Consider the fractional change plots of Figure 4.12. These plots are very similar to the positive elevation plots of Figure 4.11, and in fact, the same variations in RCS are occurring. The only differences arise from the new angular orientations of the observer with respect to the deformed edges of the wings.



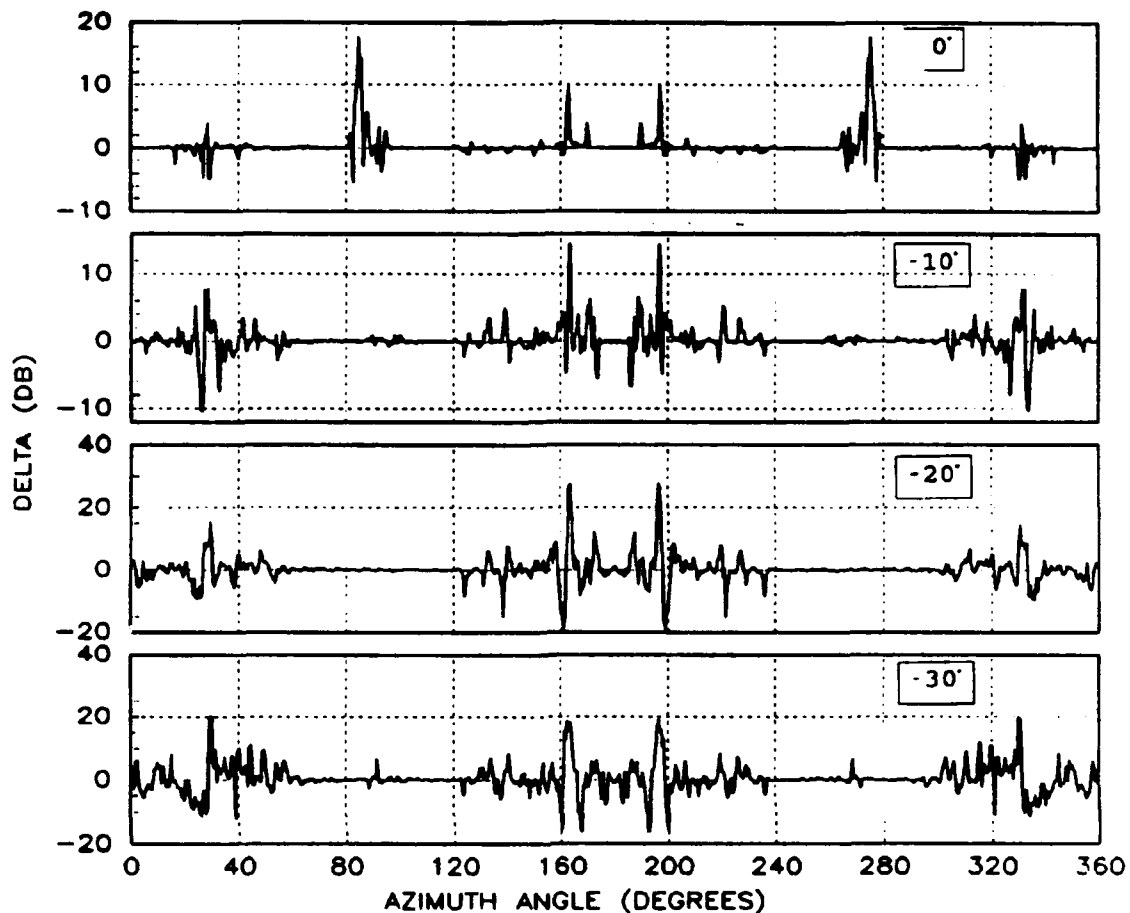


Figure 4.12. Percent Change Between the Non-deformed and Deformed C-5A Airframes for Elevations of 0, -10, -20 and -30 Degrees Respectively. PSM : Vertical Polarization

If the deformed airframe is illuminated with a horizontally polarized plane wave, the changes in RCS from the non-deformed airframe can be characterized as shown in Figures 4.13 and 4.14. It is interesting to note that for the H-pol incident field, there is relatively little variation in the RCS for a 20 degree cone of aspect angles around the nose. These variations are only slightly worse at  $\pm 30$  degrees elevation where several of the broader peaks (at 4 degrees off nose-on) approach 200 percent change for the positive elevation and 300 percent change for the negative elevation. The largest variations for

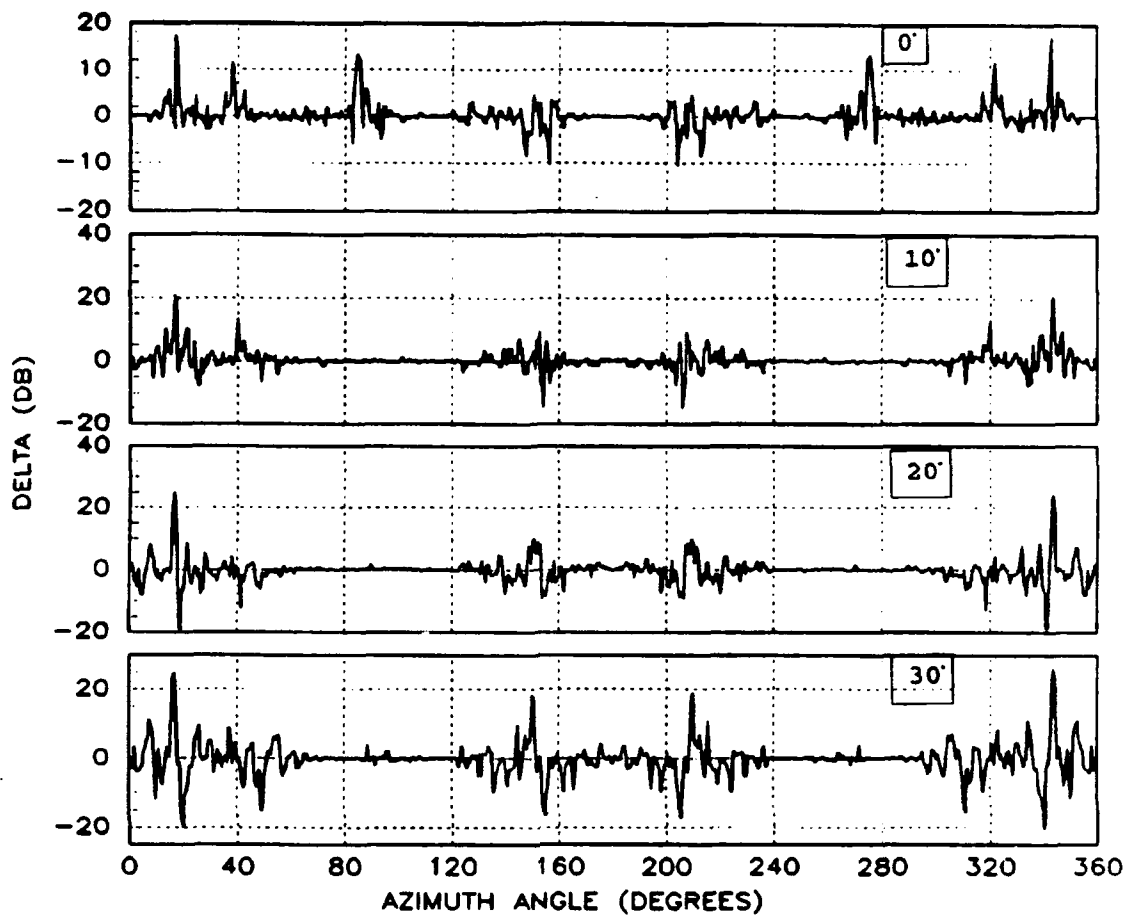


Figure 4.13. Percent Change Between the Non-deformed and Deformed C-5A Airframes for Elevations of 0, 10, 20 and 30 Degrees Respectively. PSM : Horizontal Polarization

the H-pol incidence occur at those aspect angles corresponding to the edges of the wings. For all elevations, these changes are the result of higher magnitude returns coupled with small angular shifts in the return signal. The higher magnitude returns are expected because the wings are being flattened, placing more of the edge in the plane of incidence with the illuminating field. The angular shift is simply caused by the varying spatial orientation of the deformed wing with respect to the non-deformed wing.

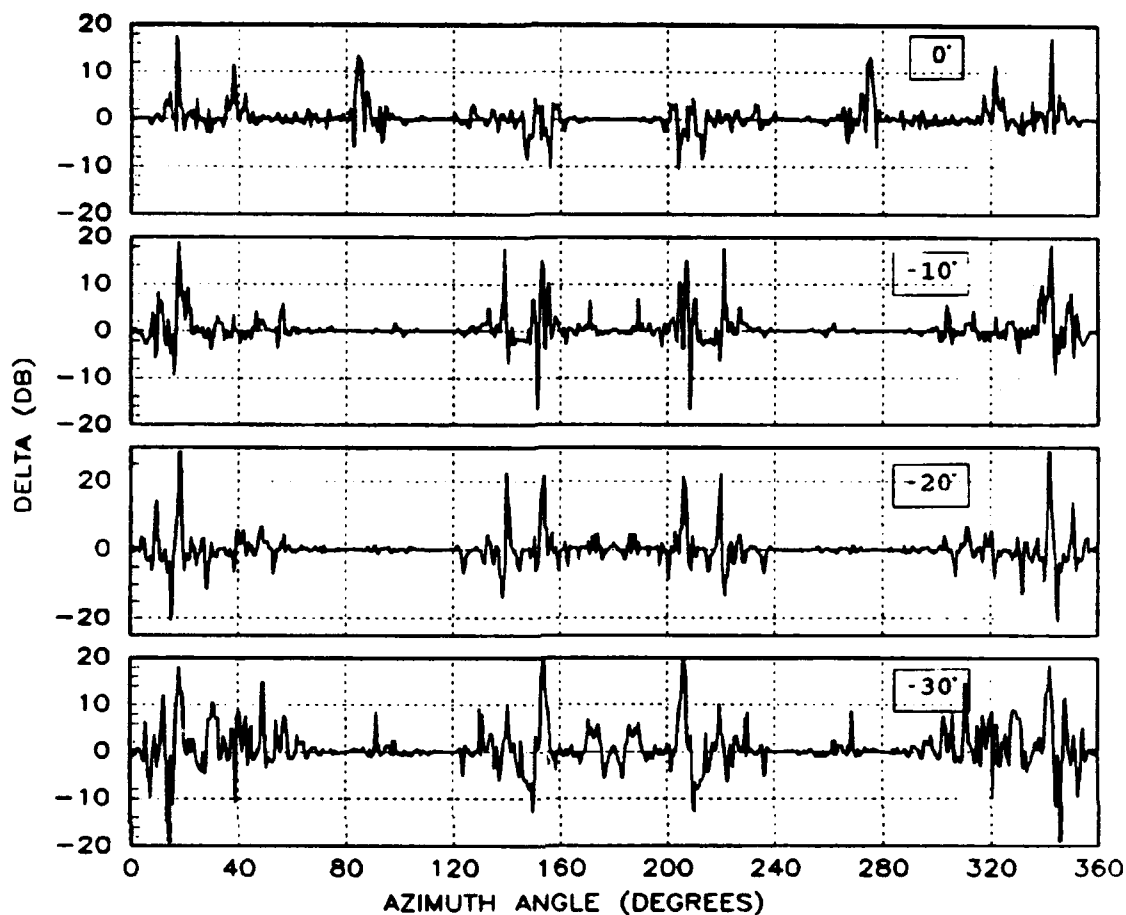


Figure 4.14. Percent Change Between the Non-deformed and Deformed C-5A Airframes for Elevations of 0, -10, -20 and -30 Degrees Respectively. PSM : Horizontal Polarization

**4.4.2 Negative Symmetric Maneuver.** As stated in chapter 3, the NSM produces predominately a twisting deformation of the wing with only a small upward bend. As seen previously, this twisting of the wingtip allows the outer rear edge of the wing to be directly illuminated by the incident field. In the case of a vertically polarized field, this results in slightly higher returns from those edges as compared to the non-deformed wing. The V-pol plots representing this situation for positive elevation angles are shown in Figure 4.15. Note that

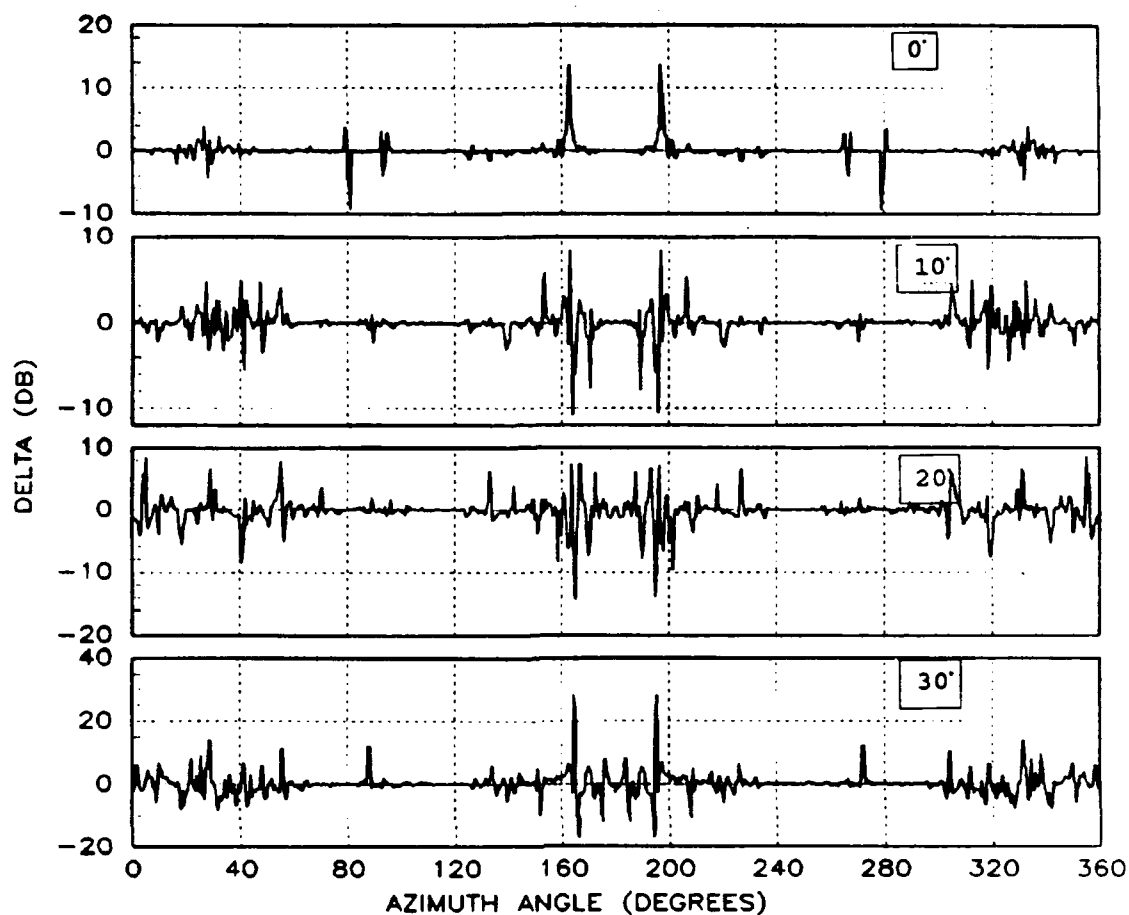


Figure 4.15. Percent Change Between the Non-deformed and Deformed C-5A Airframes for Elevations of 0, 10, 20 and 30 Degrees Respectively. NSM : Vertical Polarization

at zero elevation, the dominant change is from the rear edge of the wing at 17 degrees off nose-on. Then as the elevation increases, the portion of the edge that is bent upward becomes shadowed by the front of the wing and no longer contributes to the return signal. Referring to the average data plots in Appendix B, the smaller, narrower spikes appearing in the 10 and 20 degree elevation plots of Figure 4.15 at 17 degrees azimuth are attributable to the smaller, slightly broader lobes present in the deformed RCS patterns. These modified lobes are probably caused by the returns from the shortened rear edges of

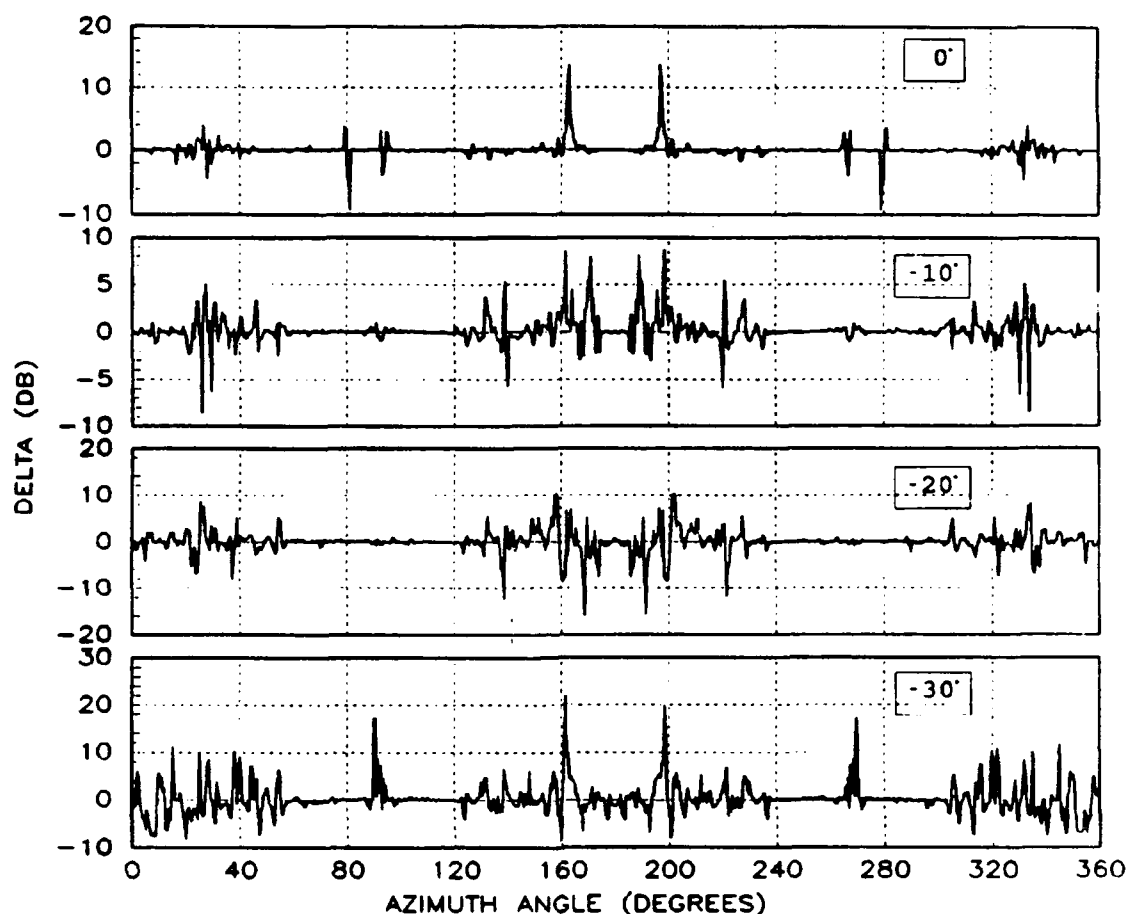


Figure 4.16. Percent Change Between the Non-deformed and Deformed C-5A Airframes for Elevations of 0, -10, -20 and -30 Degrees Respectively. NSM : Vertical Polarization

the wings which are still visible at those elevations. The opposite occurs at negative elevations angles, shown in Figure 4.16. At -10 degrees elevation the return from the deformed rear edge of the wing, which is still visible, is stronger than that of the non-deformed wing due to a larger vertical component in the deformed wings geometry at that aspect angle. Then at -20 degrees elevation, the average data plot of Figure B.13(a) reveals that the magnitude of scattered field from the rear edge decreases due to the deformations. The large fractional change seen at approximately 22 degrees off nose-on is actually a

small scale variation caused by a broadening of the rear edge lobe. This effect suggests that the edge appears slightly shorter to the observer at this aspect angle. At 30 degrees of elevation, positive or negative, the entire surface of the wing is illuminated causing varied phase interactions between the deformed wing and other scatterers on the airframe. These changes in the phase interference pattern result in large variations in the RCS patterns between the deformed and non-deformed structures.

Now consider the effects of the NSM deformations for a horizontally polarized incident field. Plots showing the percentage variations in RCS for positive elevations are given in Figure 4.17. For zero elevation, the only significant variation in RCS occurs at azimuth angles near the tail of the aircraft where the rear edge of the wing forms the leading edge to the observer. Figure B.8(b) shows that twisting the rear edge of the wing upward has increased the magnitude of that return. At 10 degrees elevation the rear edge is also noticeable along with some variations corresponding to the leading edge of the wing (28 degrees off nose-on). These leading edge variations occur at all of the positive elevations and are due to the slight upward bend of the deformed wing in the horizontal plane.

Upon examining the plots for the negative elevations, shown in Figure 4.18, and comparing them with their corresponding averaged data plots in Appendix B, it can be seen that both the leading and trailing edge variations discussed above are also present at the negative elevation angles. In fact the only notable difference between the positive and negative elevations occurs at

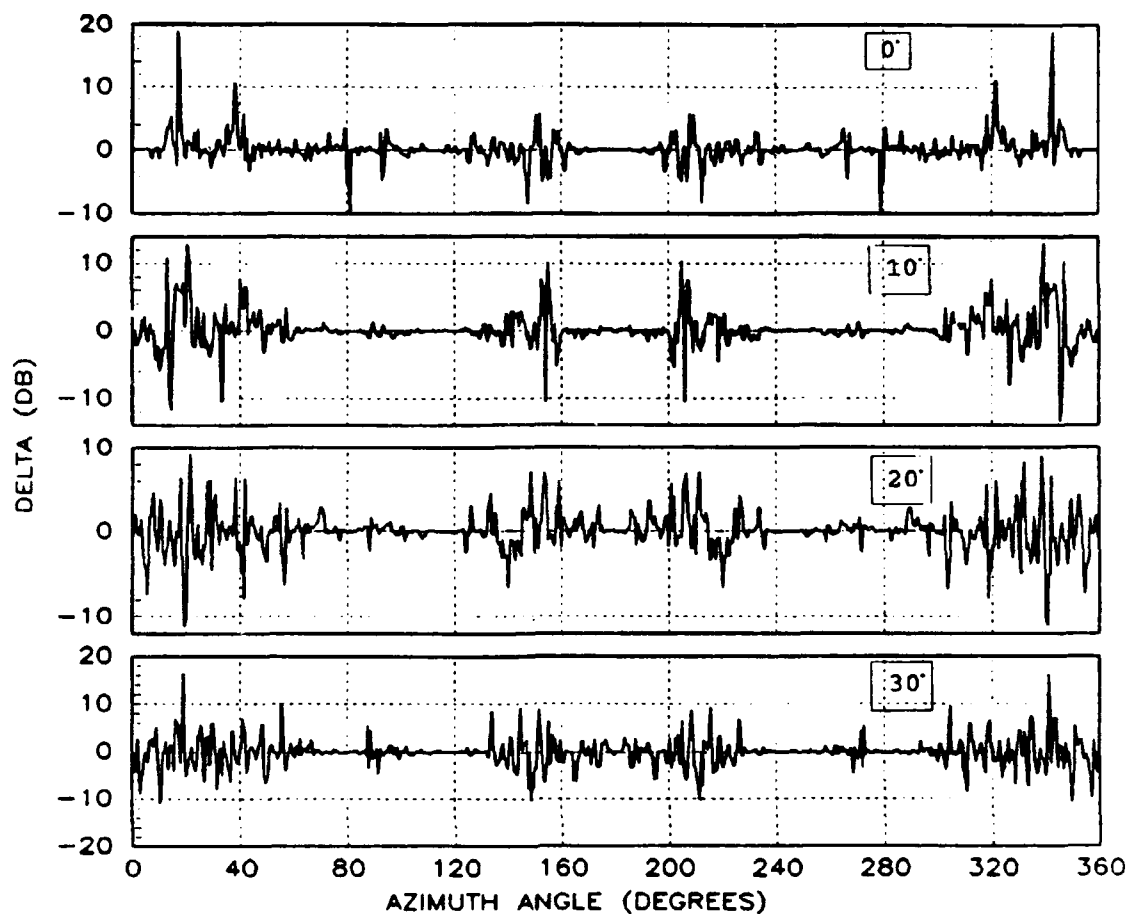


Figure 4.17. Percent Change Between the Non-Deformed and Deformed C-5A Airframes for Elevations of 0, 10, 20 and 30 Degrees Respectively. NSM : Horizontal Polarization

broadside (90 degrees) for -30 degrees elevation. However, since the same variation occurs for the vertically polarized field, see Figures B.14(a&b), it suggests that the deformed wing is causing increased constructive phase interference at that aspect angle and that the changes in RCS (which are relatively large increases in magnitude) are not polarization dependent.

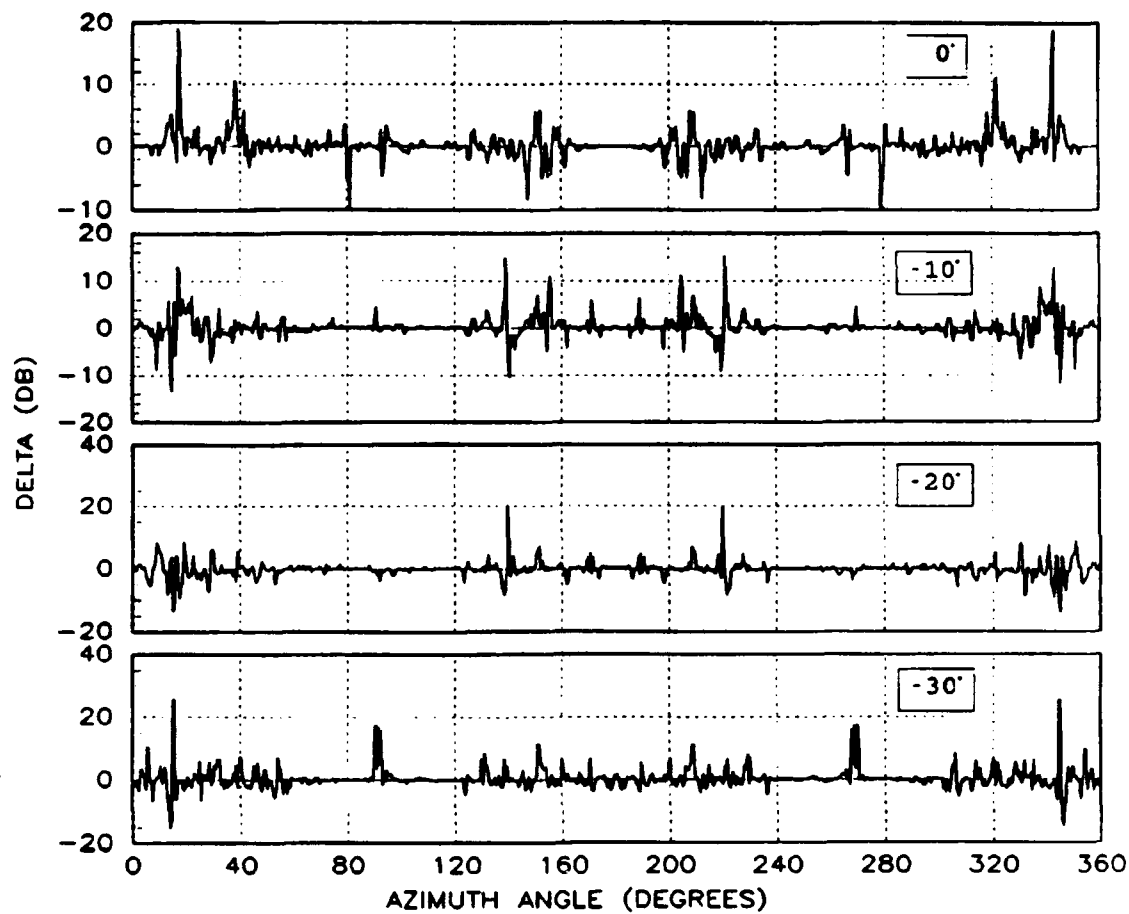


Figure 4.18. Percent Change Between the Non-deformed and Deformed C-5A Airframes for Elevations of 0, -10, -20 and -30 Degrees Respectively. NSM : Horizontal Polarization

#### 4.5 Summary

This chapter has presented both the methodology for performing the deformational analysis and the results of that analysis. First, the non-deformed and deformed RCS models of the T-38 and C-5A aircraft were described. Then the results of the RCS analysis for both airframes were presented and discussed. The RCS analysis included 360 degree conical pattern cuts at seven different elevations and both horizontal and vertical field polarizations.



## V. Conclusions and Recommendations

### 5.1 Introduction

This chapter provides a brief summary of the results of the analysis and presents the conclusions of this study. The conclusions are followed by several recommendations for continued research in this area.

### 5.2 Conclusions

Based on the analysis presented in Chapter 4 it is clear that aeroelastic deformations do have a measurable effect on the radar cross section (RCS) of aircraft. As stated in Chapter 1, RCS is geometry sensitive. If the aircraft's geometry is changed, its RCS will also change.

The effects can be lumped into basically two categories: (1) variations in the lobing structure of the RCS pattern, or (2) changes in amplitude of various lobes within the RCS pattern. Variations in the lobing structure include broadening or narrowing of individual lobes, caused by edges that appear to change length when deformed, and shifting of lobes in azimuth angle, caused by changes in the spatial orientation of the scatterer with respect to the radar.

Changes in amplitude can also be attributed to apparent variations in edge lengths since a longer edge will diffract more of the incident energy. Other significant contributors were variations in the constructive/destructive phase interference pattern and edges becoming visible that were previously shadowed when the structure was in its non-deformed state. These effects

occurred both independently and in conjunction with one another causing increases in individual lobe amplitudes as high as 14 dBsm (25 times larger) and decreases in amplitude by values as large as 20 dBsm (100 times smaller).

As might be expected, the more rigid T-38 airframe experienced less dramatic changes in the amplitude of its RCS pattern than the large, flexible C-5A did. However, the RCS pattern for the T-38 did experience both amplitude fluctuations and variations in its lobing structure, which demonstrates the sensitivity of the RCS to changes in geometry, even for relatively small changes (the structural deformation was less than one wavelength for an incident field of 1 GHz).

In the case of the C-5A, the larger structural deformation produced the most dramatic changes in RCS, again as might be expected. As described in Chapter 3, the larger deformation was produced by a Positive Symmetric Maneuver (PSM) which primarily causes a bending deformation in the wings of the C-5A. This vertical bending tended to flatten the wings in the horizontal plane causing a variety of fluctuations in the RCS pattern for both the horizontally and vertically polarized fields.

The second structural deformation imposed on the C-5A airframe was a Negative Symmetric Maneuver (NSM). The NSM produced a twisting deformation of the wings with much smaller structural displacement than the PSM. The observed effects on the RCS of the C-5A as a result of the NSM were somewhat polarization dependent due to the twisting effect of the

deformation. For example, at 0 degrees elevation the horizontally polarized return reflected negligible changes in RCS for forward aspect angles (front half of the airframe) while the RCS for a vertically polarized field showed nearly a 14 dBsm increase in amplitude from the lobe corresponding to the rear edge of the wing.

These variations in RCS should be accounted for by both the system designer and threat modeler if they are to adequately design for or assess the survivability of the aircraft. Unfortunately, characterizing the changes in RCS caused by structural deformations for a variety of aircraft is a difficult process. The structural models do not normally include all of the surfaces of the aircraft, such as loft surfaces on the wings, because those surfaces are not required for the structural analysis and it is computationally more efficient to omit them. Therefore, the translation of the structural model (both non-deformed and deformed) into an RCS model must be done manually (if one of the various RCS prediction codes is to be used). Dynamic RCS measurements of an aircraft is a possibility, but those measurements tend to be costly and access to dynamic measurement ranges is limited.

### 5.3 Recommendations for Further Research

As a continuation of this research, a recommendation would be to investigate the effects of aeroelastic deformations on the RCS of more aircraft at more frequencies. The changes in RCS should be characterized for various stages of airframe structural deformation to obtain a complete representation of

the aeroelastic effects on RCS. Since NASTRAN models are not always readily available, due to proprietary elements in the model for example, IDEAS universal files should be requested since they contain all of the structural information required. Also, use of an RCS software package that can interpret computer aided design (CAD) geometry files would make the translation from structural model to RCS model easier and the RCS CAD model would be a more accurate representation of the actual airframe.

Another recommendation for continued research in this area would be to perform a statistical analysis of the changes in RCS due to structural deformation to determine if some form of probability distribution function could be applied to characterize the changes. This type of analysis might be limited to examining a 30 or 40 degree sector of aspect angles around nose-on incidence for a class of aircraft, such as fixed wing fighters for example, where all aircraft are scaled to provide the same wavelength/dimension ratio.

#### 5.4 Summary

This chapter has presented the conclusions of this research and recommendations for further research. The bottom line was that aeroelastic deformations do have a measurable effect on the RCS of aircraft and the nature of those effects need to be accounted for by system designers and threat modelers. Recommendations for further research included expanding this study to include more aircraft and performing a statistical analysis of the changes in RCS of an aircraft due to aeroelastic deformations.

## Appendix A

This Appendix contains the medianized, averaged computed RCS data for the non-deformed versus deformed T-38 airframe. The RCS of the non-deformed airframe is shown in solid lines and the RCS of the deformed is represented by dashed lines. In the following plots, the nose of the aircraft is located at 180 degrees and the illuminating frequency is 1 GHz.

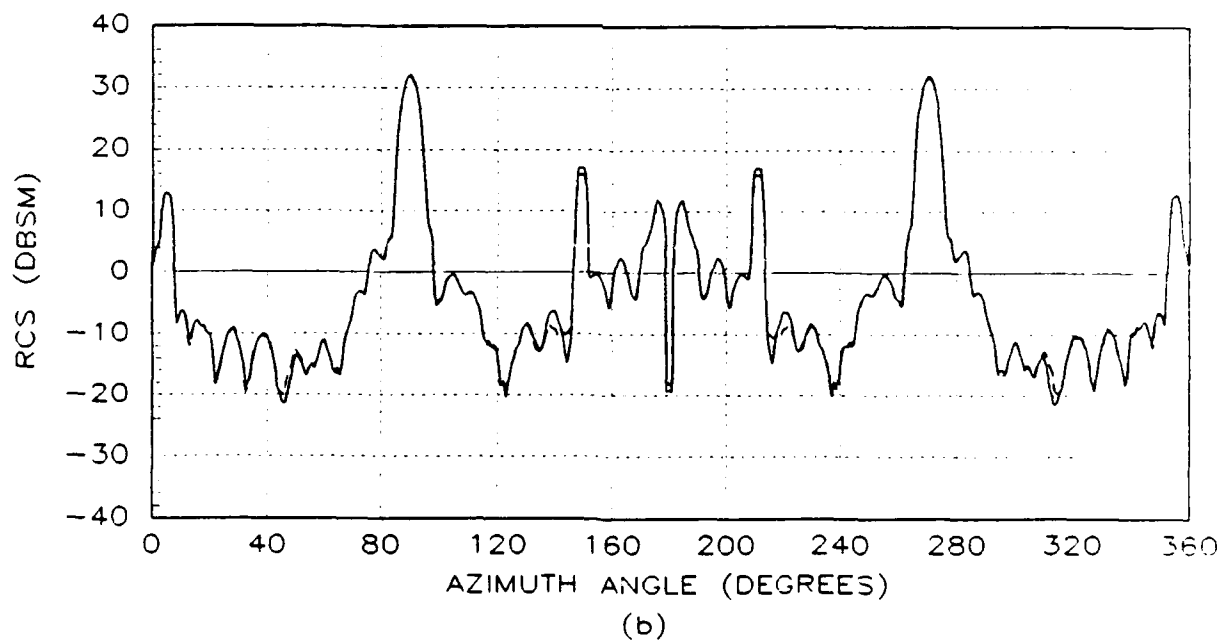
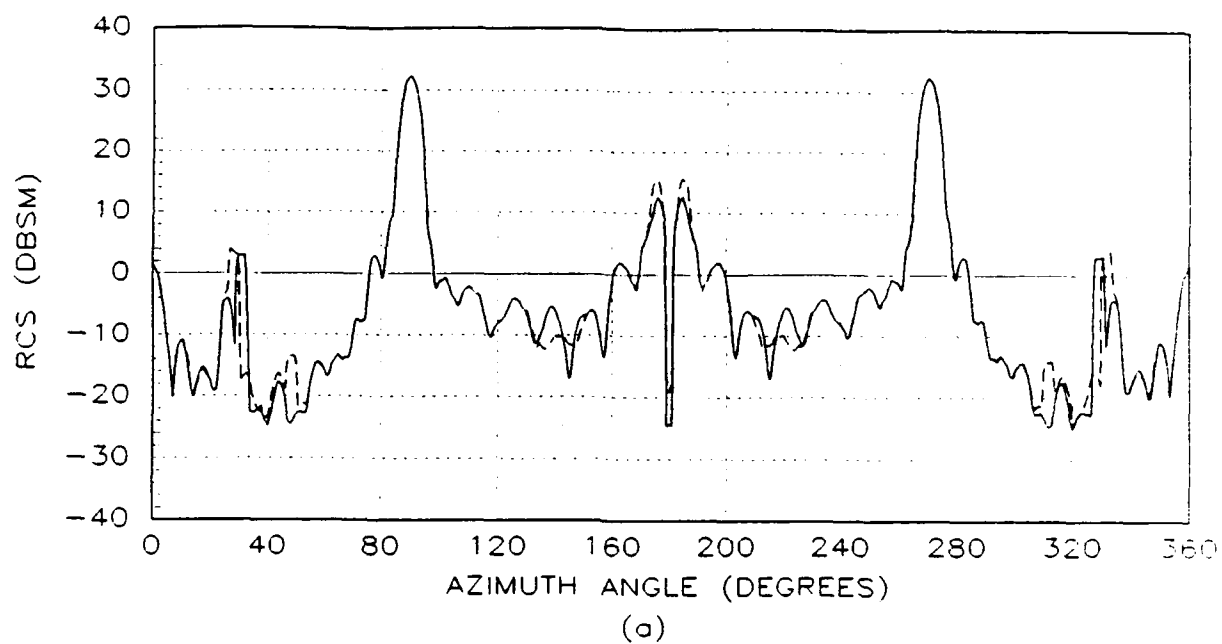
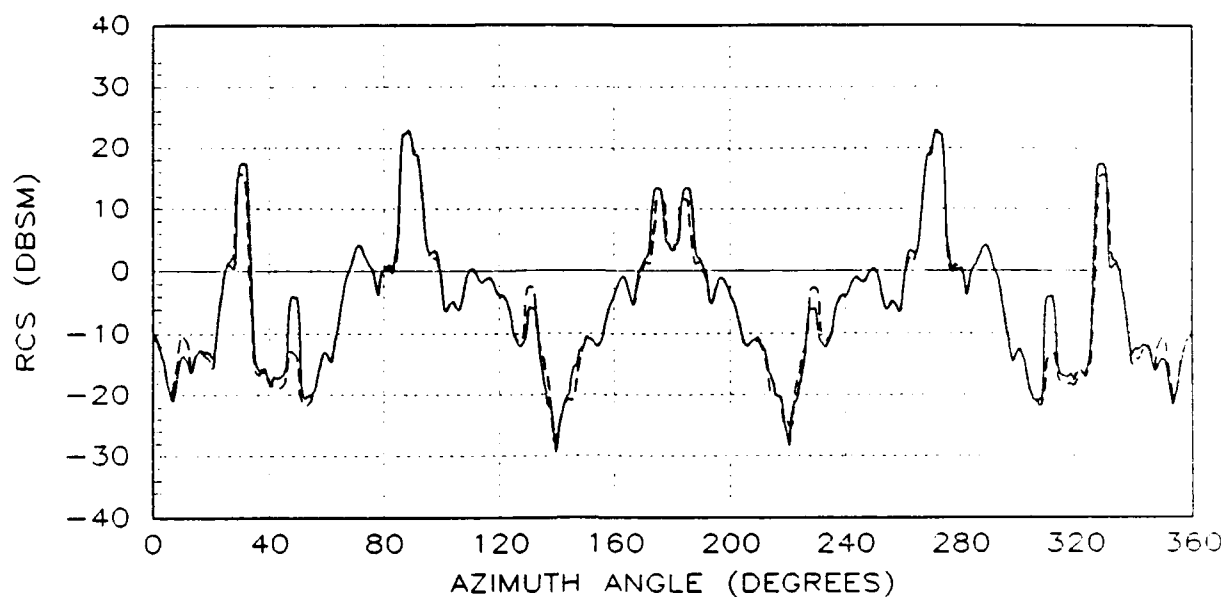
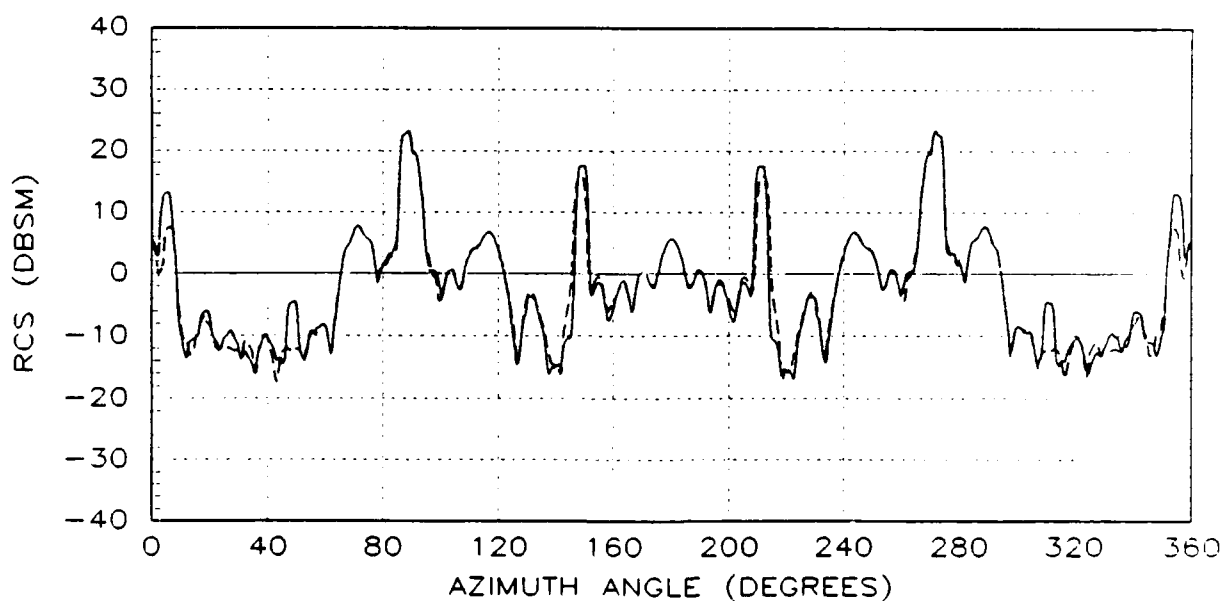


Figure A.1. Medianized, Averaged RCS Data Comparisons Between the Non-deformed (solid line) and Deformed (dashed line) T-38 Airframes for: (a) Vertical Polarization, and (b) Horizontal Polarization. 0 Degrees Elevation

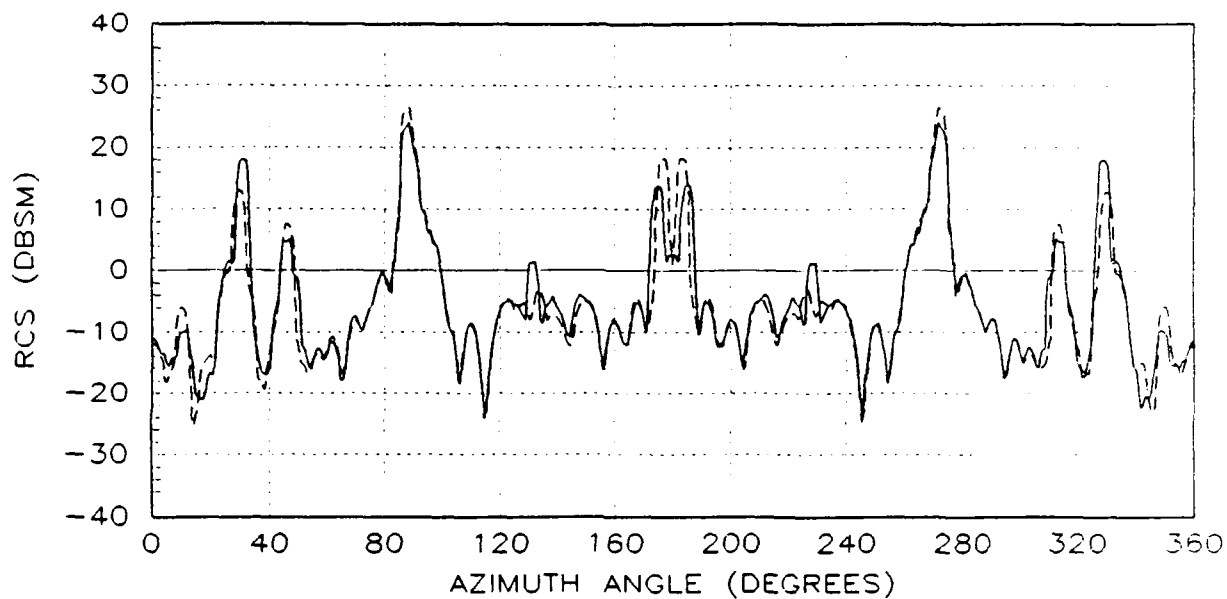


(a)

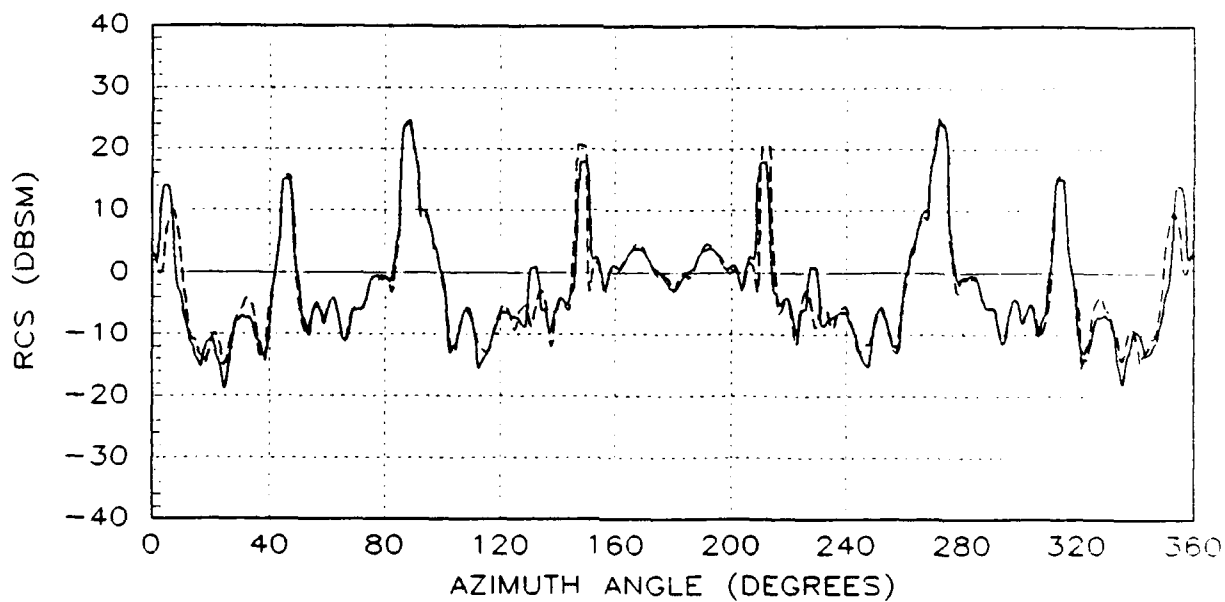


(b)

Figure A.2. Medianized, Averaged RCS Data Comparisons Between the Non-deformed (solid line) and Deformed (dashed line) T-38 Airframes for: (a) Vertical Polarization, and (b) Horizontal Polarization. 10 Degrees Elevation



(a)



(b)

Figure A.3. Medianized, Averaged RCS Data Comparisons Between the Non-deformed (solid line) and Deformed (dashed line) T-38 Airframes for: (a) Vertical Polarization, and (b) Horizontal Polarization. 20 Degrees Elevation



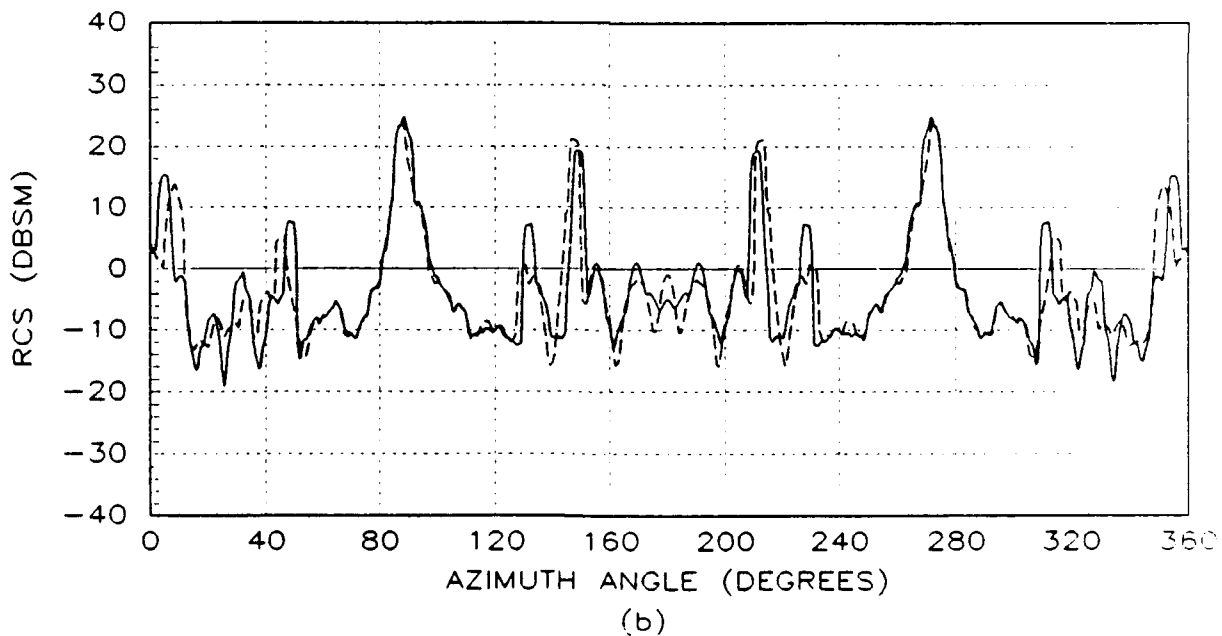
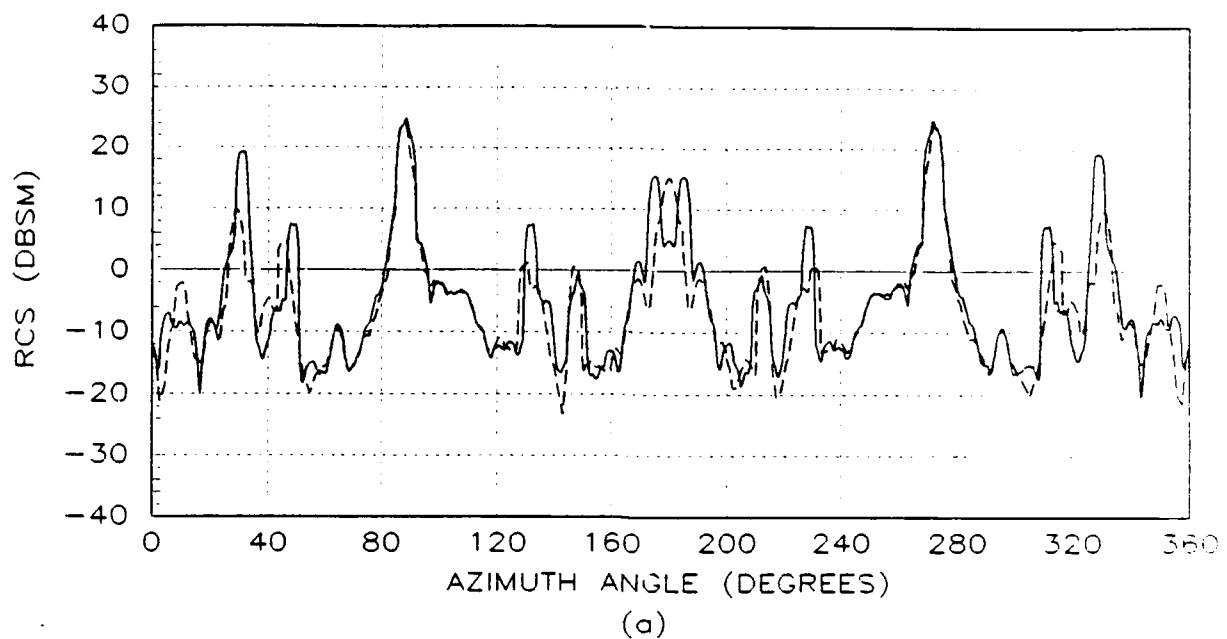


Figure A.4. Medianized, Averaged RCS Data Comparisons Between the Non-deformed (solid line) and Deformed (dashed line) T-38 Airframes for: (a) Vertical Polarization, and (b) Horizontal Polarization. 30 Degrees Elevation

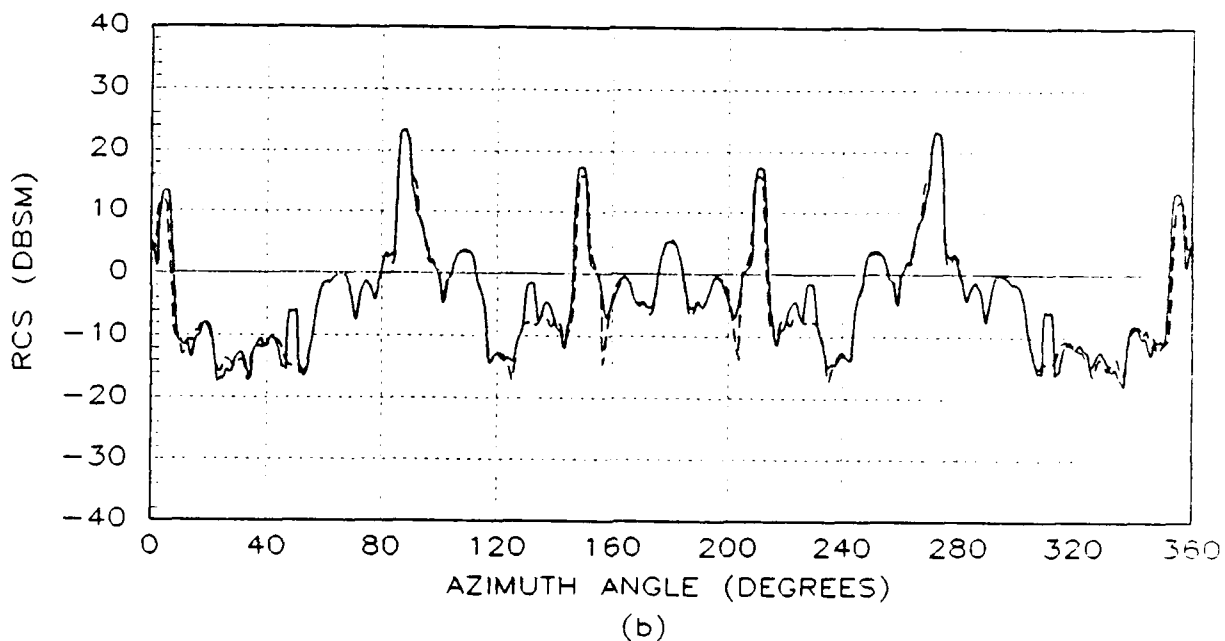
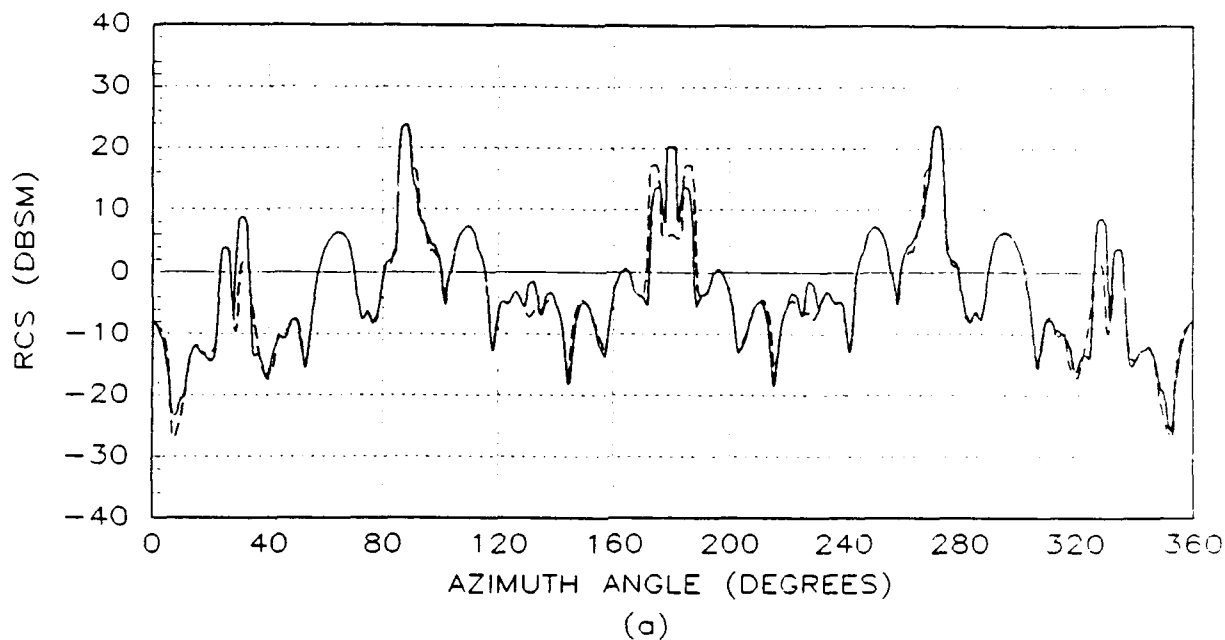


Figure A.5. Medianized, Averaged RCS Data Comparisons Between the Non-deformed (solid line) and Deformed (dashed line) T-38 Airframes for: (a) Vertical Polarization, and (b) Horizontal Polarization. -10 Degrees Elevation

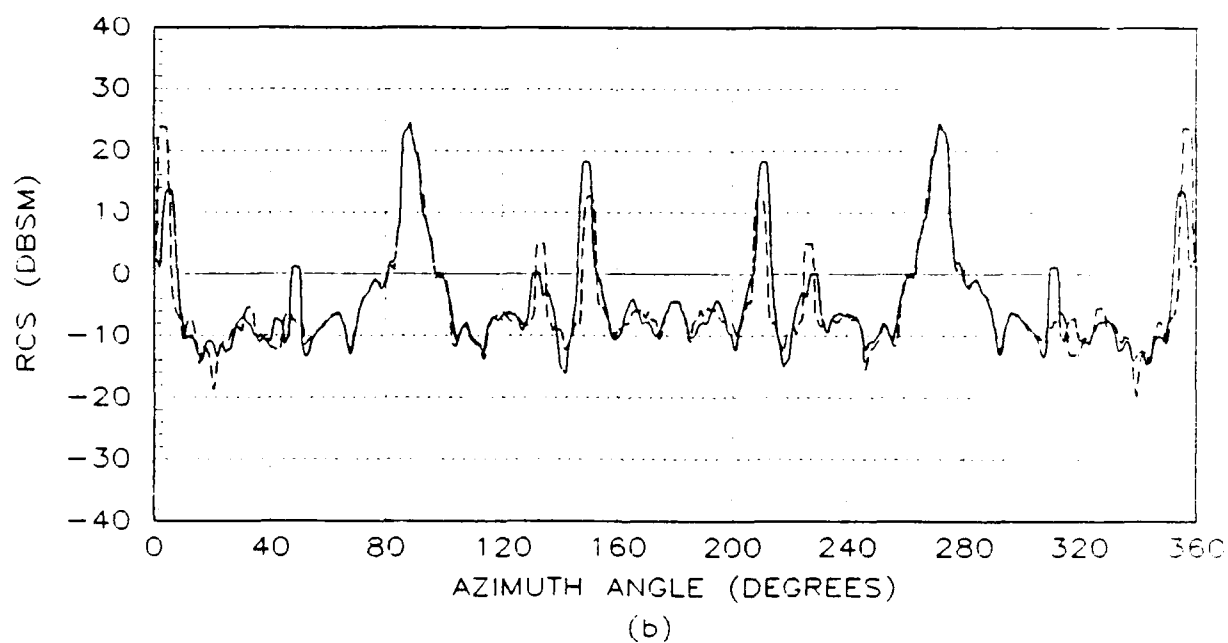
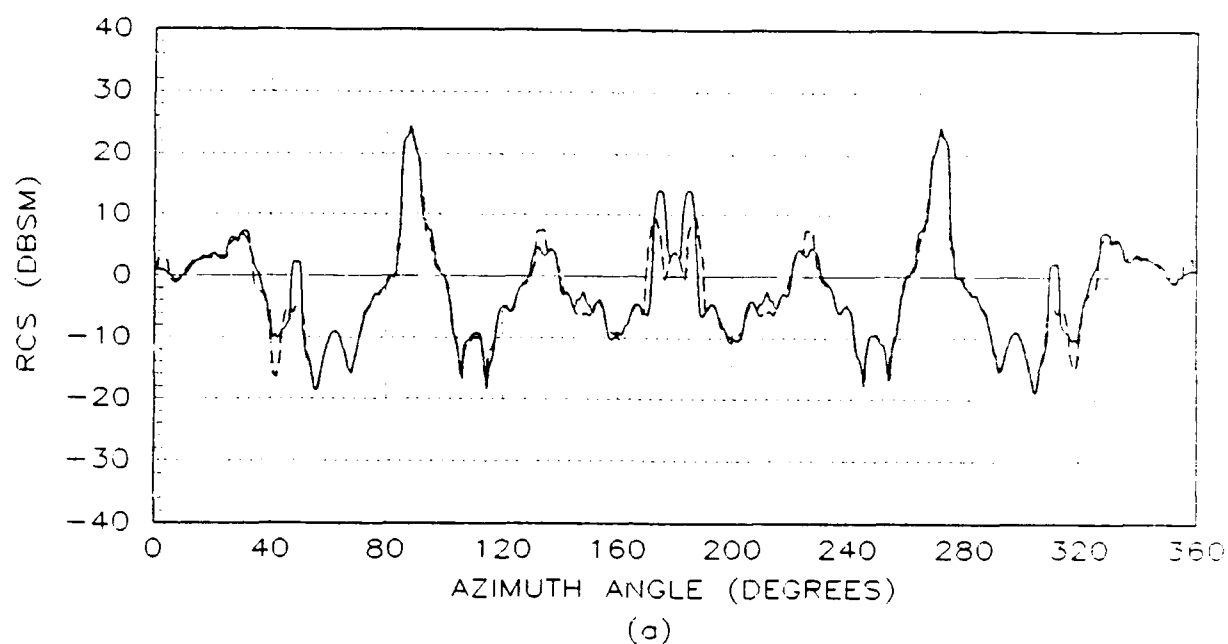
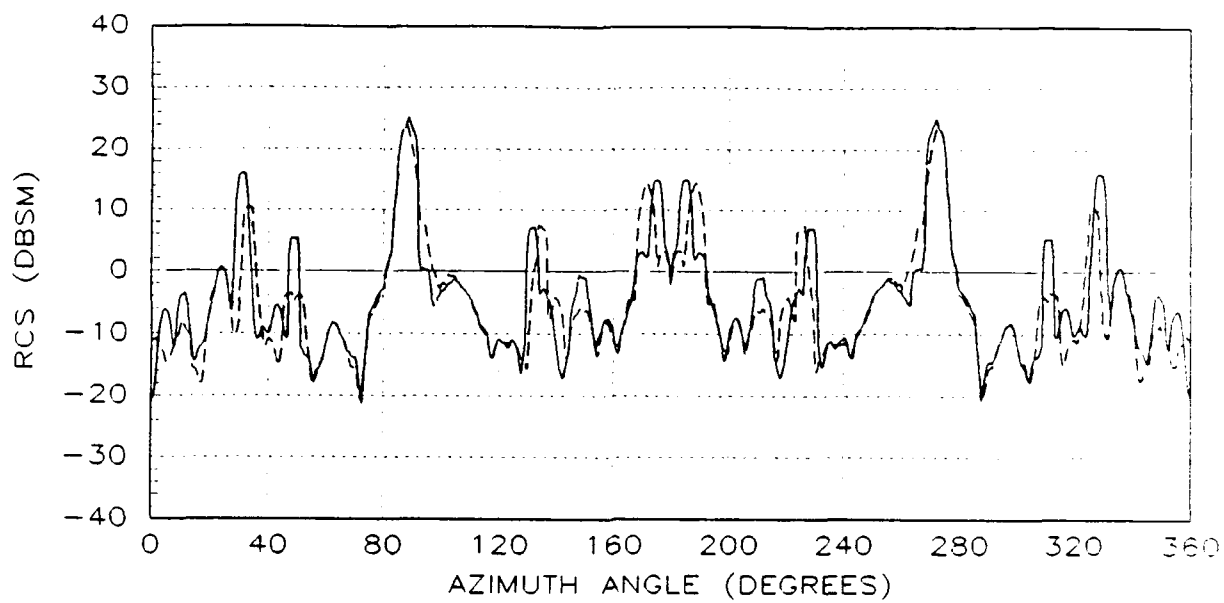
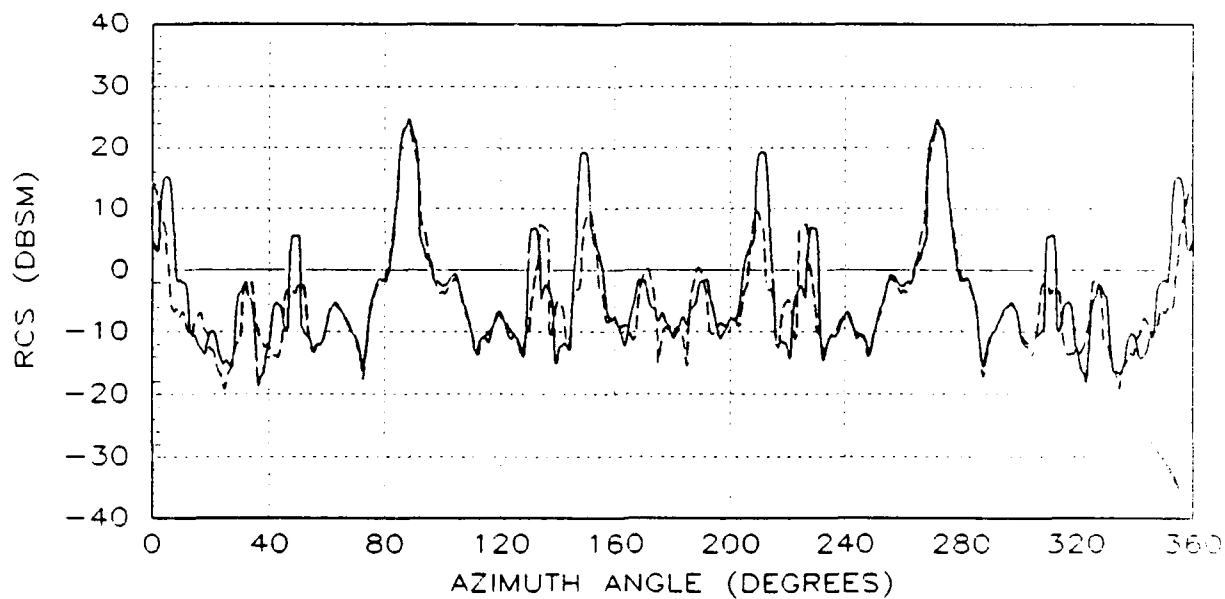


Figure A.6. Medianized, Averaged RCS Data Comparisons Between the Non-deformed (solid line) and Deformed (dashed line) T-38 Airframes for: (a) Vertical Polarization, and (b) Horizontal Polarization. -20 Degrees Elevation



(a)



(b)

Figure A.7. Medianized, Averaged RCS Data Comparisons Between the Non-deformed (solid line) and Deformed (dashed line) T-38 Airframes for: (a) Vertical Polarization, and (b) Horizontal Polarization. -30 Degrees Elevation

## Appendix B

This Appendix contains the medianized, averaged computed RCS data for the non-deformed versus deformed C-5A airframes. Data for both the positive symmetric maneuver (PSM) and negative symmetric maneuver (NSM) is presented for horizontal and vertical field polarizations. As in Appendix A, the nose of the aircraft is located at 180 degrees and the non-deformed data is represented by solid lines. The illuminating frequency is 10 GHz for the 1/10th scale model of the C-5A airframe.

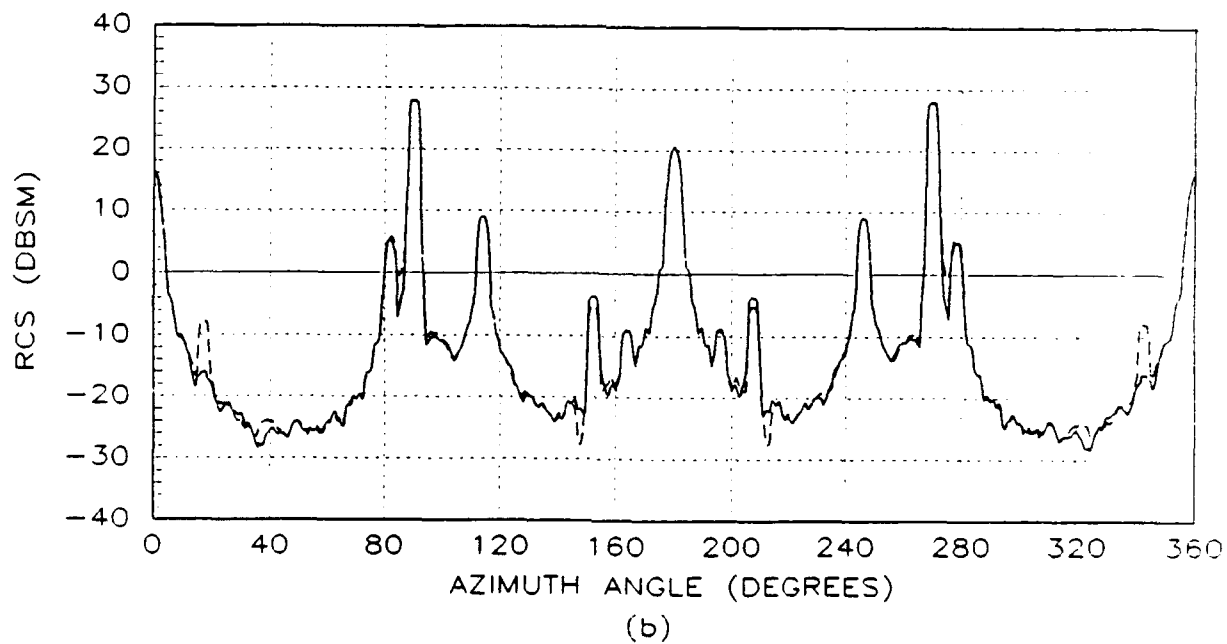
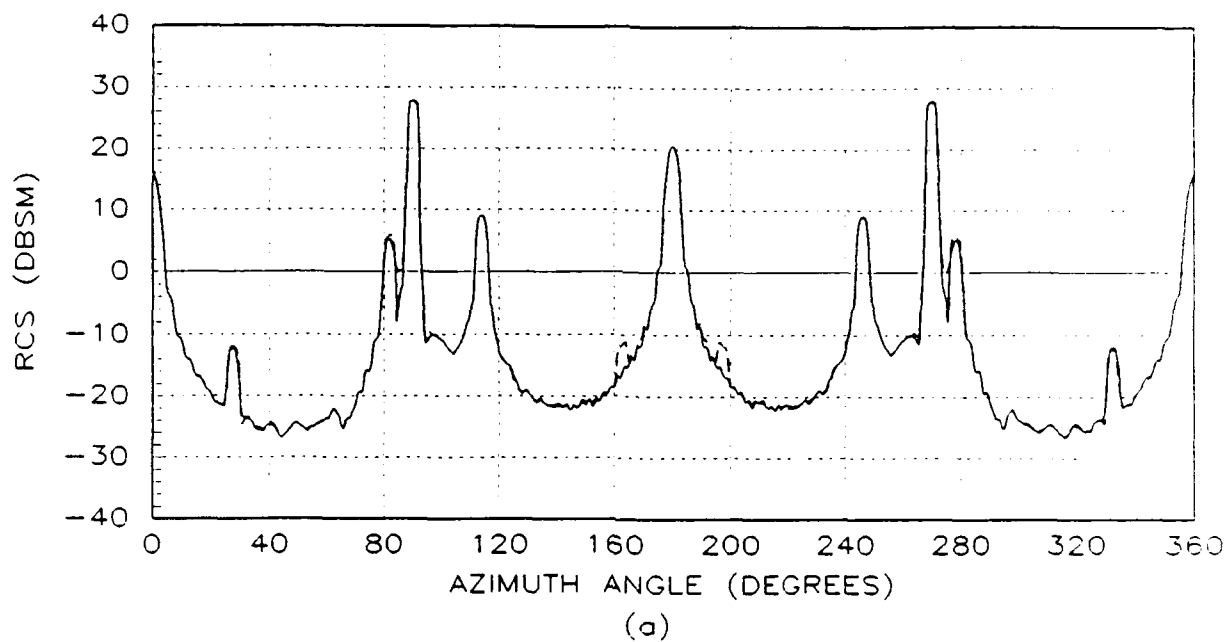


Figure B.1. Medianized, Averaged RCS Data Comparisons for the Non-deformed (solid line) versus Deformed (dashed line) C-5A Airframes for: (a) Vertical Polarization, and (b) Horizontal Polarization. PSM : 0 Degrees Elevation

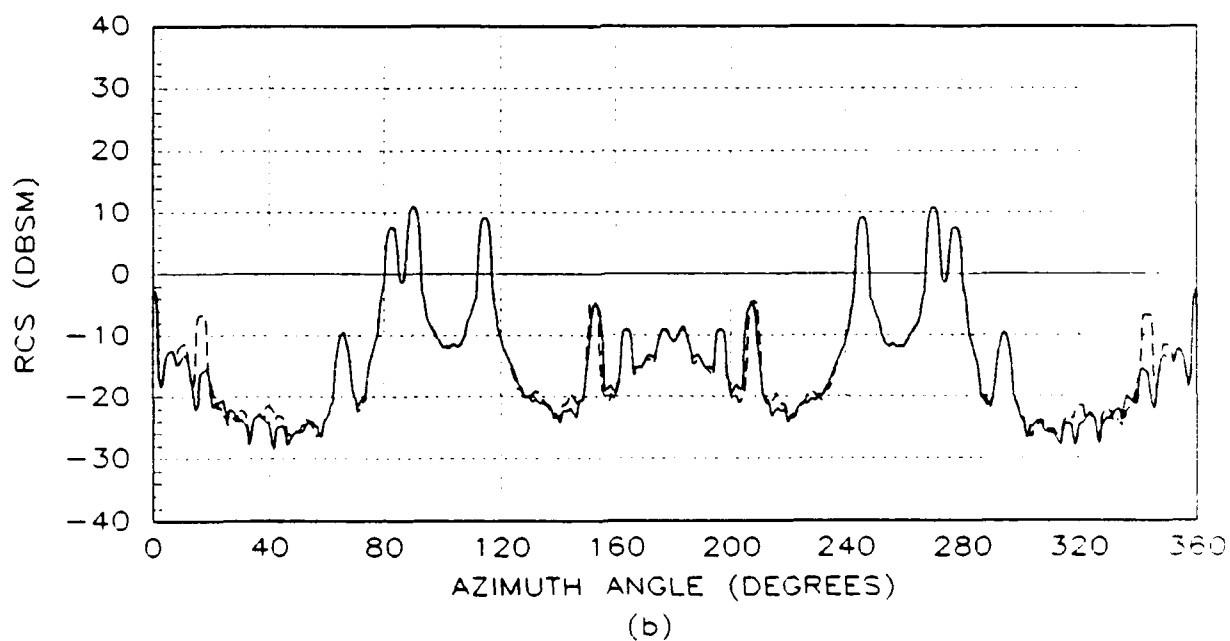
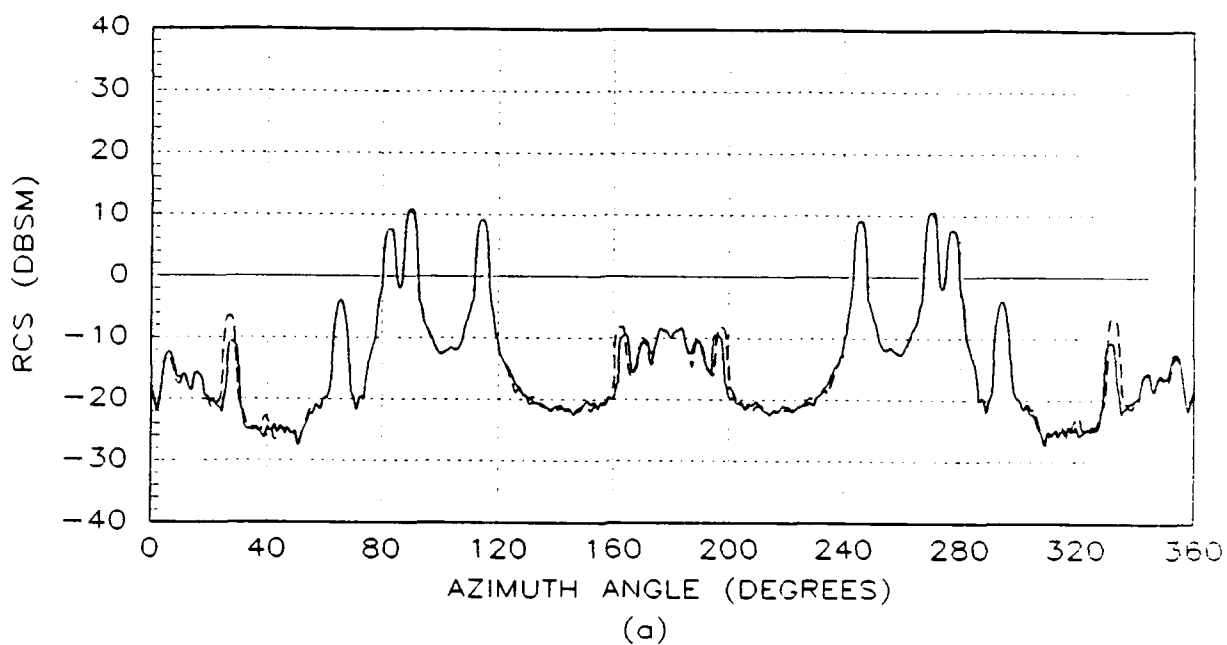


Figure B.2. Medianized, Averaged RCS Data Comparisons for the Non-deformed (solid line) versus Deformed (dashed line) C-5A Airframes for: (a) Vertical Polarization, and (b) Horizontal Polarization. PSM : 10 Degrees Elevation

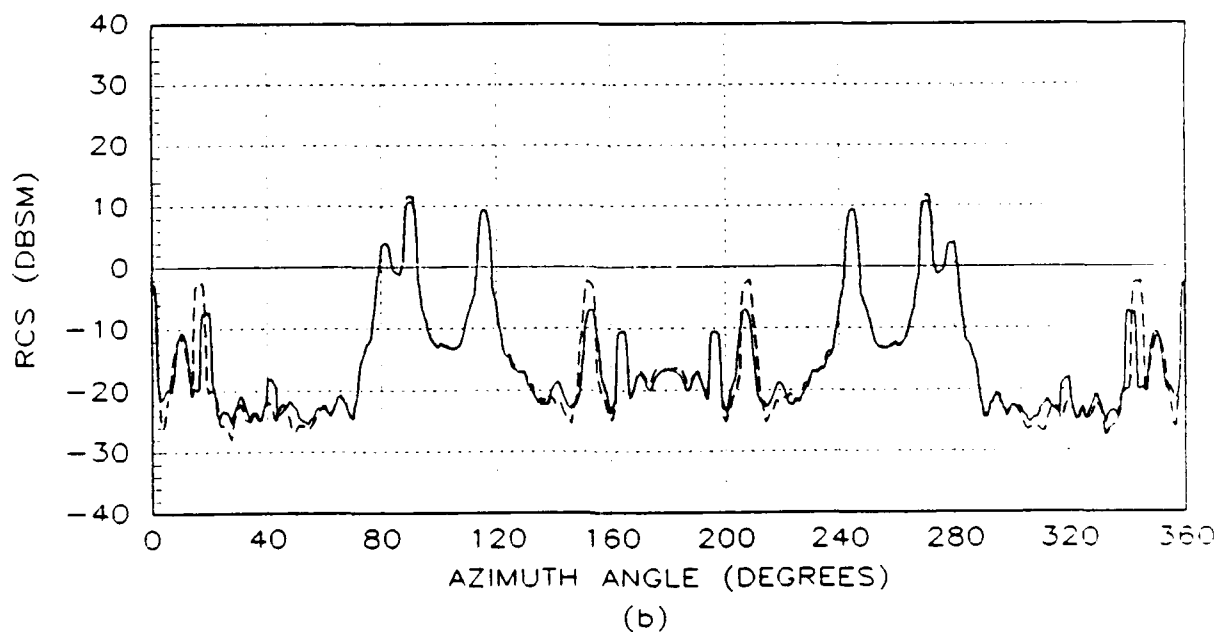
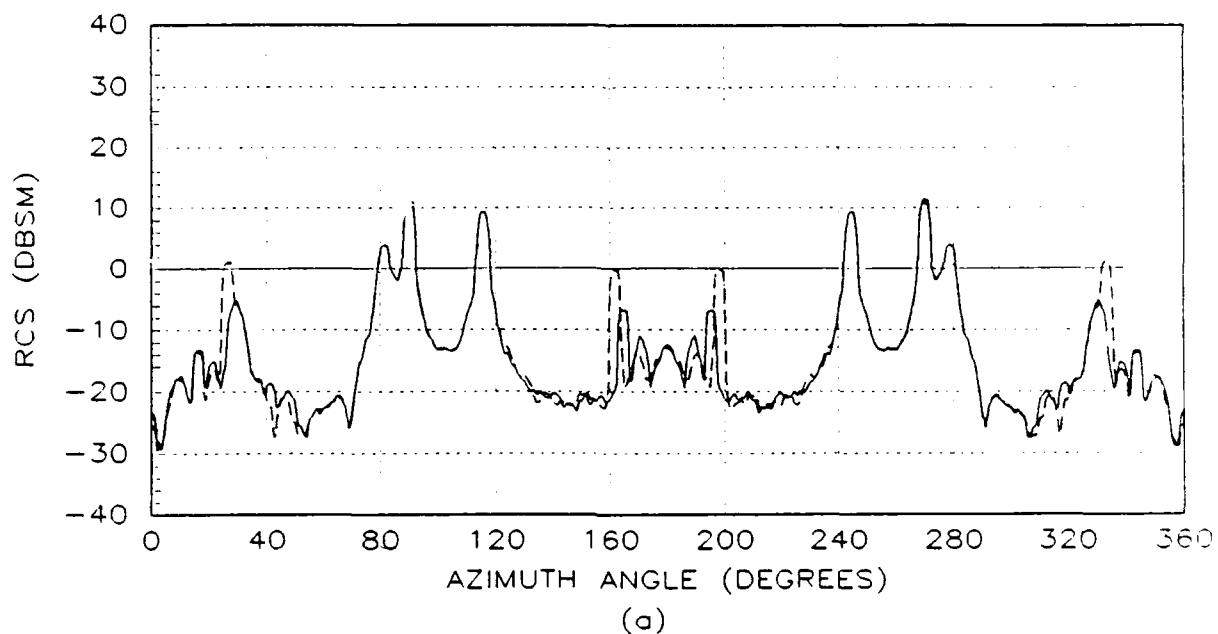


Figure B.3. Medianized, Averaged RCS Data Comparisons for the Non-deformed (solid line) versus Deformed (dashed line) C-5A Airframes for: (a) Vertical Polarization, and (b) Horizontal Polarization. PSM : 20 Degrees Elevation



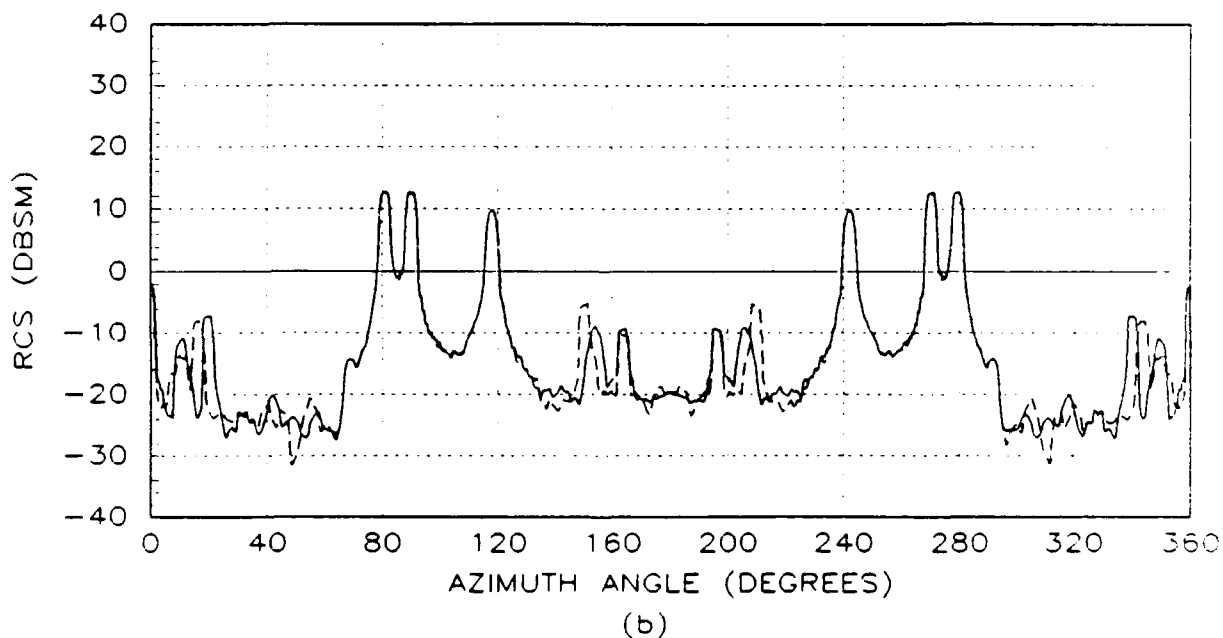
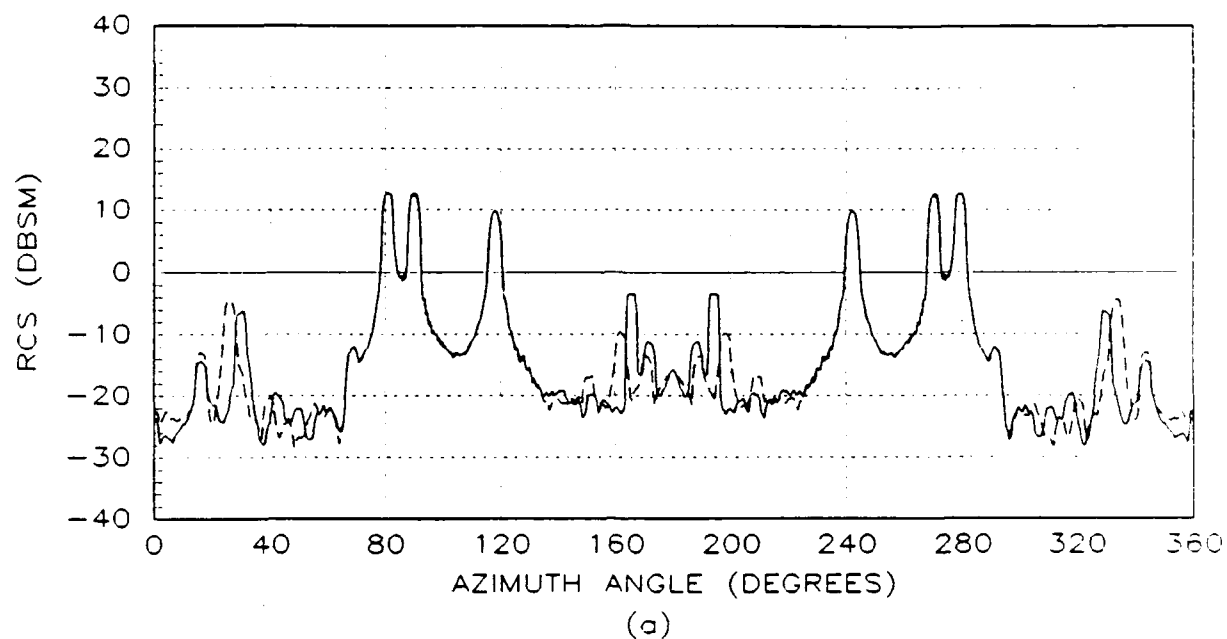


Figure B.4. Medianized, Averaged RCS Data Comparisons for the Non-deformed (solid line) versus Deformed (dashed line) C-5A Airframes for: (a) Vertical Polarization, and (b) Horizontal Polarization. PSM : 30 Degrees Elevation

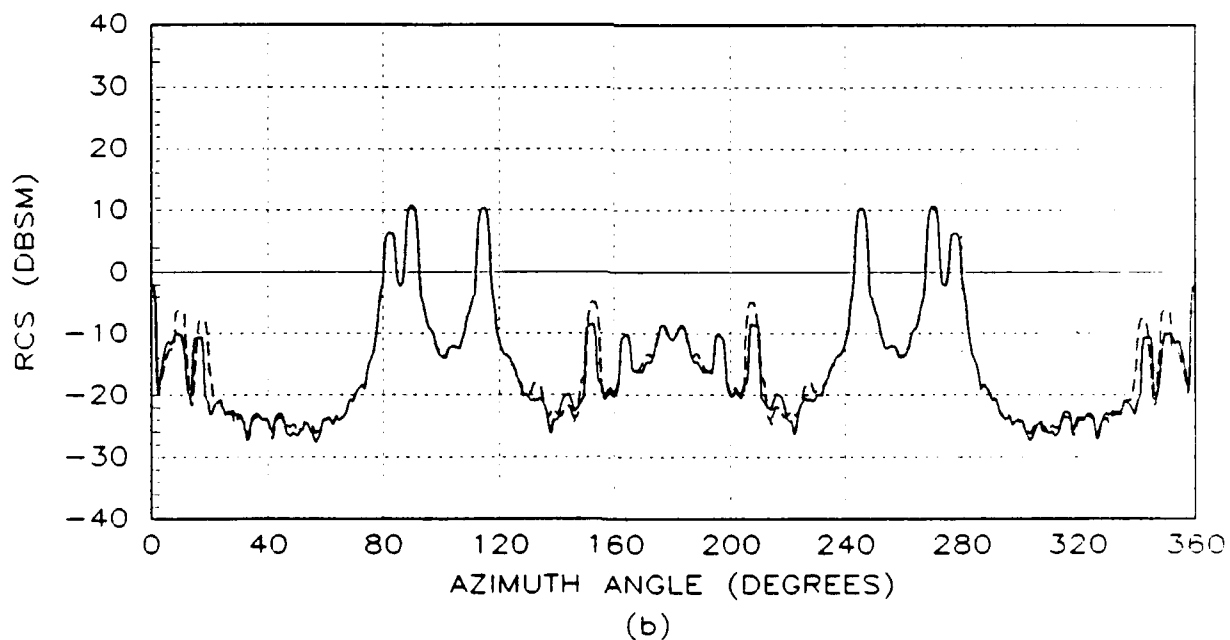
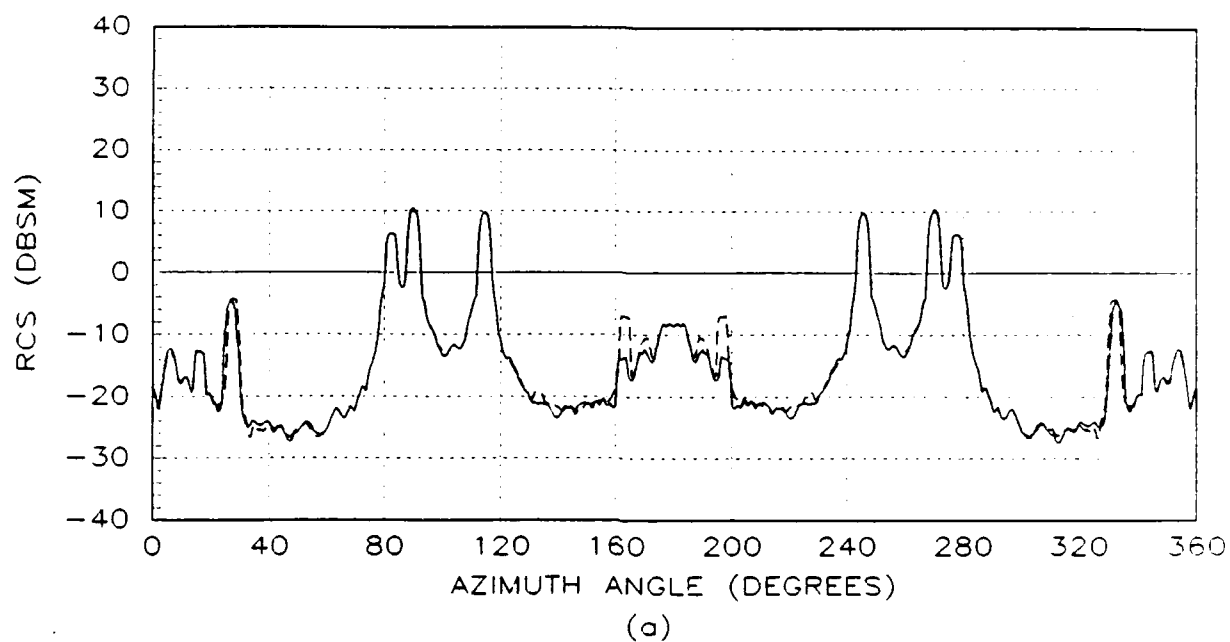


Figure B.5. Medianized, Averaged RCS Data Comparisons for the Non-deformed (solid line) versus Deformed (dashed line) C-5A Airframes for: (a) Vertical Polarization, and (b) Horizontal Polarization. PSM : -10 Degrees Elevation

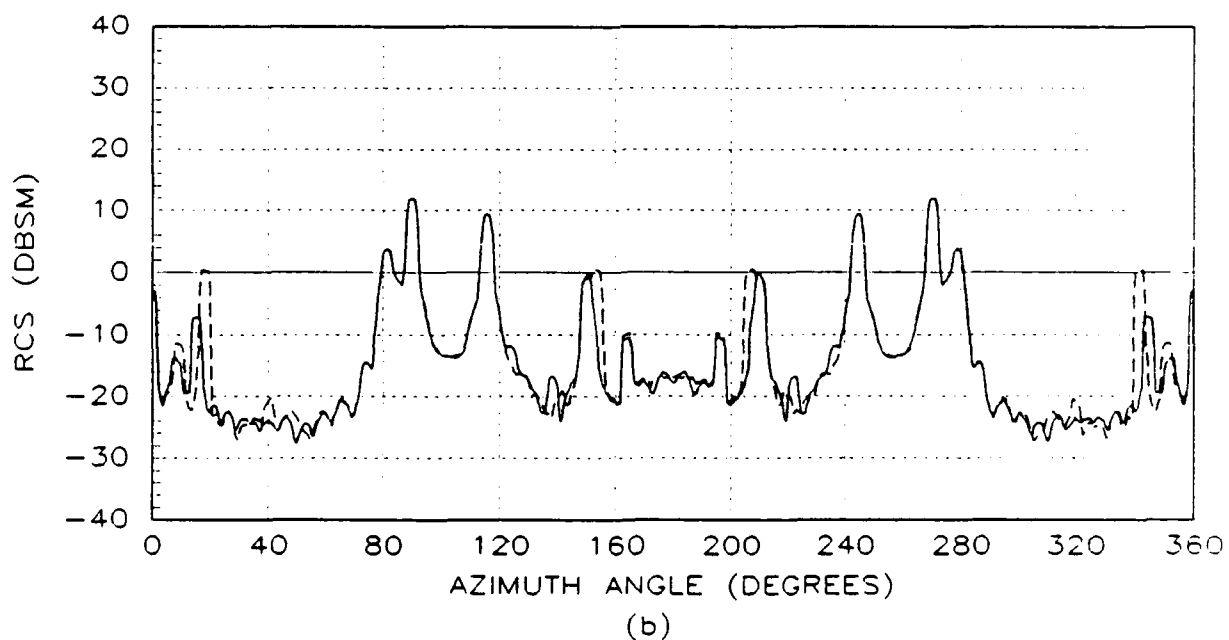
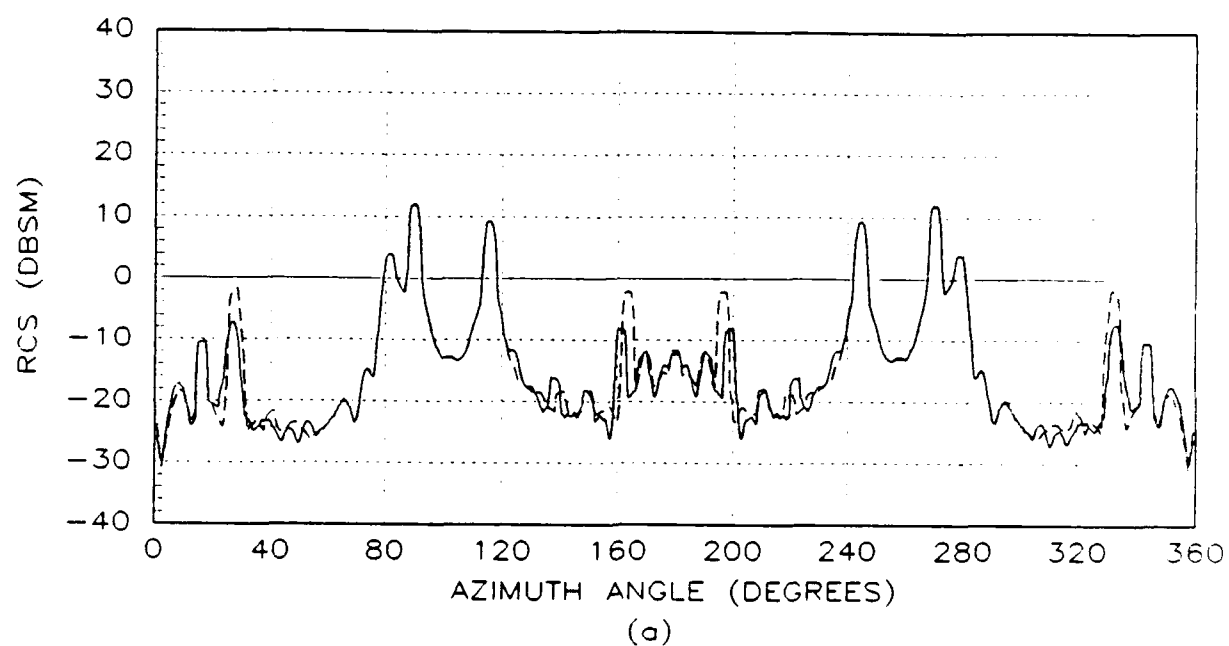


Figure B.6. Medianized, Averaged RCS Data Comparisons for the Non-deformed (solid line) versus Deformed (dashed line) C-5A Airframes for: (a) Vertical Polarization, and (b) Horizontal Polarization. PSM : -20 Degrees Elevation

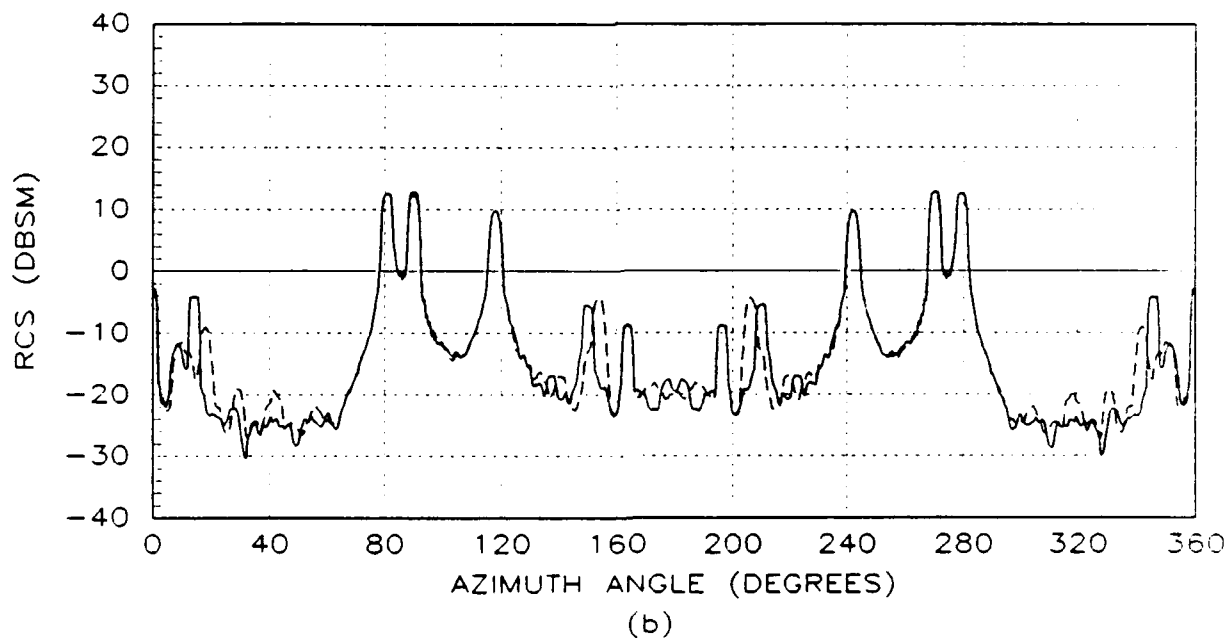
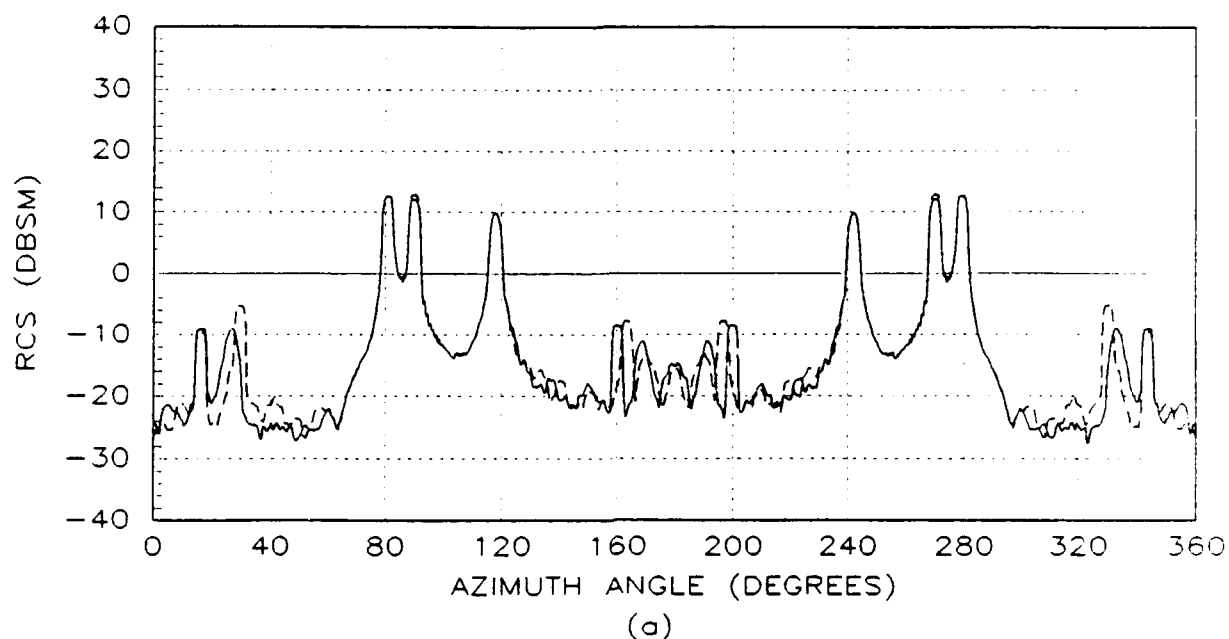
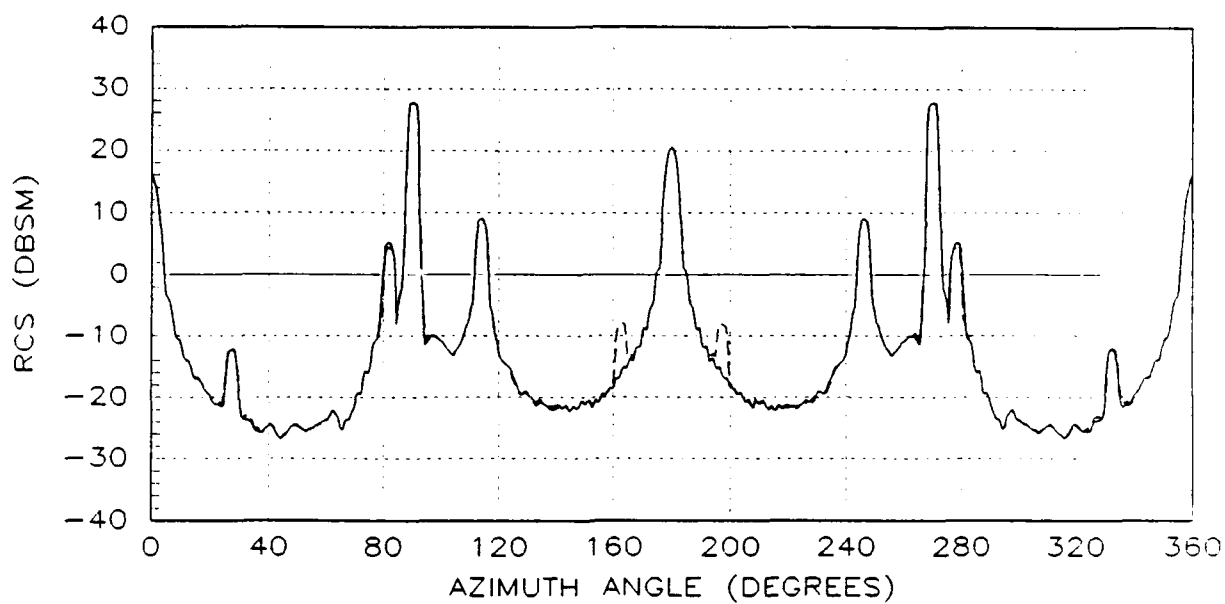
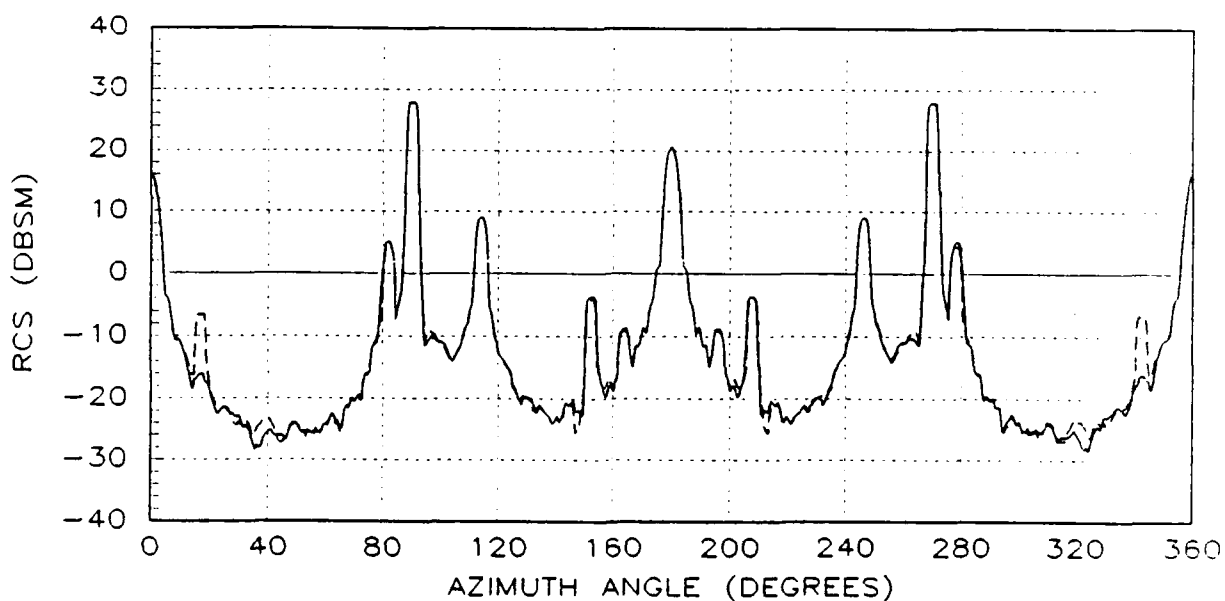


Figure B.7. Medianized, Averaged RCS Data Comparisons for the Non-deformed (solid line) versus Deformed (dashed line) C-5A Airframes for: (a) Vertical Polarization, and (b) Horizontal Polarization. PSM : -30 Degrees Elevation



(a)



(b)

Figure B.8. Medianized, Averaged RCS Data Comparisons for the Non-deformed (solid line) versus Deformed (dashed line) C-5A Airframes for: (a) Vertical Polarization, and (b) Horizontal Polarization. NSM : 0 Degrees Elevation

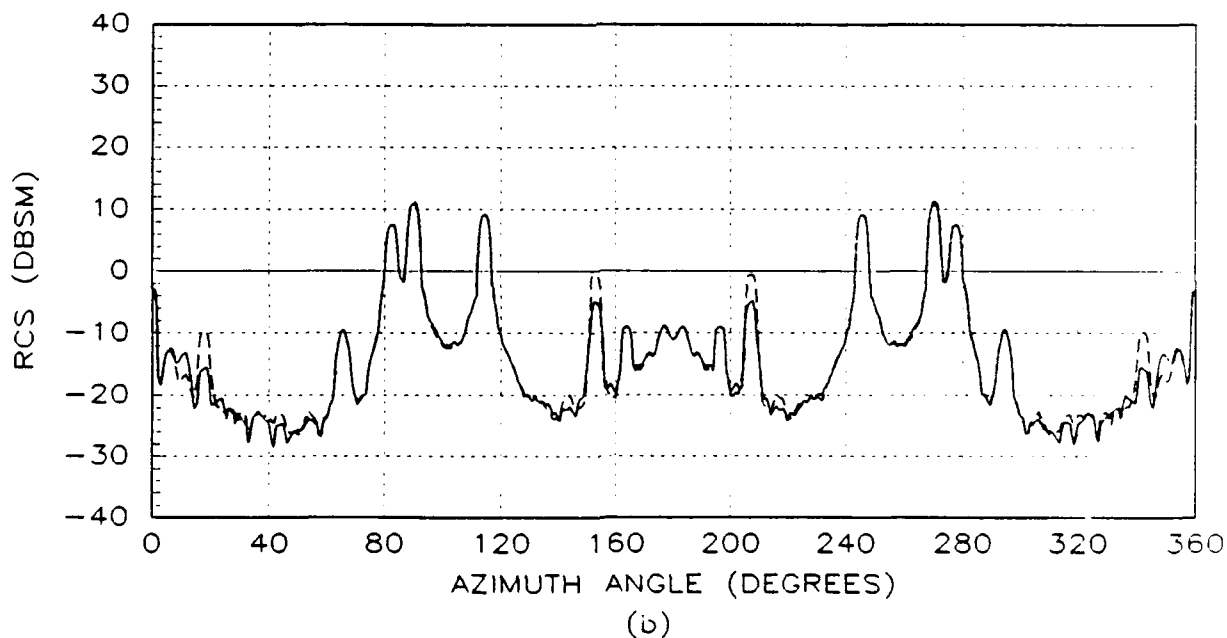
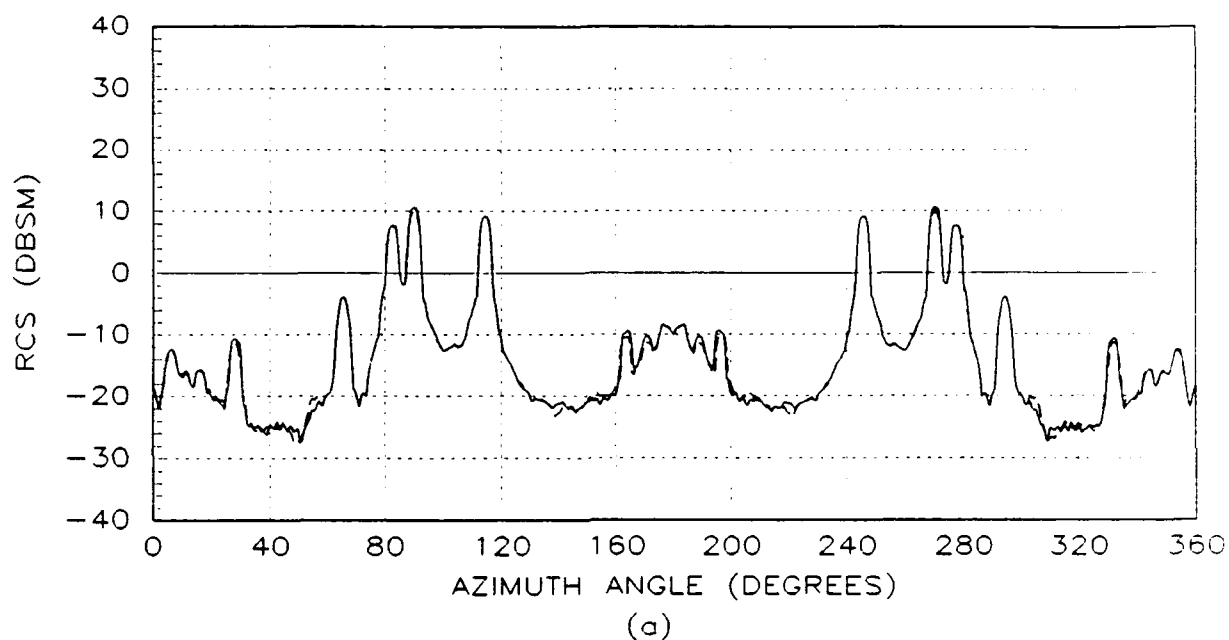


Figure B.9. Medianized, Averaged RCS Data Comparisons for the Non-deformed (solid line) versus Deformed (dashed line) C-5A Airframes for: (a) Vertical Polarization, and (b) Horizontal Polarization. NSM : 10 Degrees Elevation

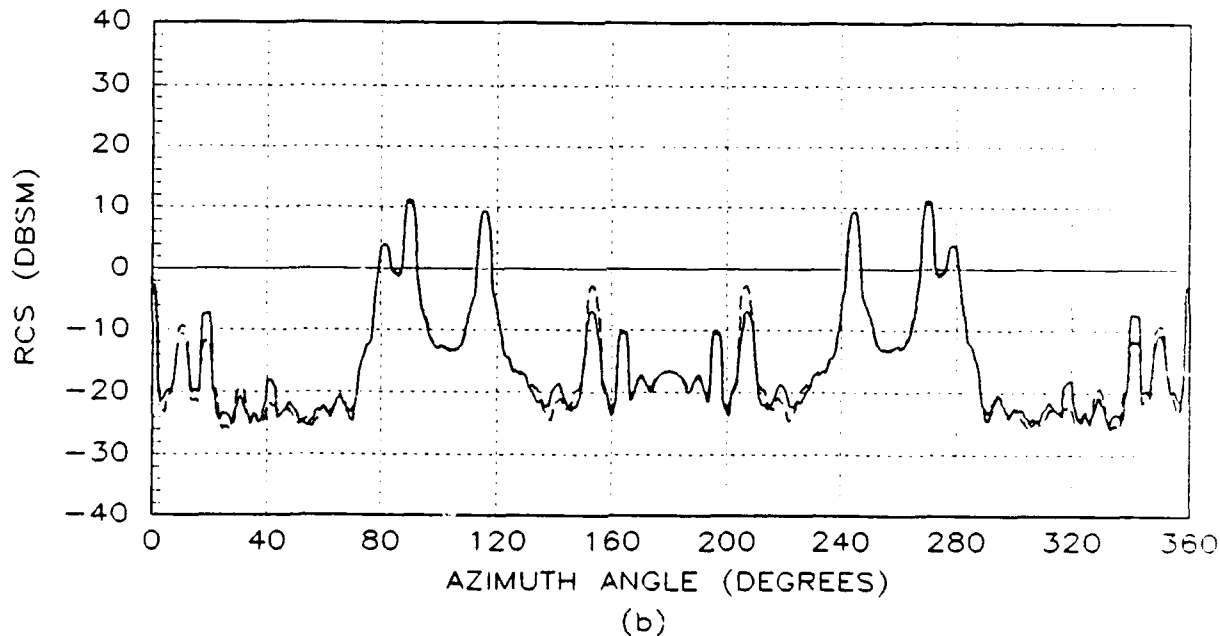
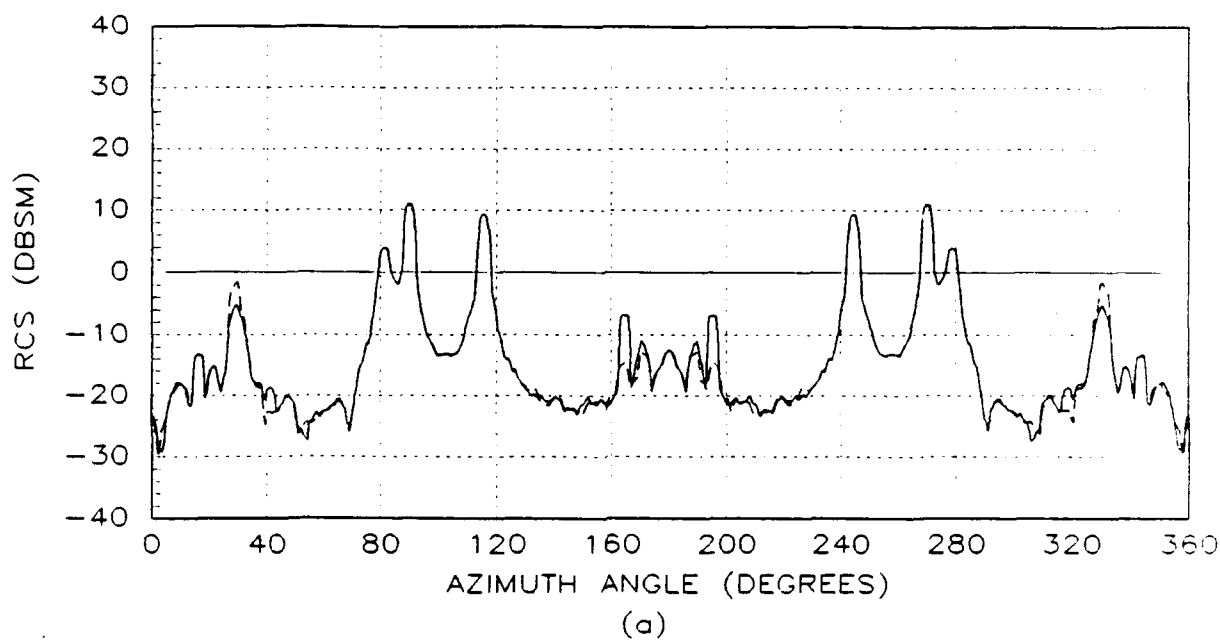


Figure B.10. Medianized, Averaged RCS Data Comparisons for the Non-deformed (solid line) versus Deformed (dashed line) C-5A Airframes for: (a) Vertical Polarization, and (b) Horizontal Polarization. NSM : 20 Degrees Elevation

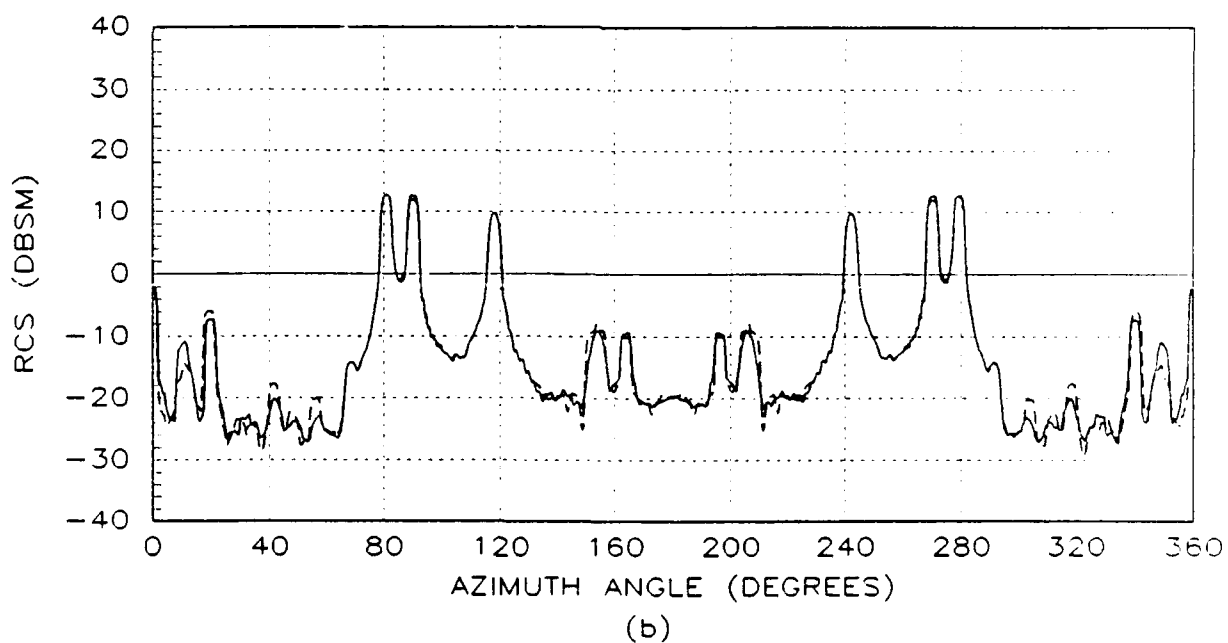
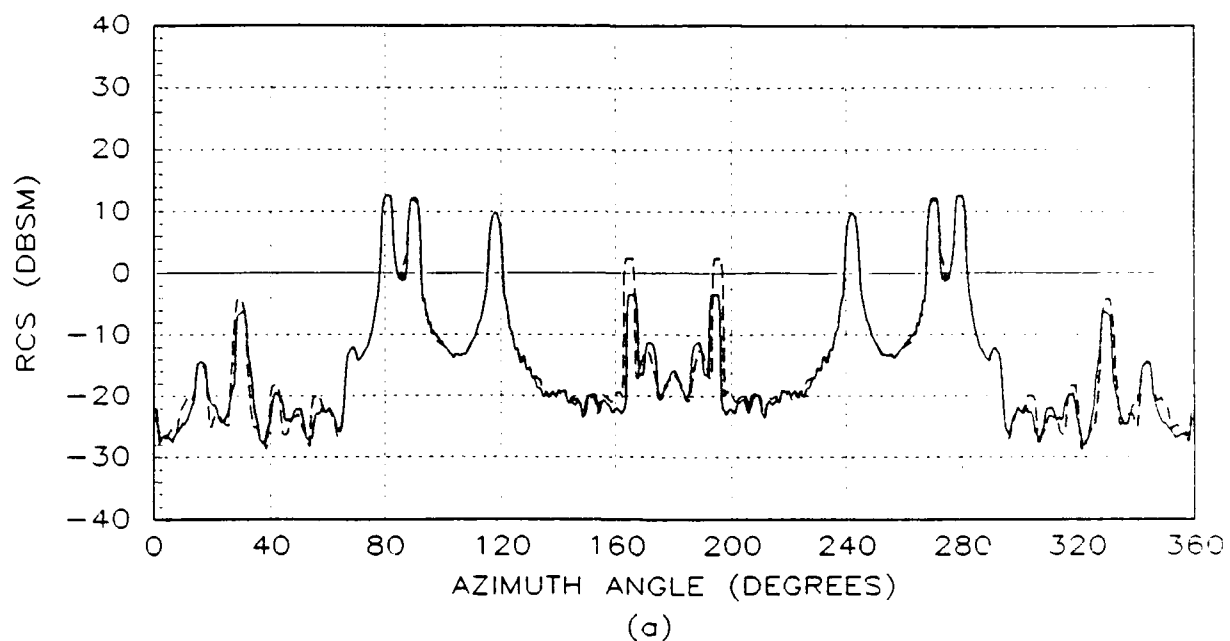


Figure B.11. Medianized, Averaged RCS Data Comparisons for the Non-deformed (solid line) versus Deformed (dashed line) C-5A Airframes for: (a) Vertical Polarization, and (b) Horizontal Polarization. NSM : 30 Degrees Elevation



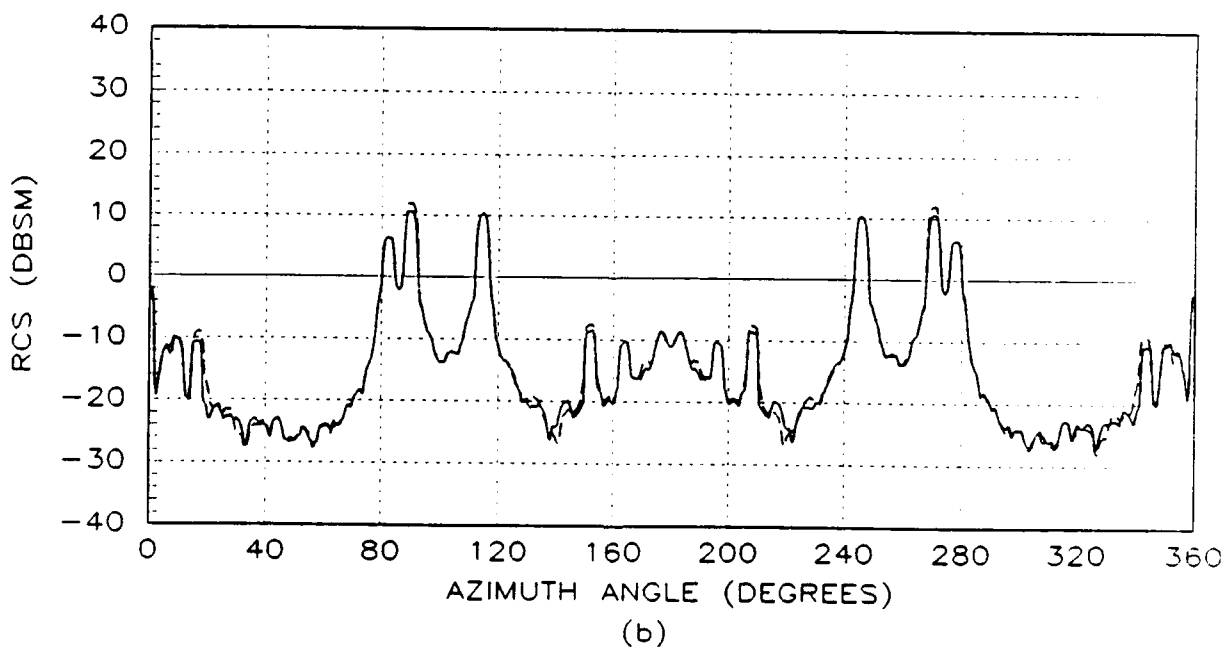
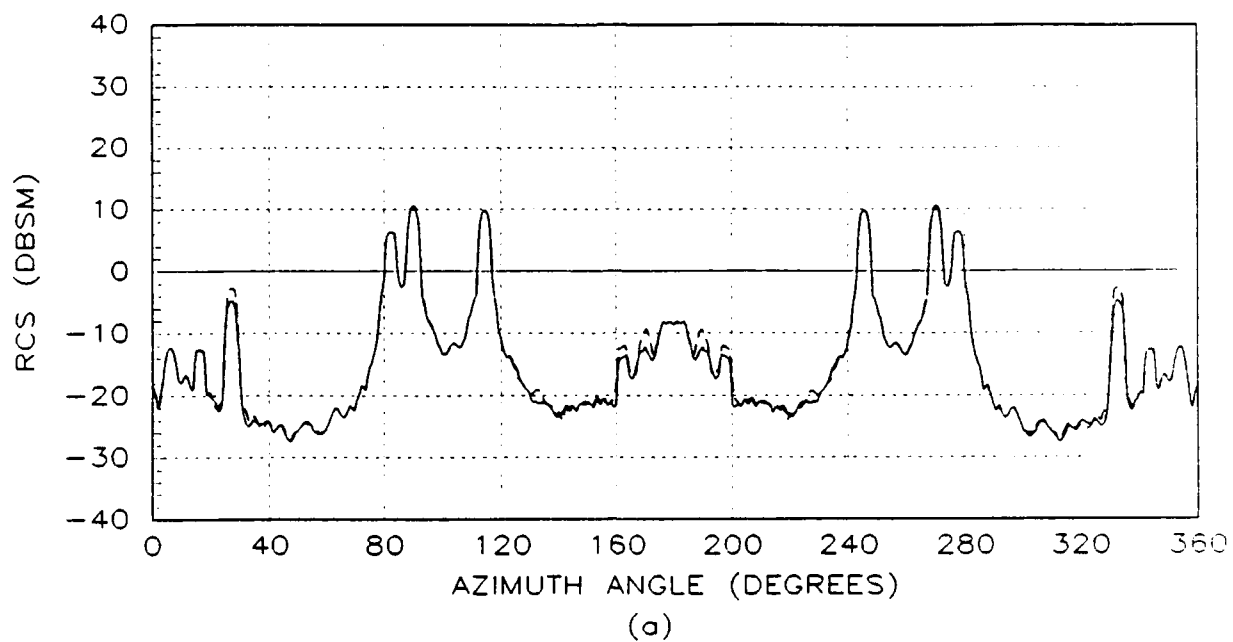


Figure B.12. Medianized, Averaged RCS Data Comparisons for the Non-deformed (solid line) versus Deformed (dashed line) C-5A Airframes for: (a) Vertical Polarization, and (b) Horizontal Polarization. NSM : -10 Degrees Elevation

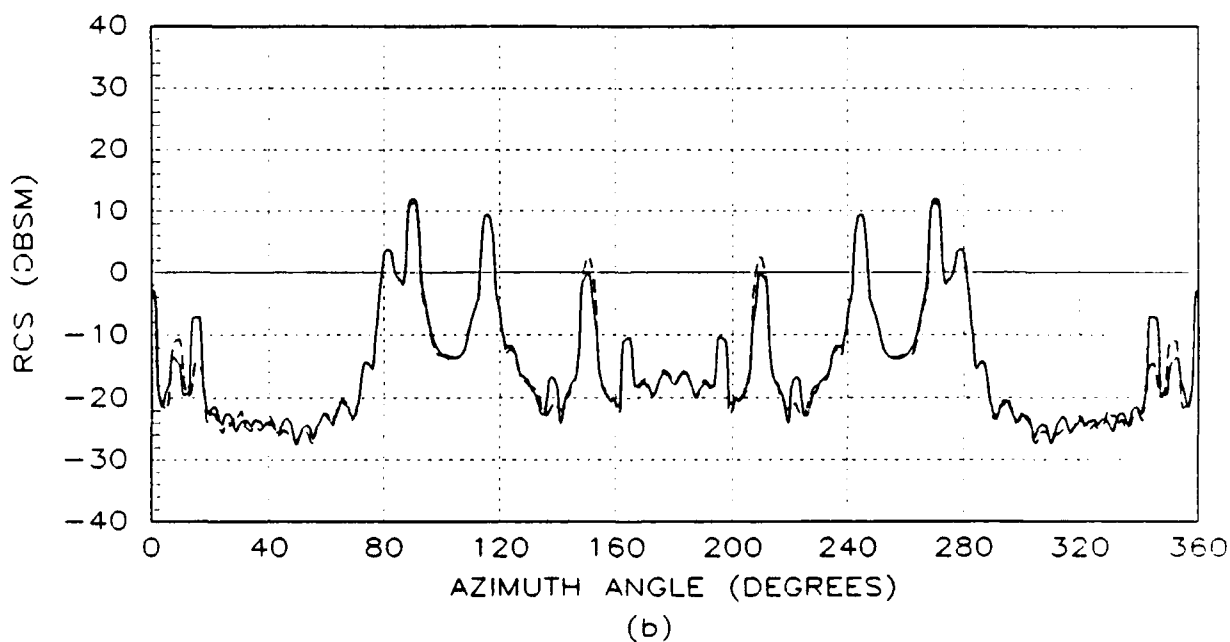
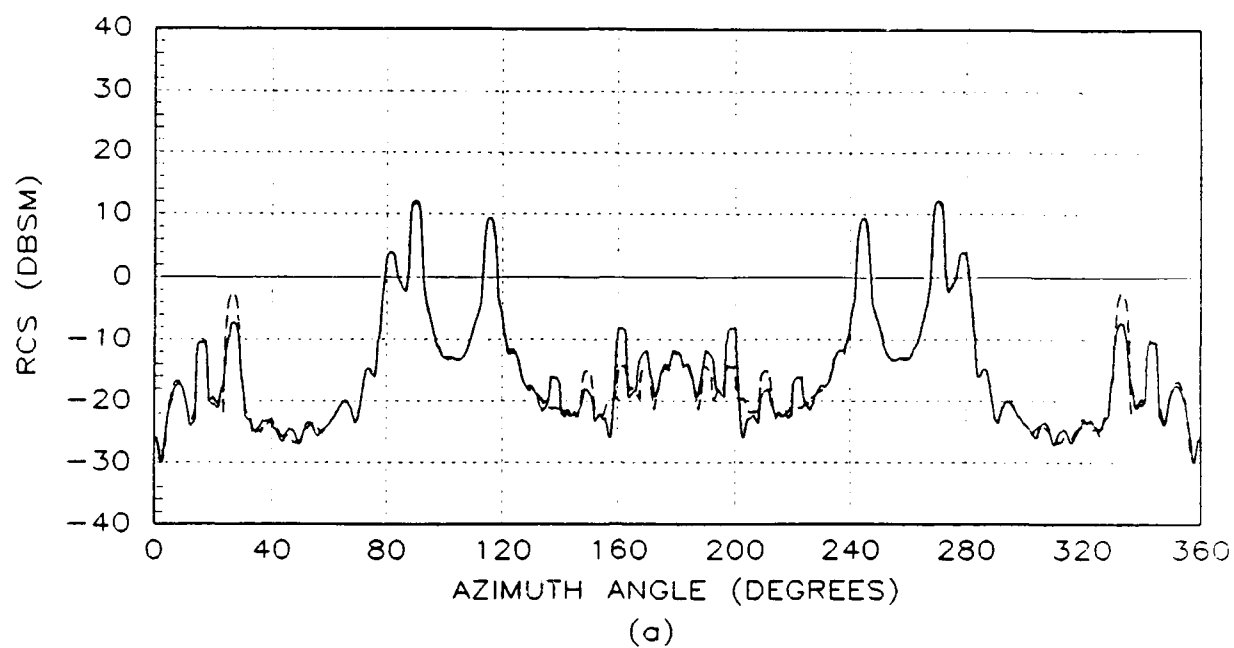


Figure B.13. Medianized, Averaged RCS Data Comparisons for the Non-deformed (solid line) versus Deformed (dashed line) C-5A Airframes for: (a) Vertical Polarization, and (b) Horizontal Polarization. NSM : -20 Degrees Elevation

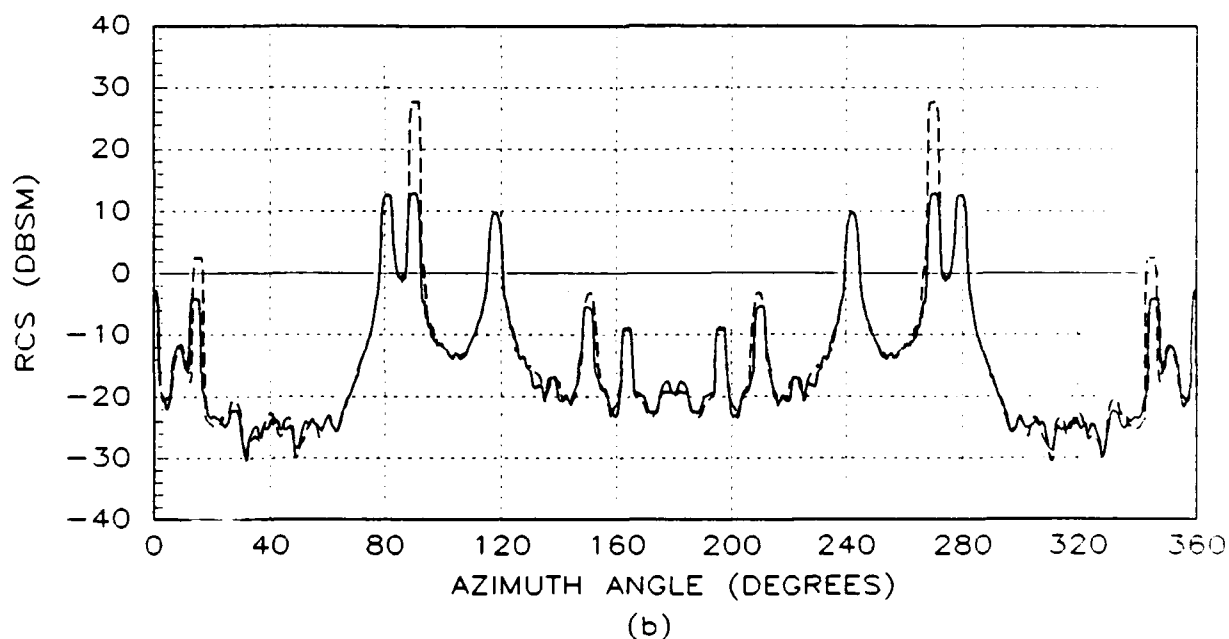
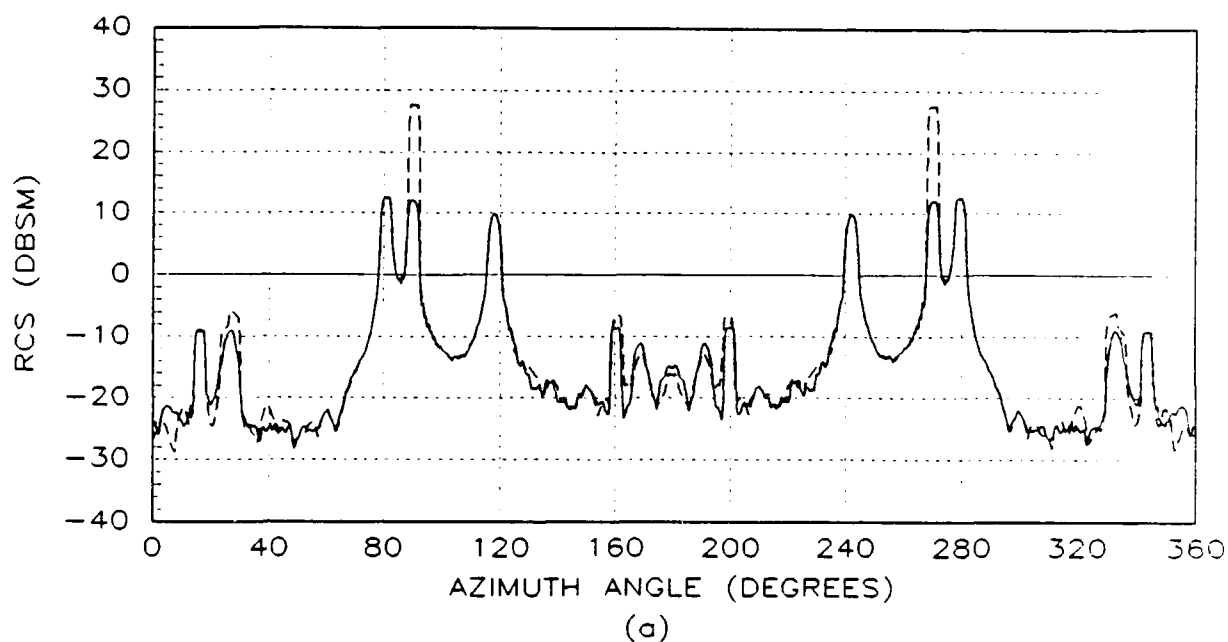
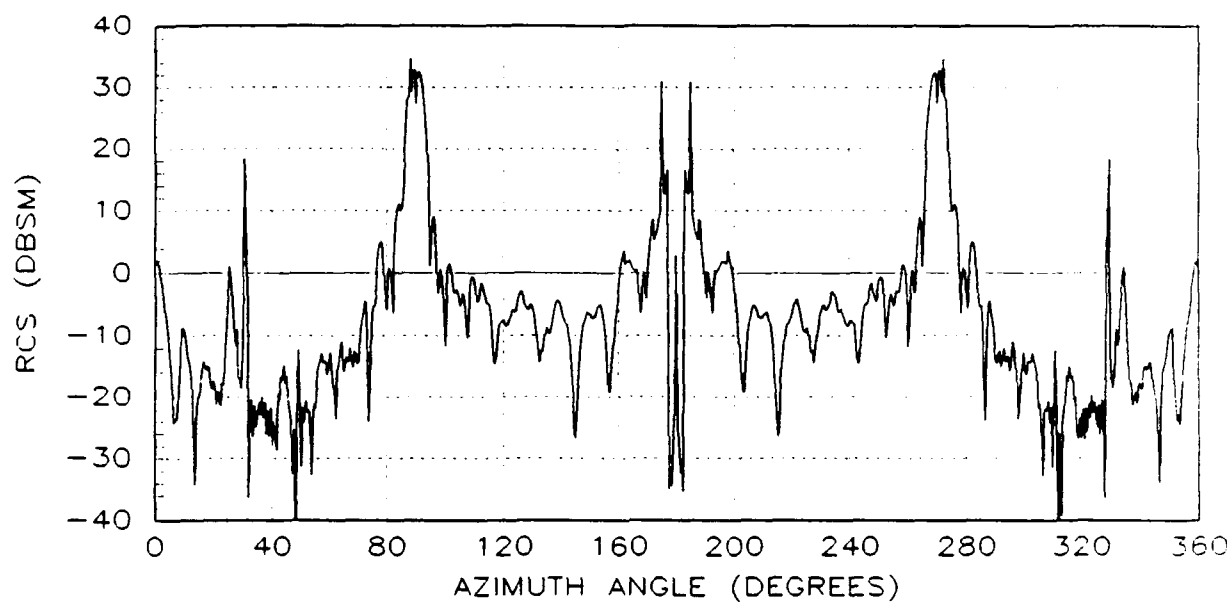


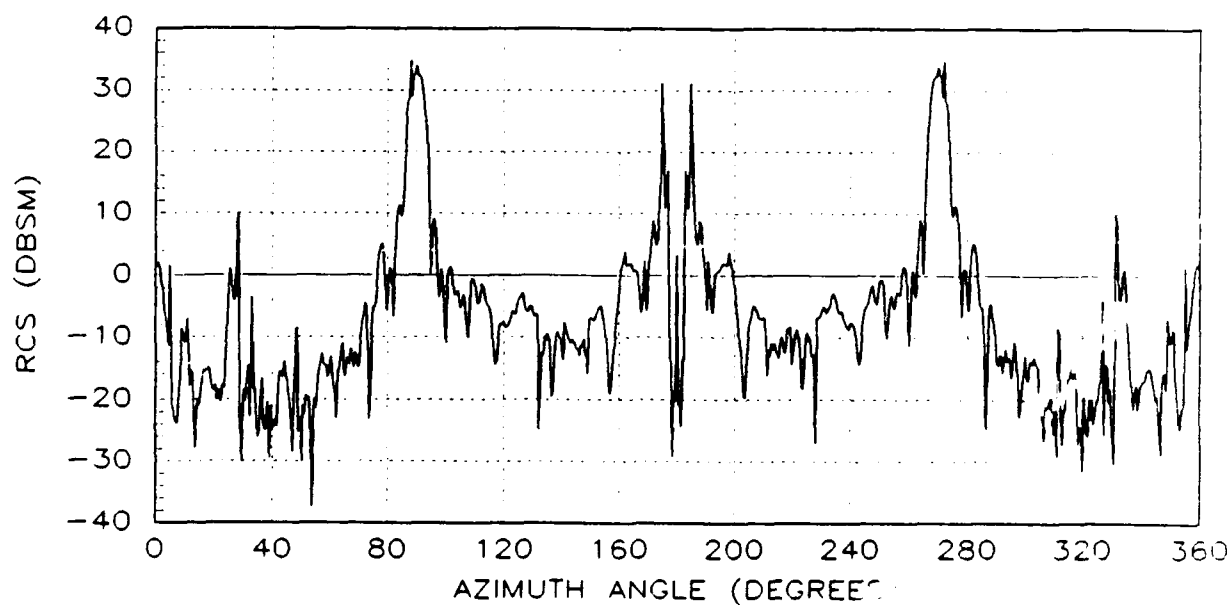
Figure B.14. Medianized, Averaged RCS Data Comparisons for the Non-deformed (solid line) versus Deformed (dashed line) C-5A Airframes for: (a) Vertical Polarization, and (b) Horizontal Polarization. NSM : -30 Degrees Elevation

## Appendix C

This appendix contains the raw computed RCS data for the T-38 airframe as modeled by the RCS analysis software RCSBSC2. The raw RCS for both the non-deformed and deformed airframes is presented for horizontal and vertical field polarizations and elevations ranging from -30 to 30 degrees. In all of the plots, the nose of the aircraft is located at 180 degrees and the illuminating frequency is 1 GHz.

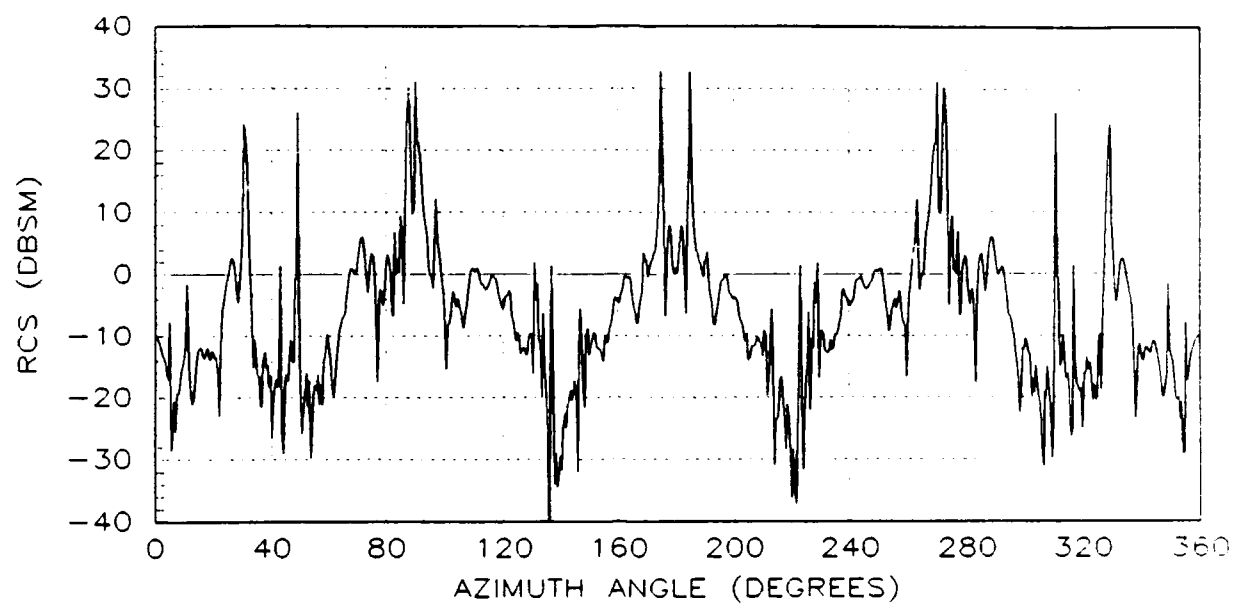


(a)

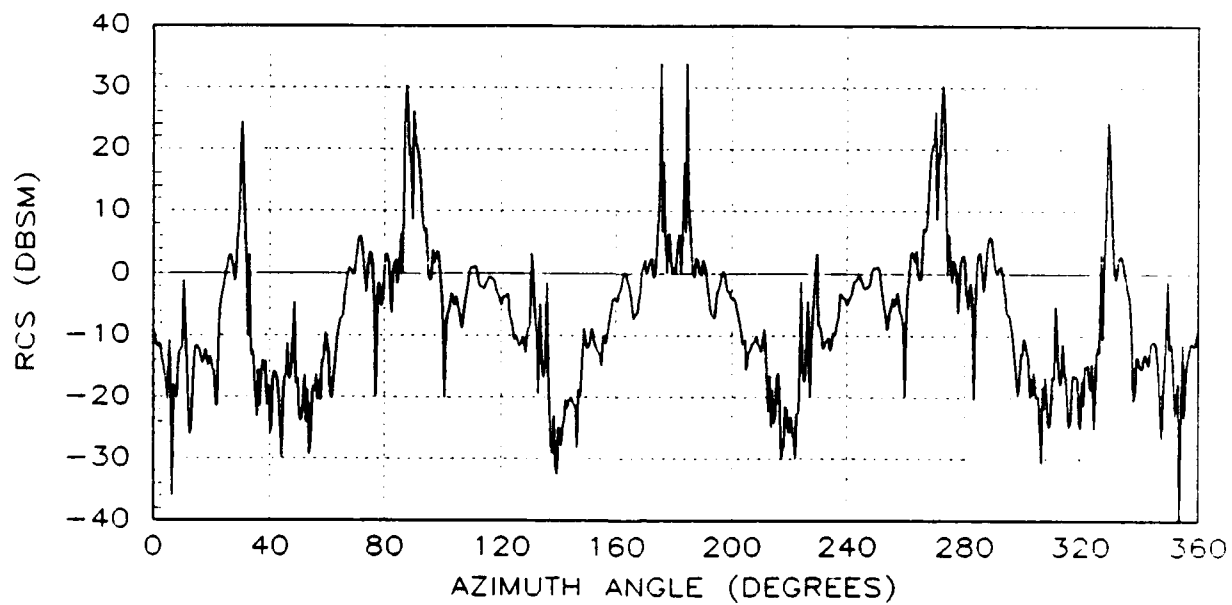


(b)

Figure C.1. Raw RCS of a T-38 Aircraft for: (a) Non-deformed Airframe, and (b) Deformed Airframe. 0 Degrees Elevation : Vertical Polarization



(a)



(b)

Figure C.2. Raw RCS of a T-38 Aircraft for: (a) Non - deformed Airframe, and (b) Deformed Airframe. 10 Degrees Elevation : Vertical Polarization

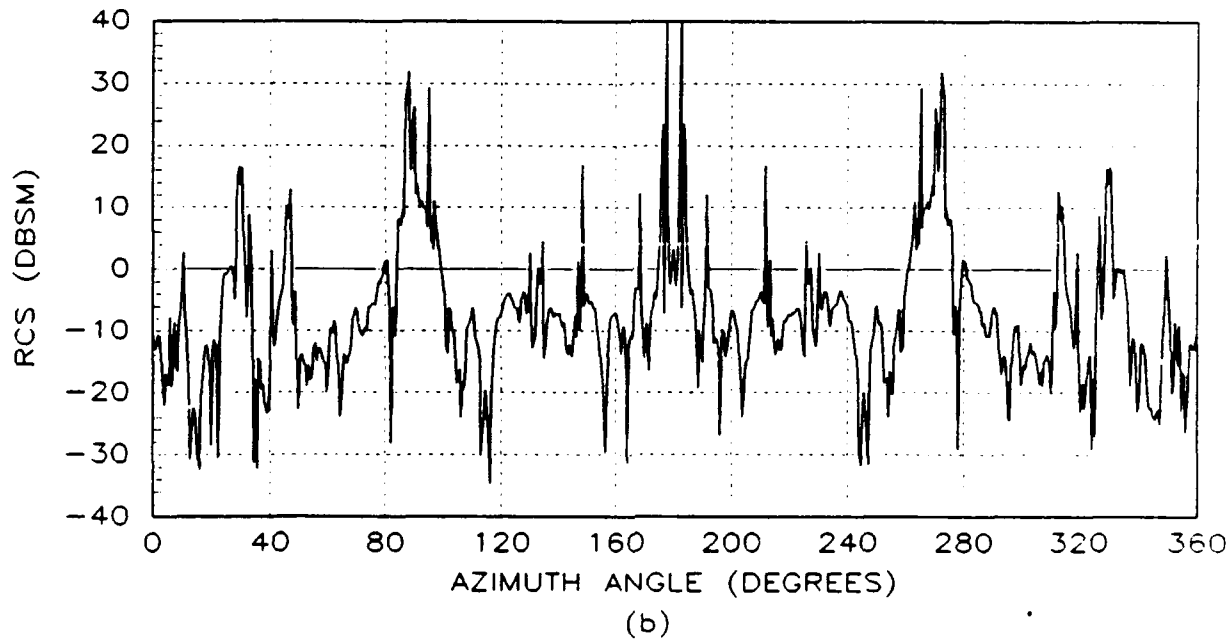
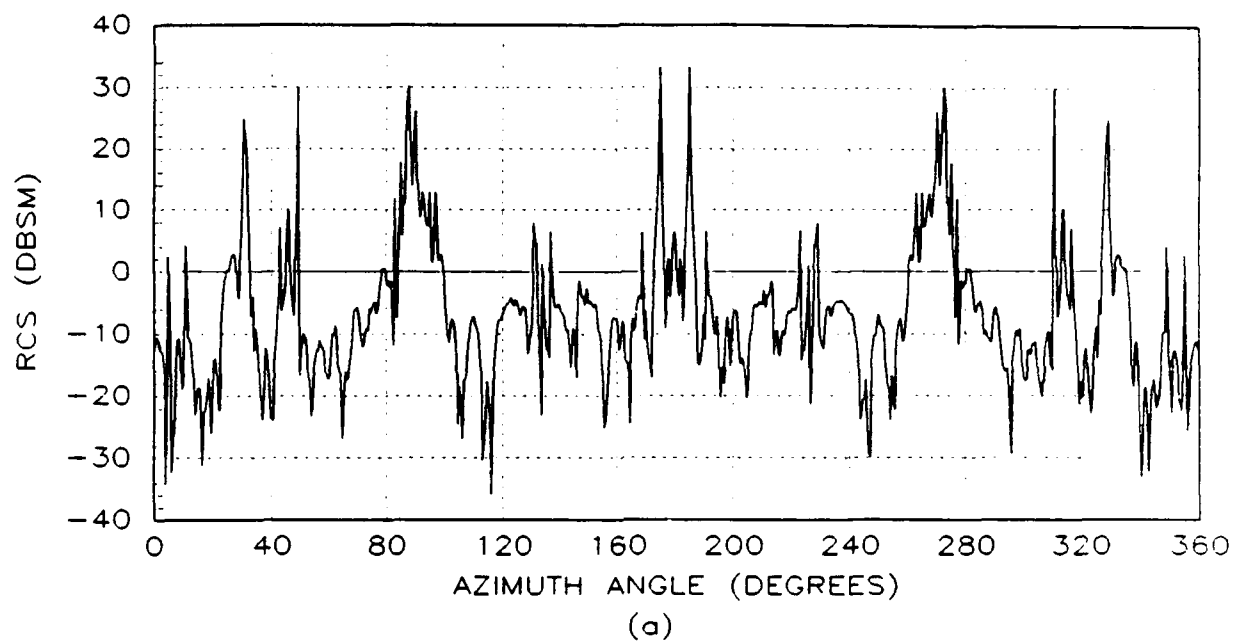


Figure C.3. Raw RCS of a T-38 Aircraft for: (a) Non-deformed Airframe, and (b) Deformed Airframe. 20 Degrees Elevation : Vertical Polarization

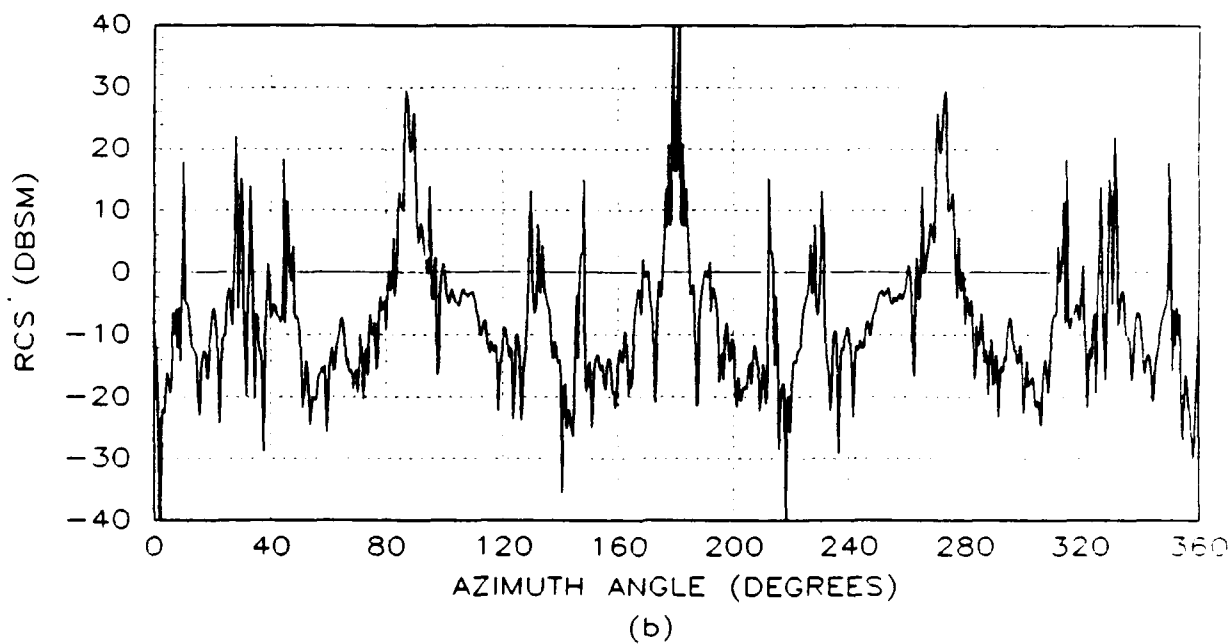
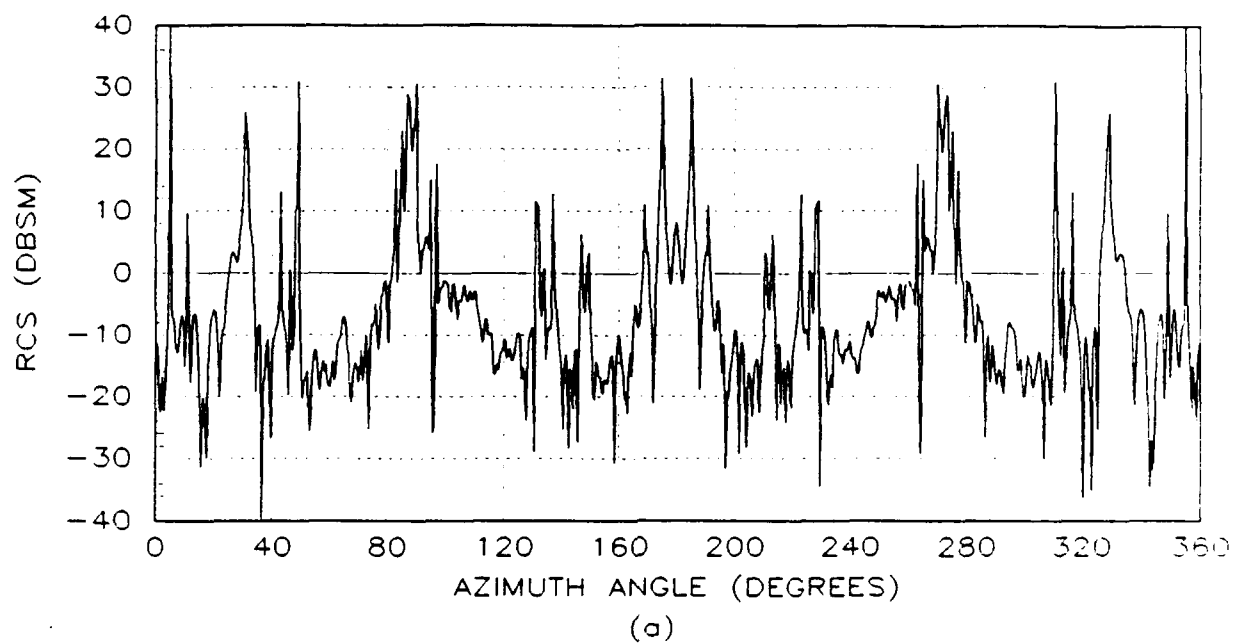
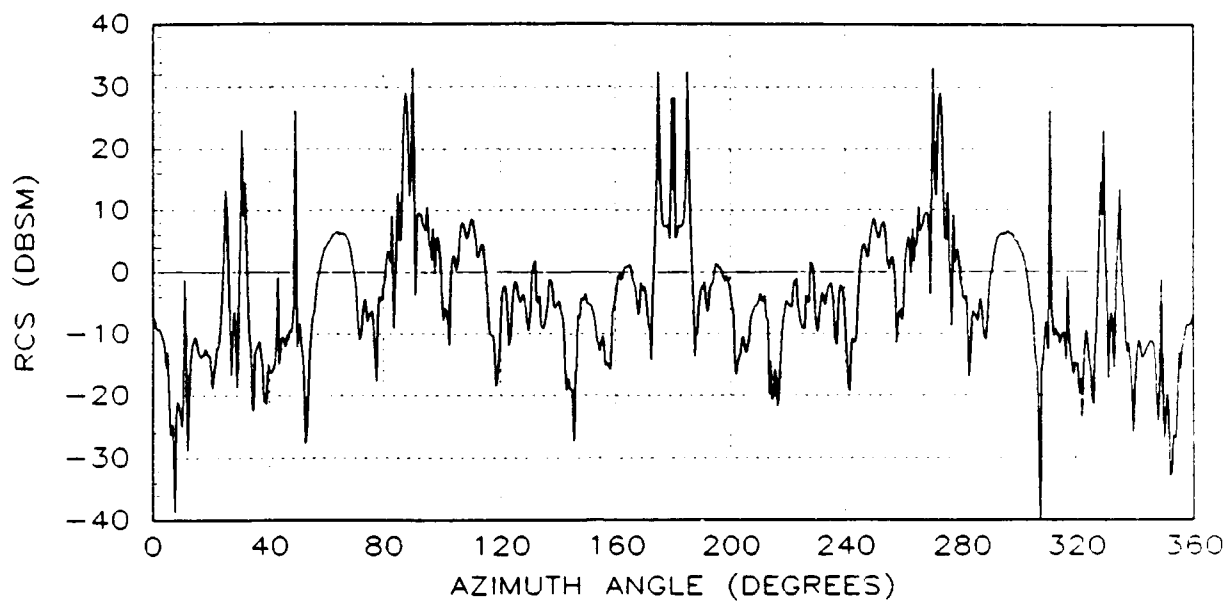
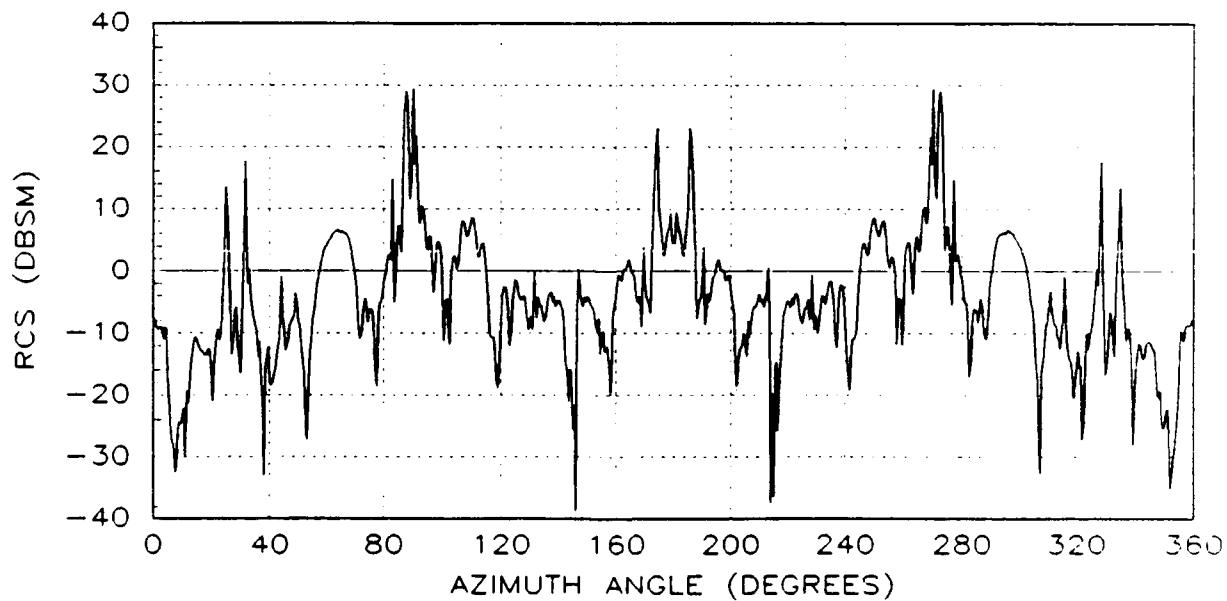


Figure C.4. Raw RCS of a T-38 Aircraft for: (a) Non-deformed Airframe, and (b) Deformed Airframe. 30 Degrees Elevation : Vertical Polarization





(a)



(b)

Figure C.5. Raw RCS of a T-38 Aircraft for: (a) Non-deformed Airframe, and (b) Deformed Airframe. -10 Degrees Elevation : Vertical Polarization

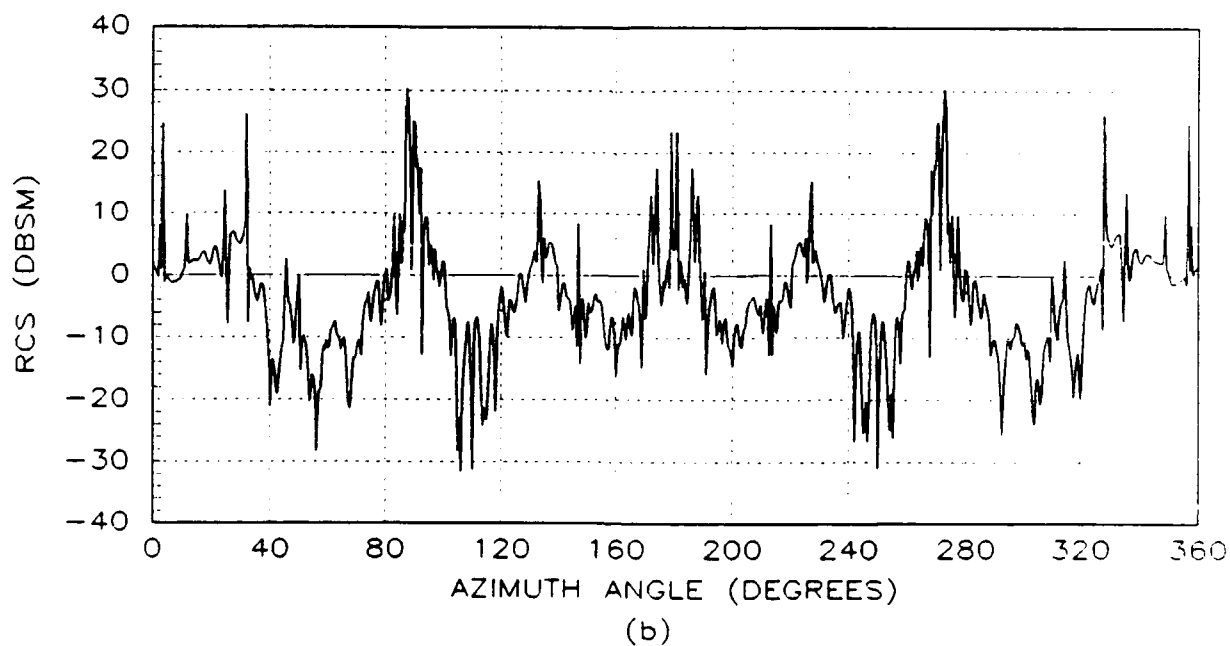
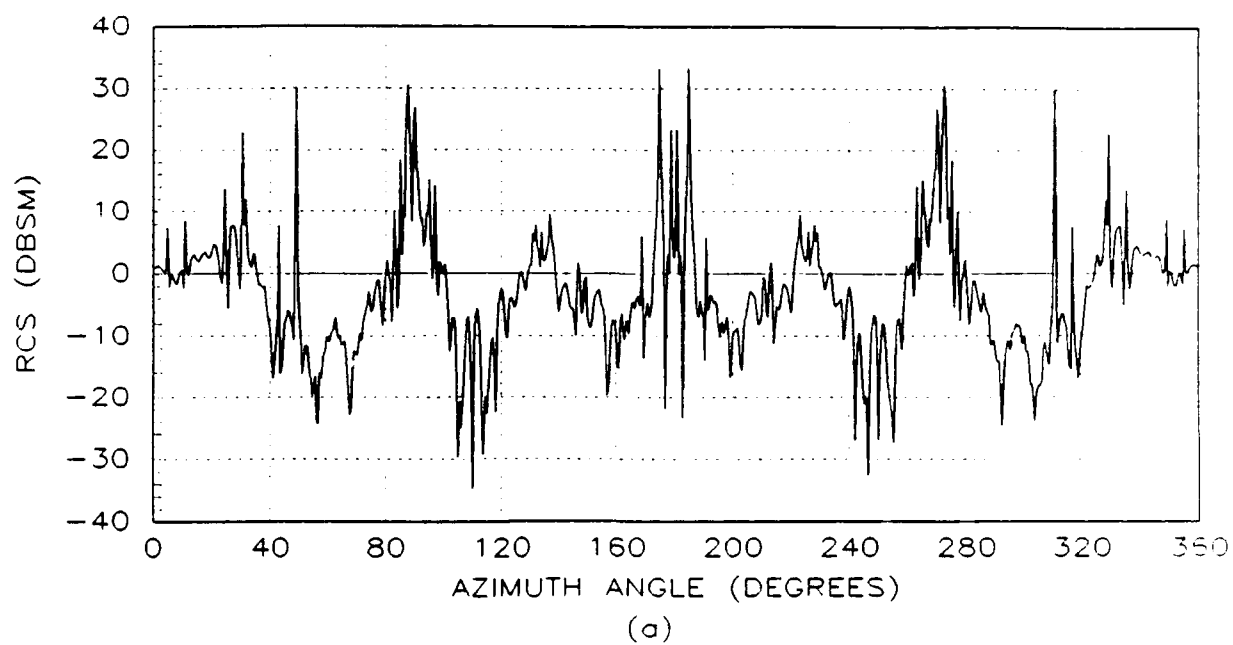


Figure C.6. Raw RCS of a T-38 Aircraft for: (a) Non-deformed Airframe, and (b) Deformed Airframe. -20 Degrees Elevation : Vertical Polarization

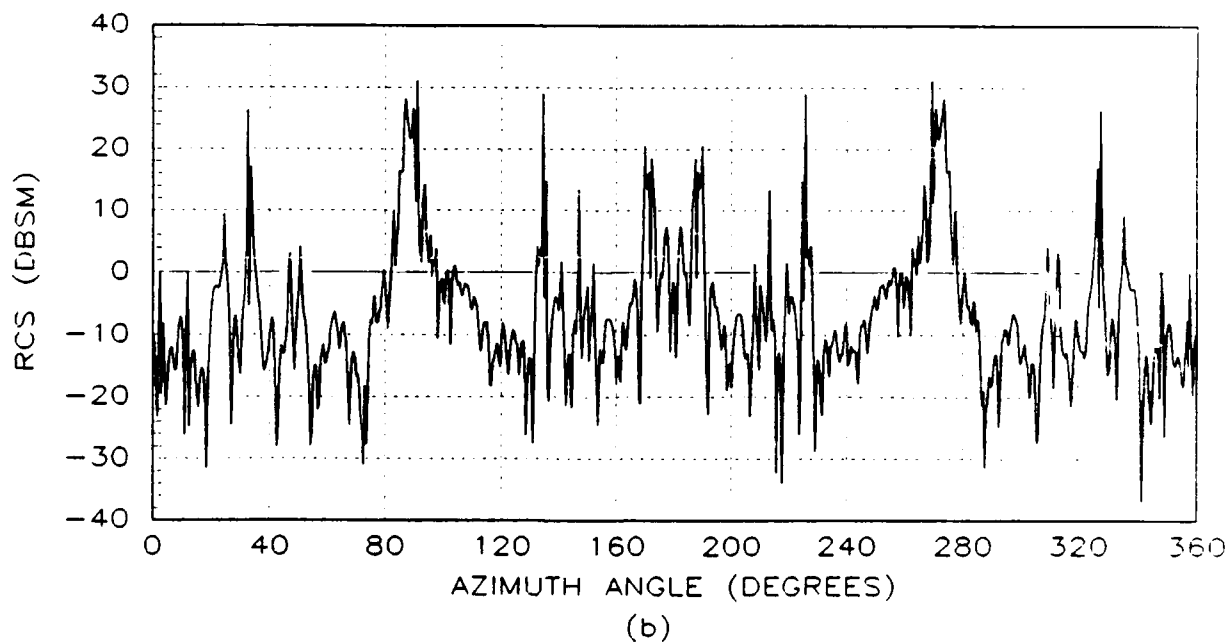
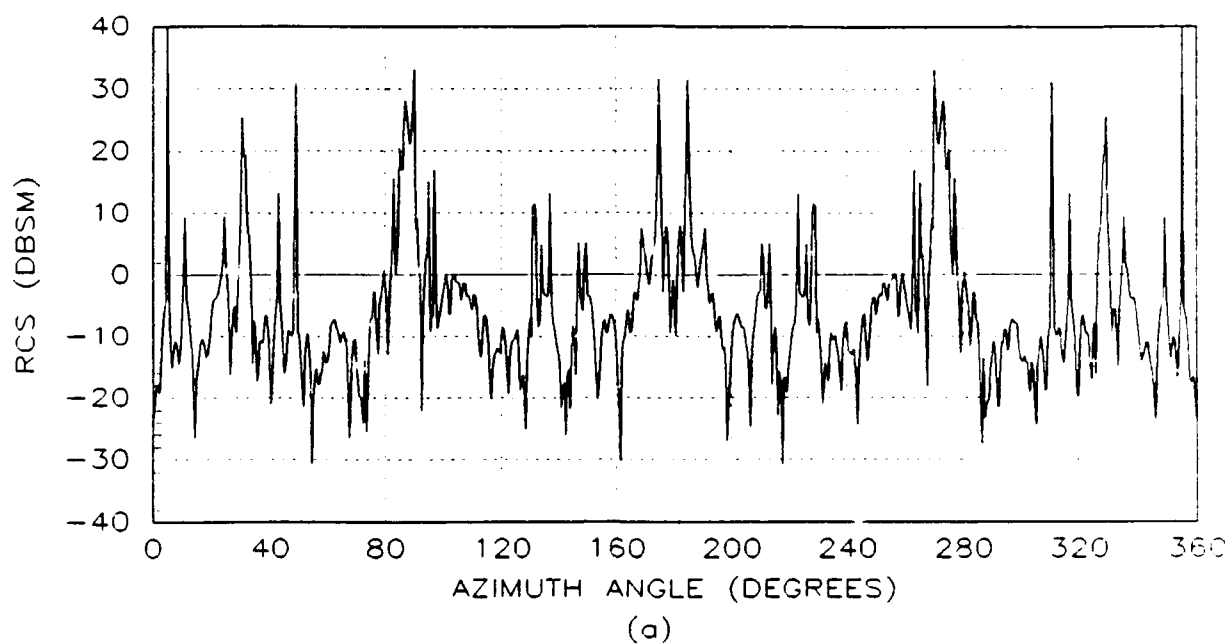


Figure C.7. Raw RCS of a T-38 Aircraft for: (a) Non-deformed Airframe, and (b) Deformed Airframe. -30 Degrees Elevation : Vertical Polarization

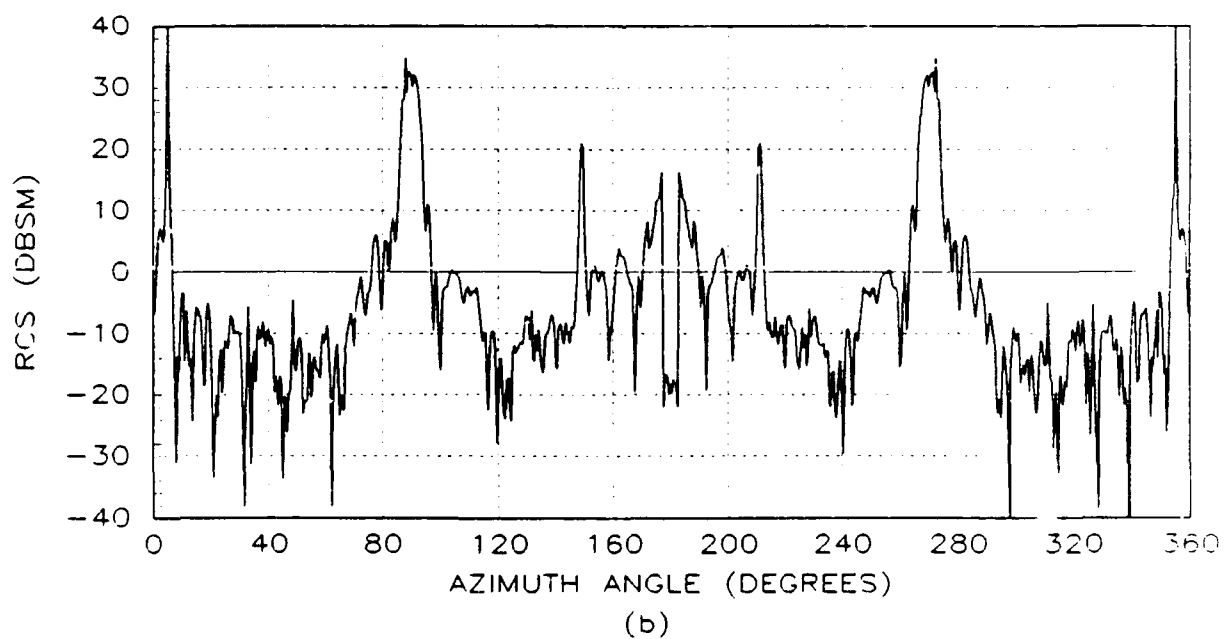
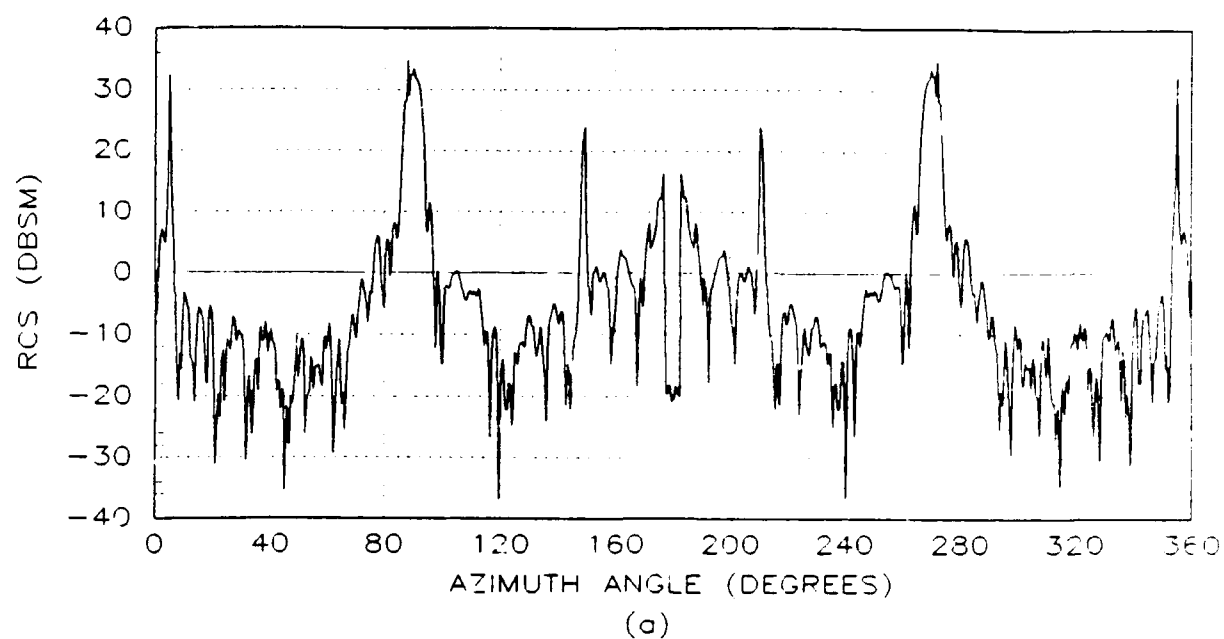
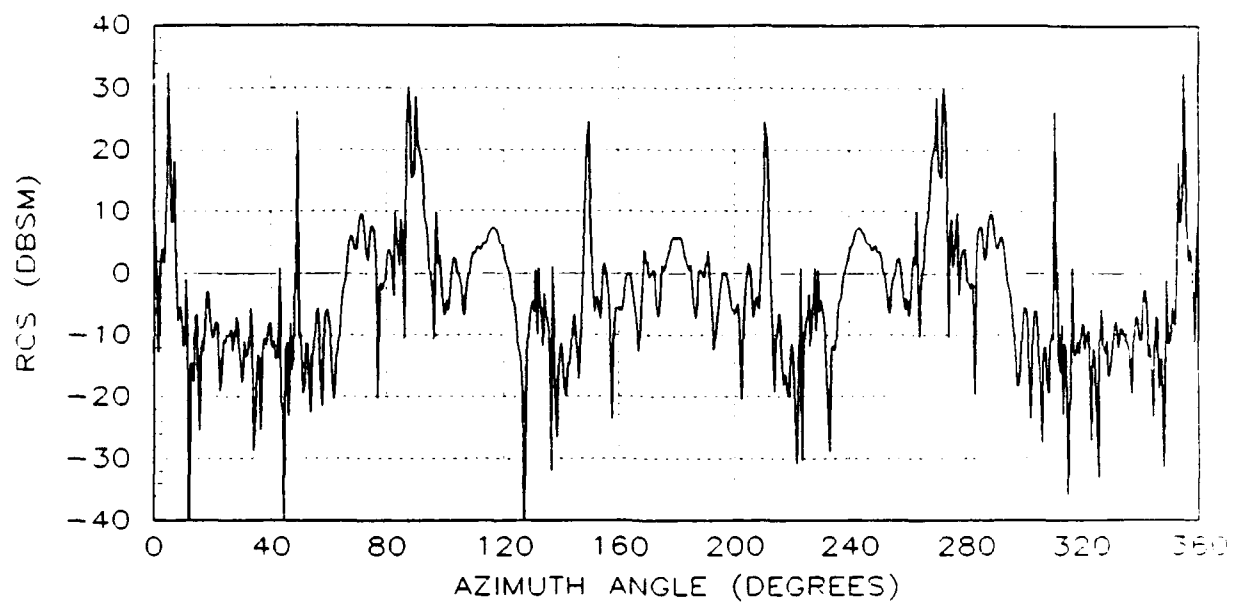
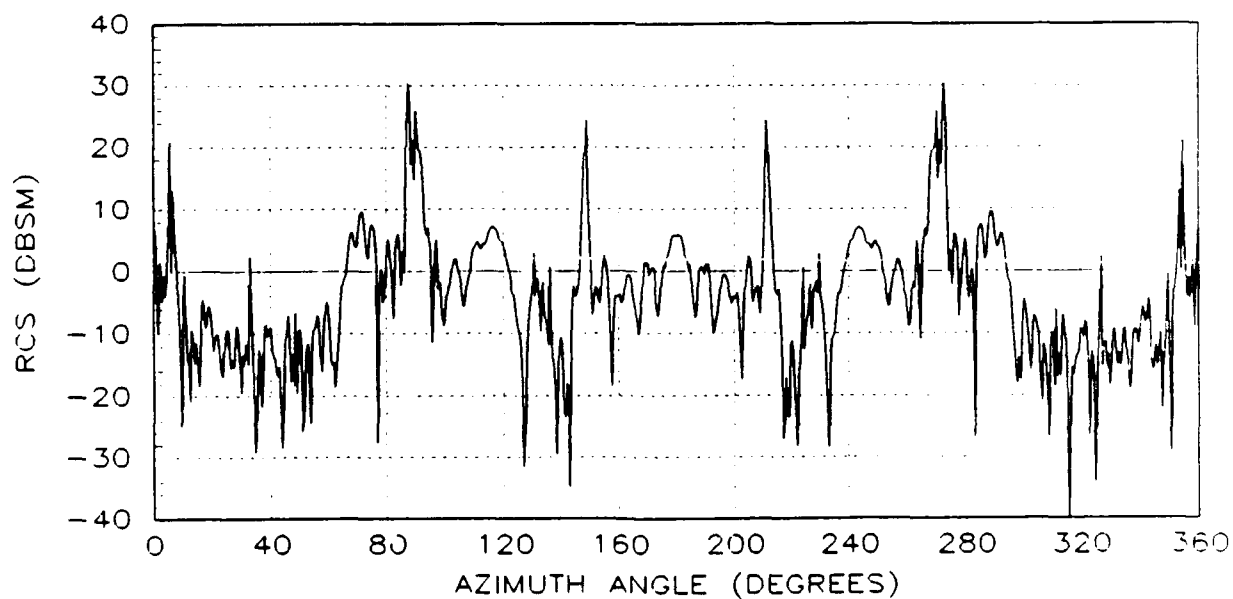


Figure C.8. Raw RCS of a T-38 Aircraft for: (a) Non-deformed Airframe, and (b) Deformed Airframe. 0 Degrees Elevation : Horizontal Polarization



(a)



(b)

Figure C.9. Raw RCS of a T-38 Aircraft for: (a) Non-deformed Airframe, and (b) Deformed Airframe. 10 Degrees Elevation : Horizontal Polarization

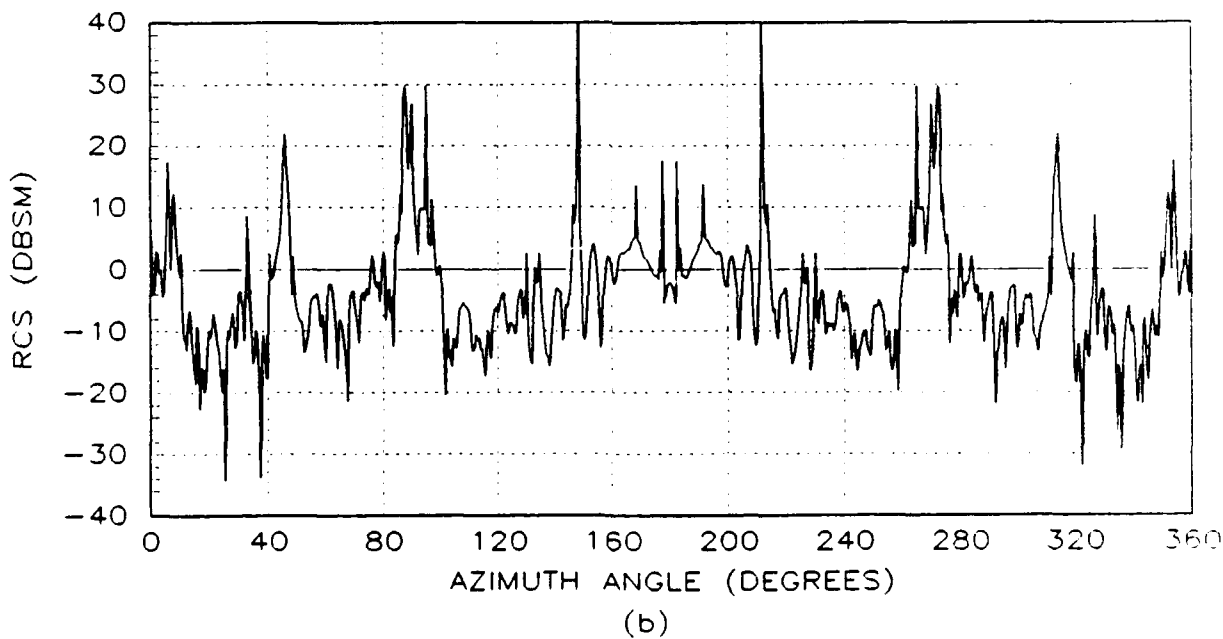
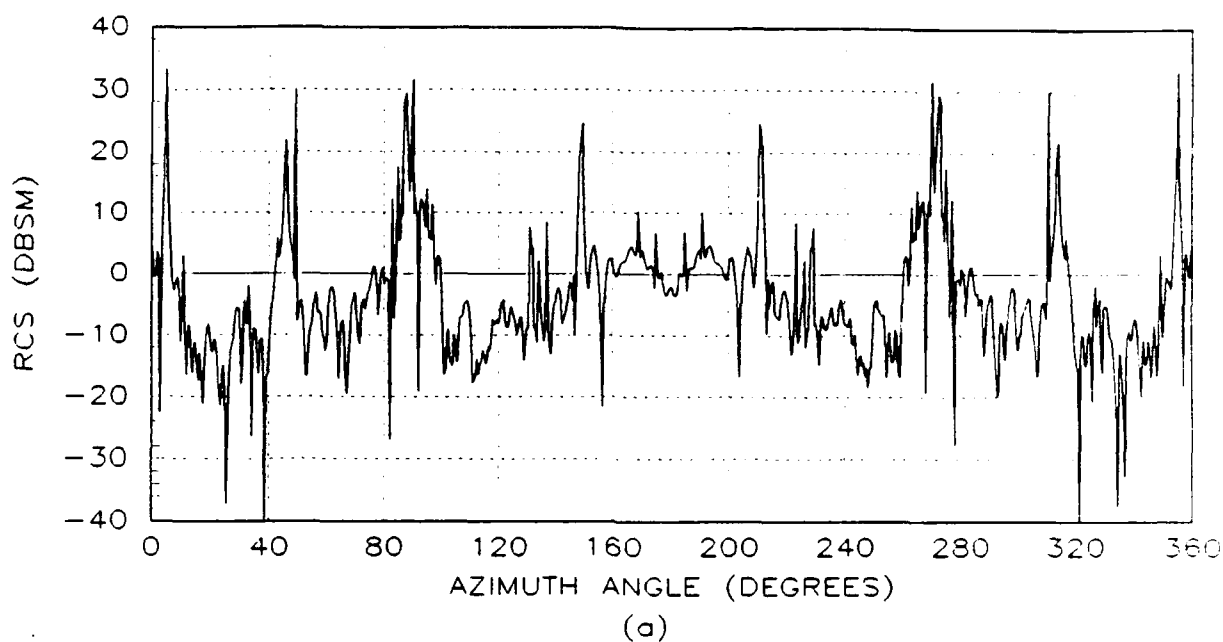


Figure C.10. Raw RCS of a T-38 Aircraft for: (a) Non-deformed Airframe, and (b) Deformed Airframe. 20 Degrees Elevation : Horizontal Polarization

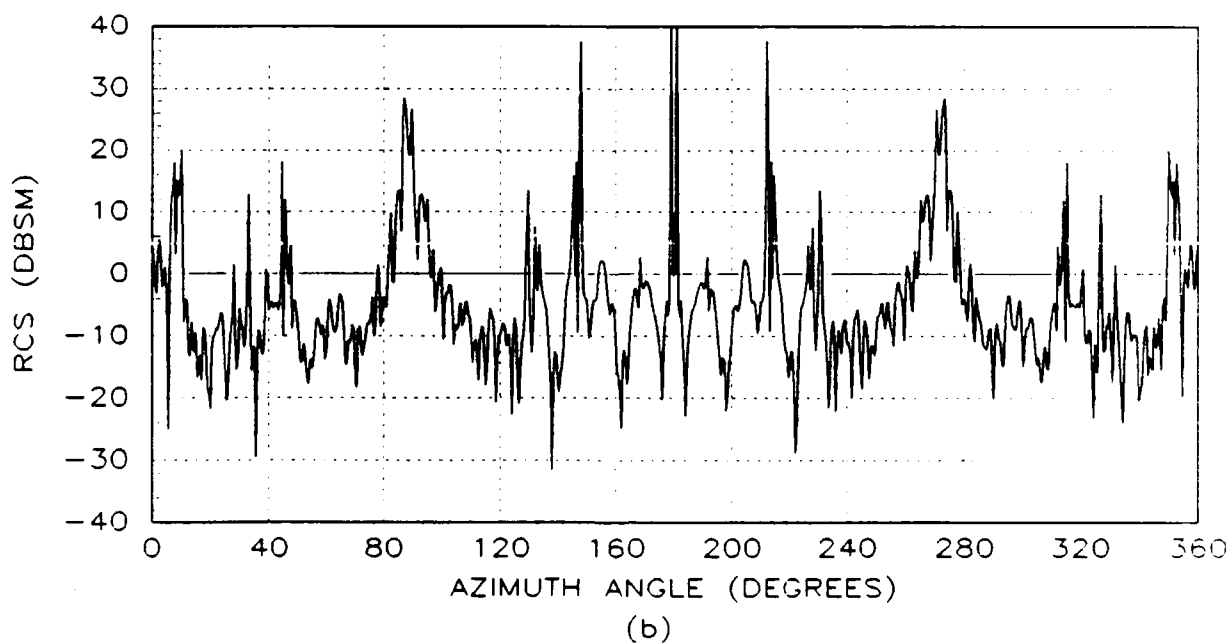
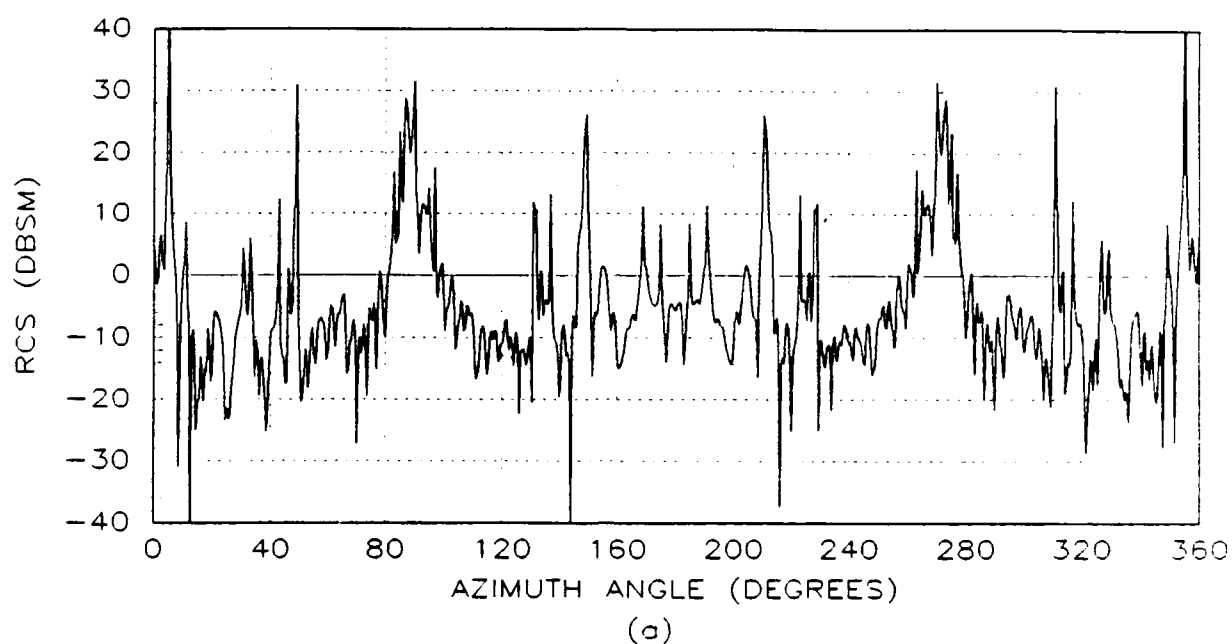


Figure C.11. Raw RCS of a T-38 Aircraft for: (a) Non-deformed Airframe, and (b) Deformed Airframe. 30 Degrees Elevation : Horizontal Polarization

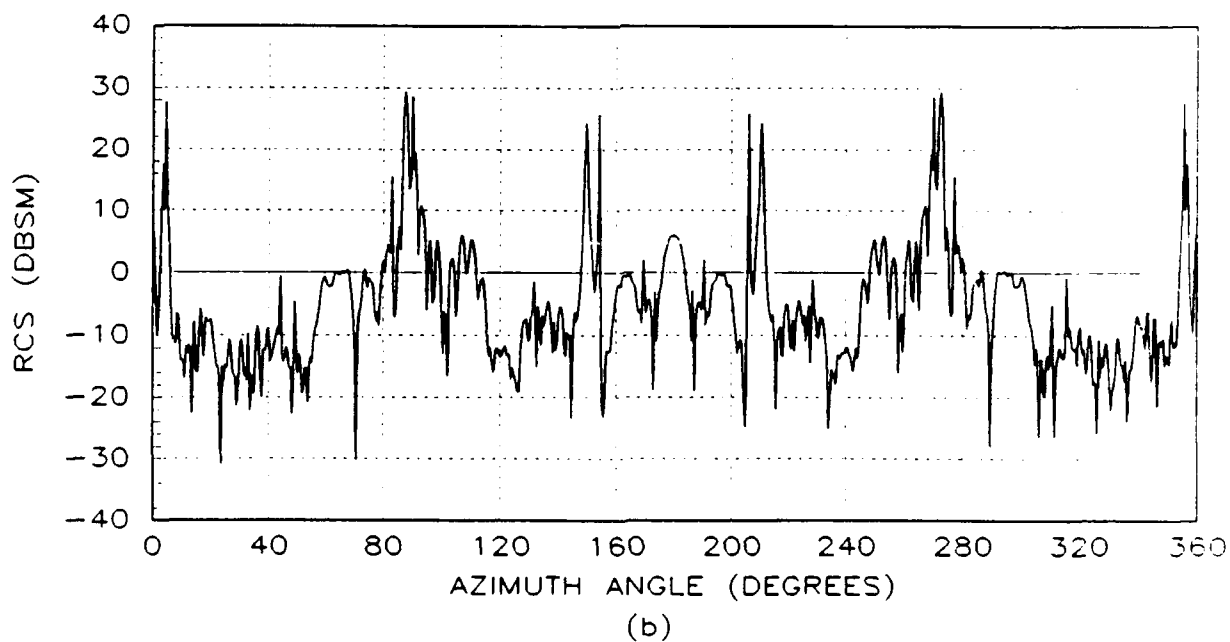
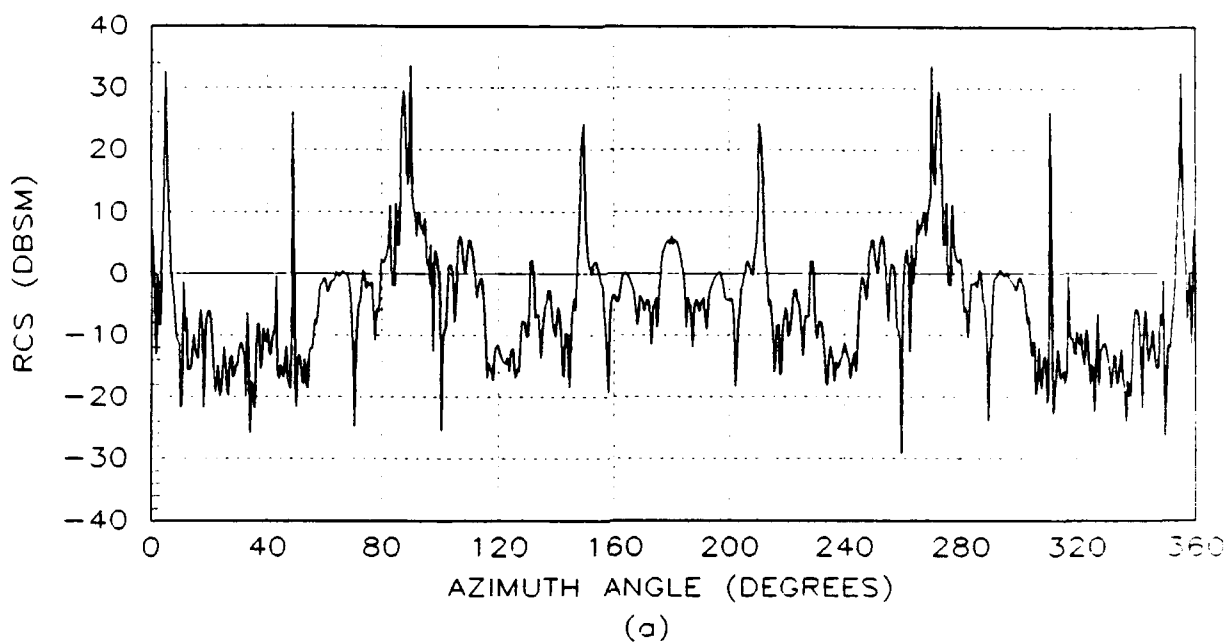
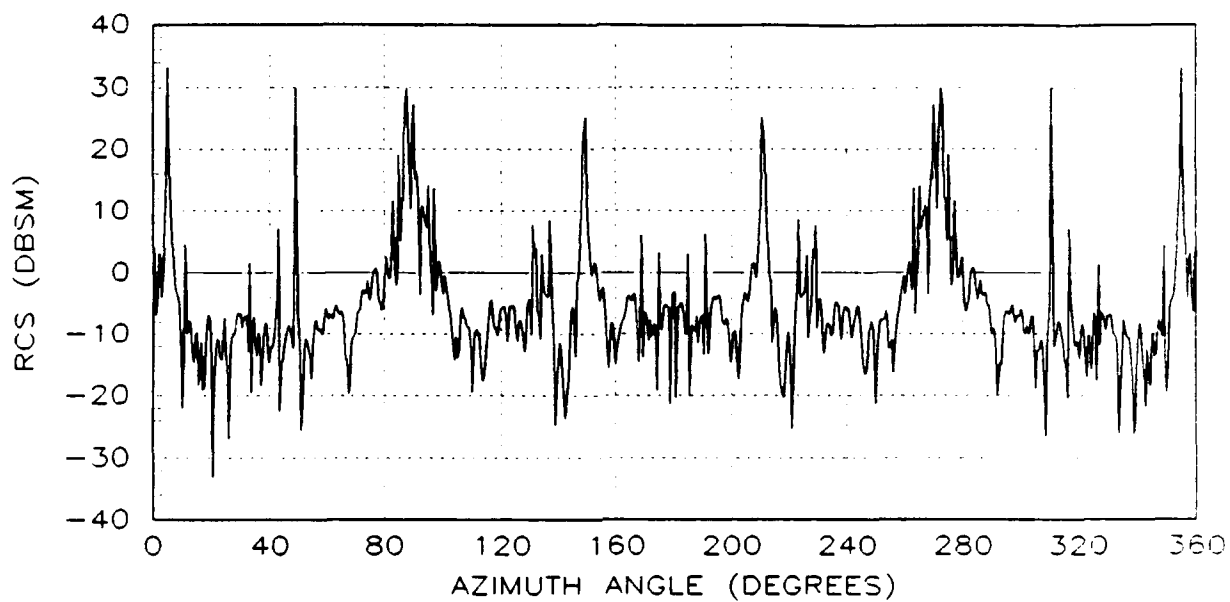
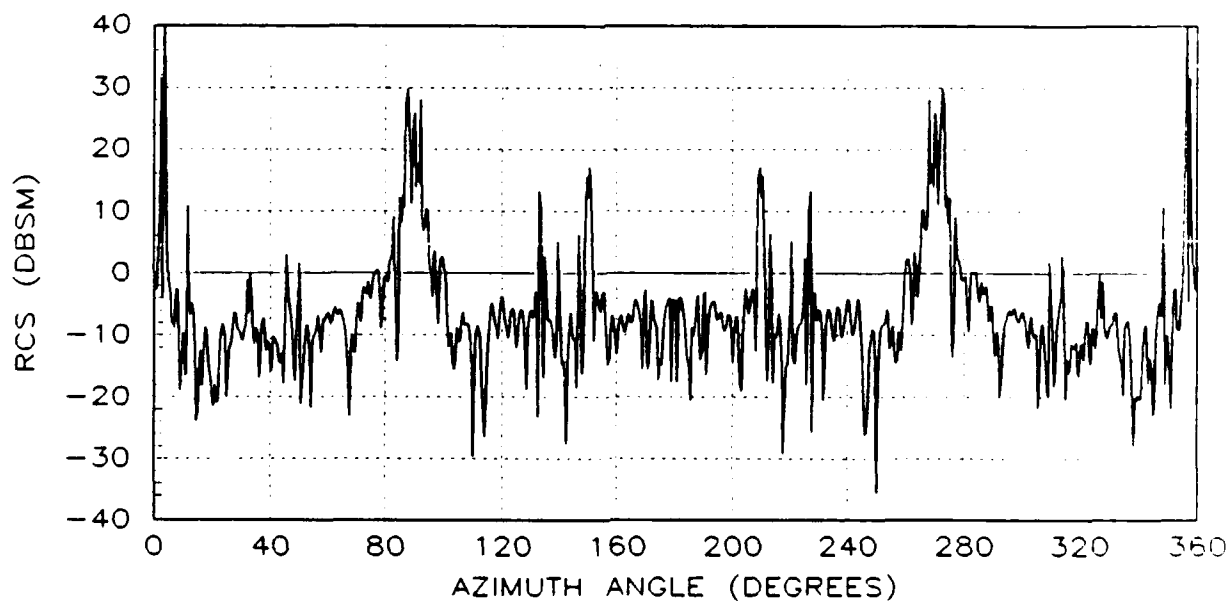


Figure C.12. Raw RCS of a T-38 Aircraft for: (a) Non-deformed Airframe, and (b) Deformed Airframe. -10 Degrees Elevation : Horizontal Polarization





(a)



(b)

Figure C.13. Raw RCS of a T-38 Aircraft for: (a) Non-deformed Airframe, and (b) Deformed Airframe. -20 Degrees Elevation : Horizontal Polarization

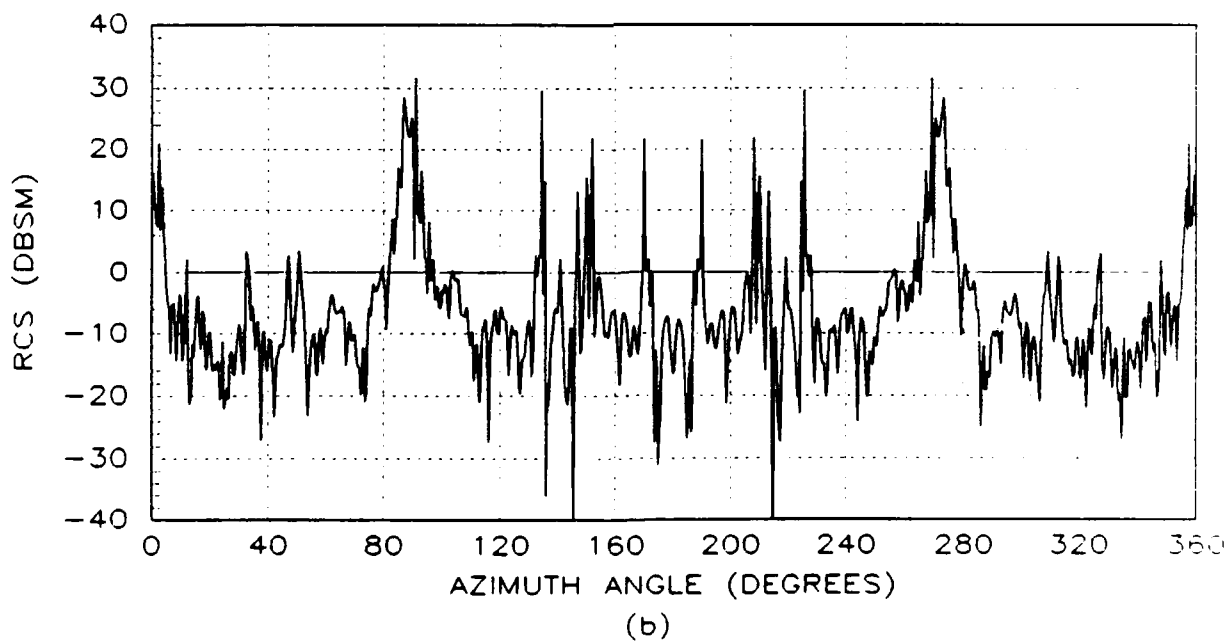
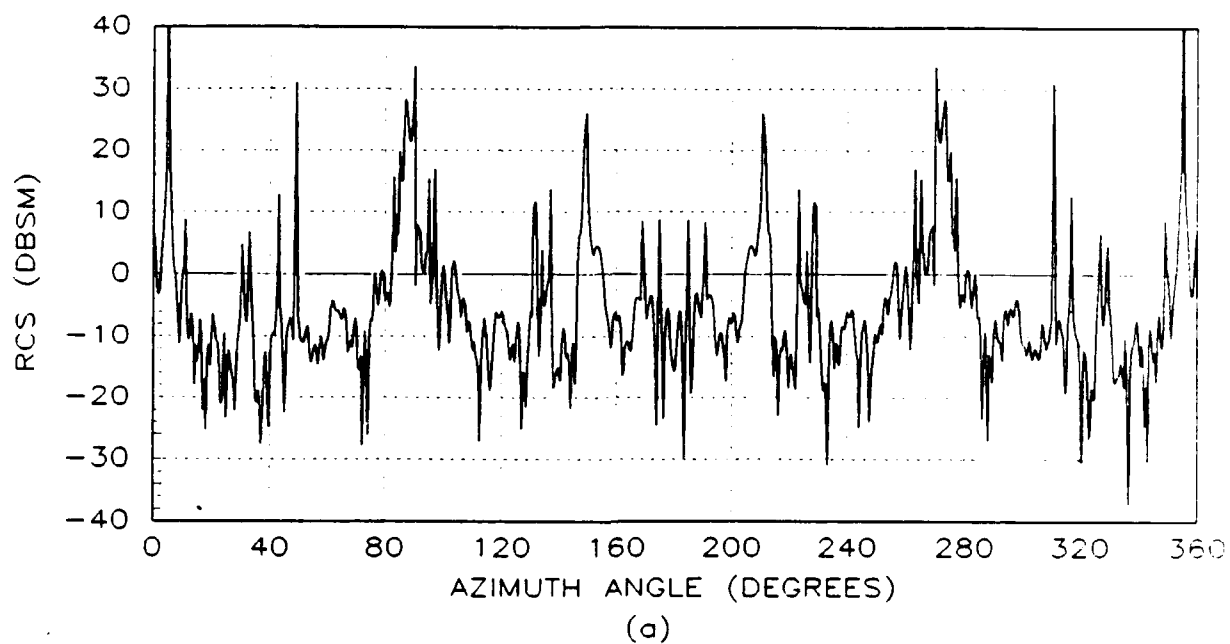


Figure C.14. Raw RCS of a T-38 Aircraft for: (a) Non-deformed Airframe, and (b) Deformed Airframe. -30 Degrees Elevation : Horizontal Polarization

## Appendix D

This appendix contains the raw RCS data for the 1/10th scale model of the C-5A Airframe as modeled by the RCS analysis software RCSBSC2. The computed raw RCS for the non-deformed airframe as well as the RCS for the airframe deformed by both a Positive Symmetric Maneuver (PSM) and Negative Symmetric Maneuver (NSM) is presented for horizontal and vertical field polarizations and elevations ranging from -30 to 30 degrees. In all of the plots, the nose of the aircraft is located at 180 degrees and the illuminating frequency is 10 GHz.

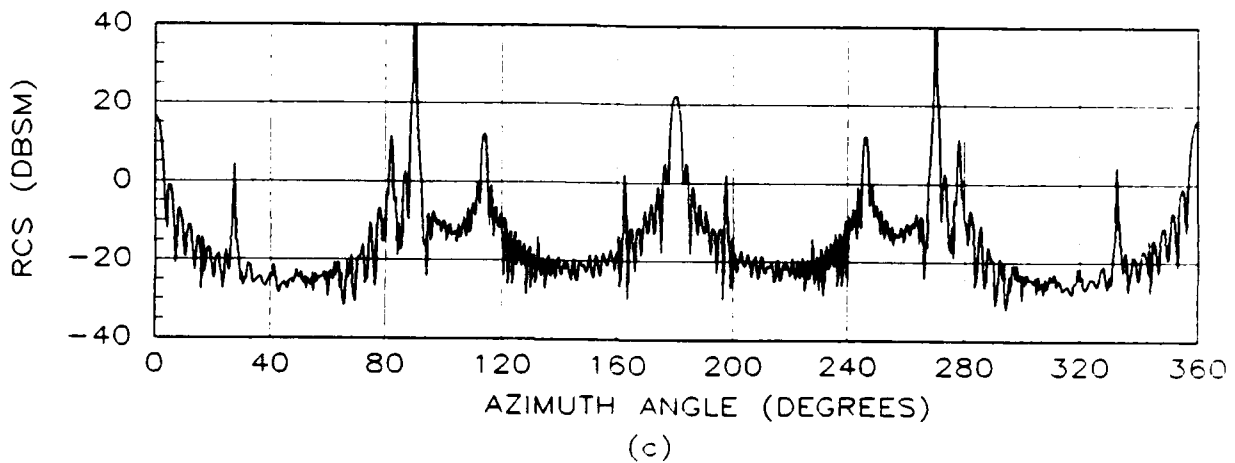
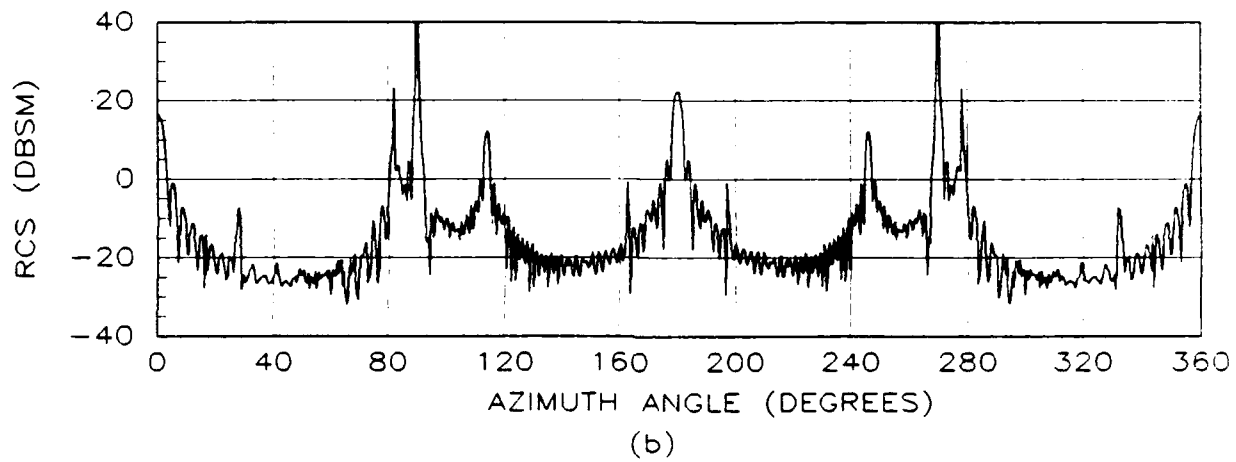
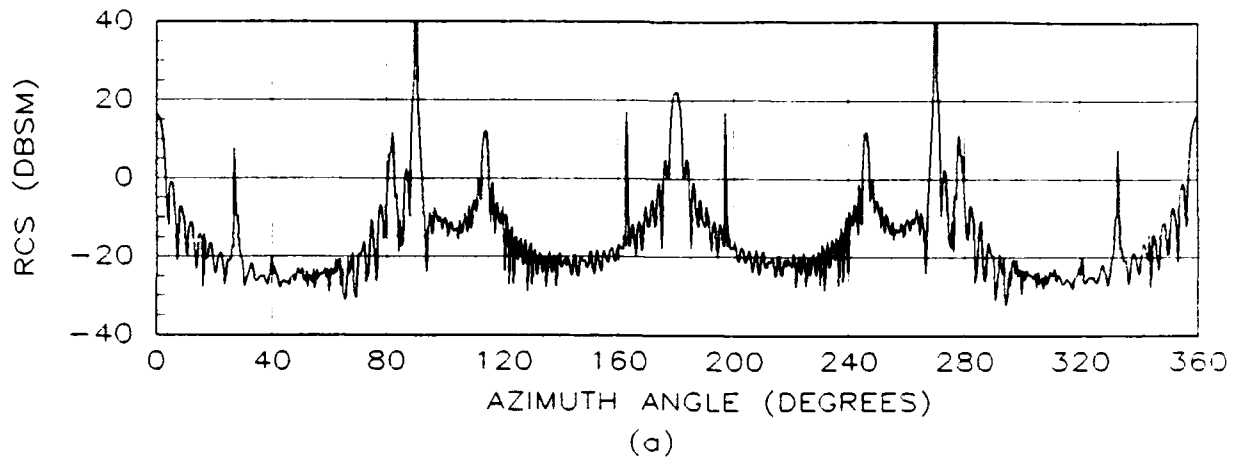
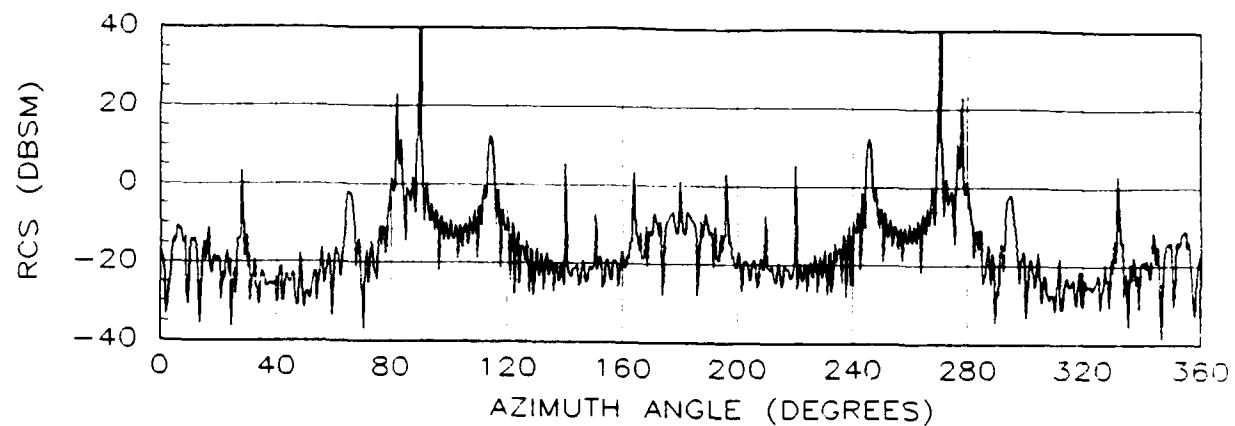
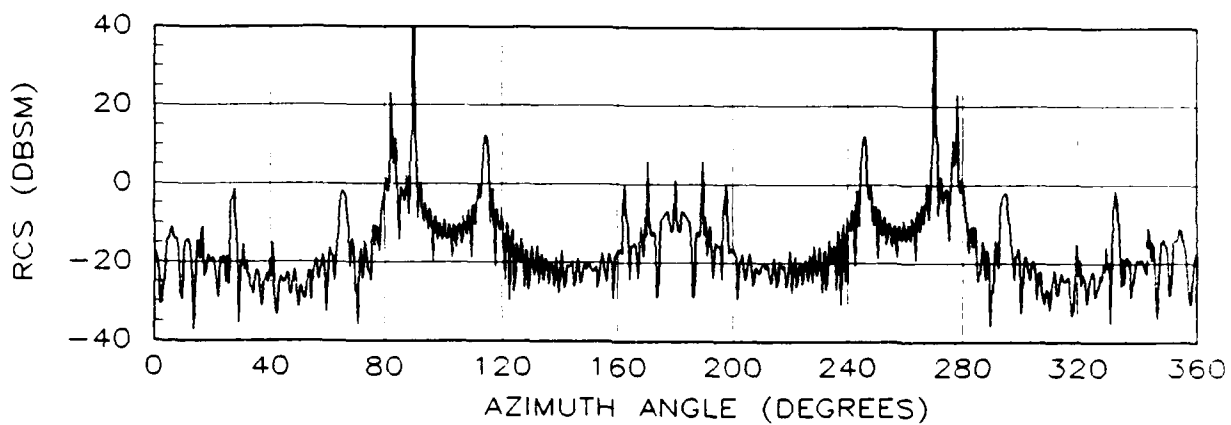


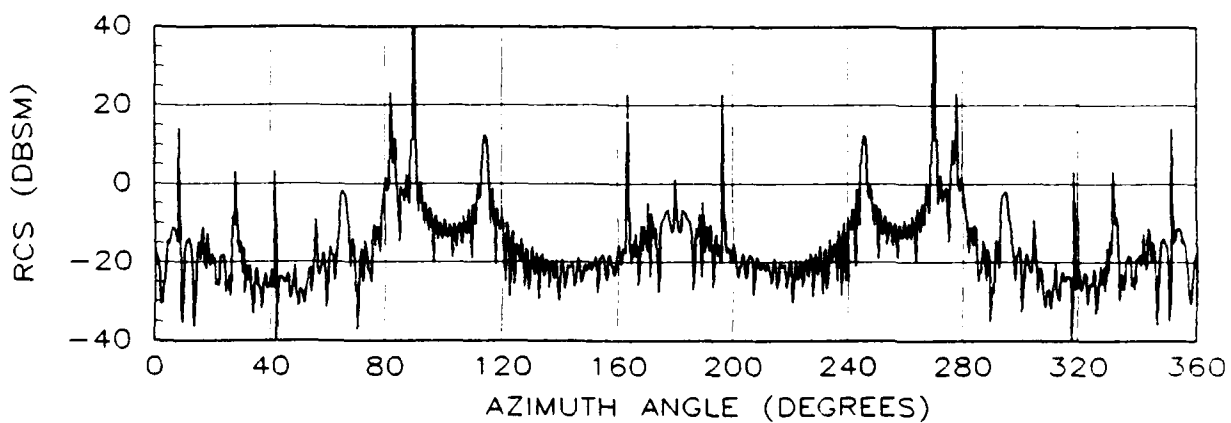
Figure D.1. Raw RCS of a C-5A Aircraft for: (a) Non-deformed Airframe, (b) PSM deformation, and (c) NSM deformation. 0 Degrees Elevation : Vertical Polarization



(a)



(b)



(c)

Figure D.2. Raw RCS of a C-5A Aircraft for: (a) Non-deformed Airframe, (b) PSM deformation, and (c) NSM deformation. 10 Degrees Elevation : Vertical Polarization

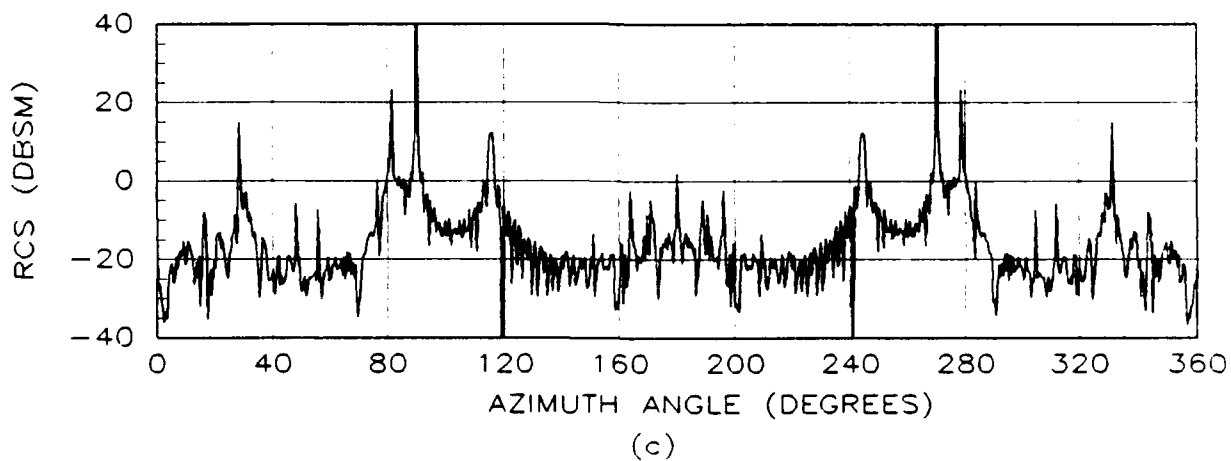
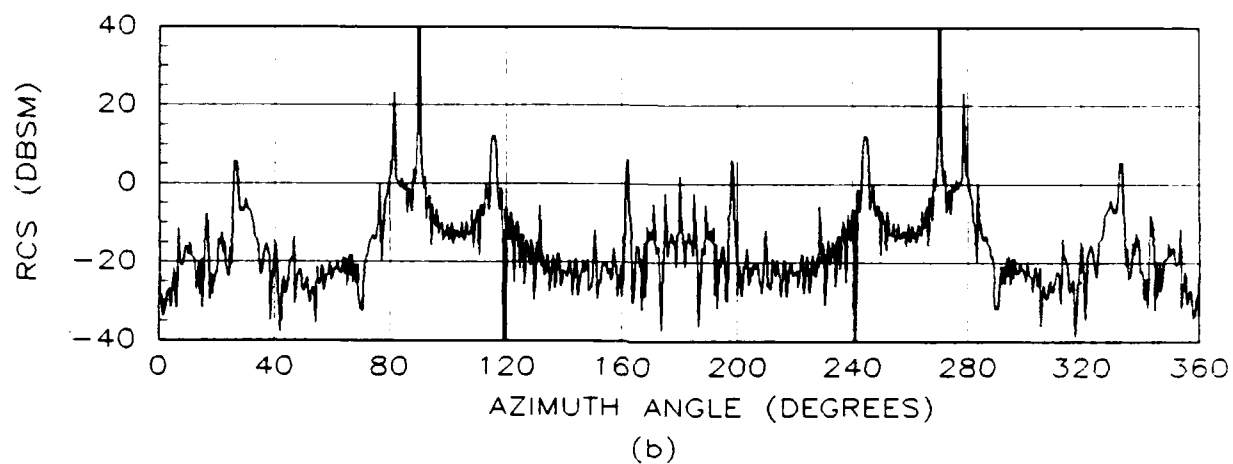
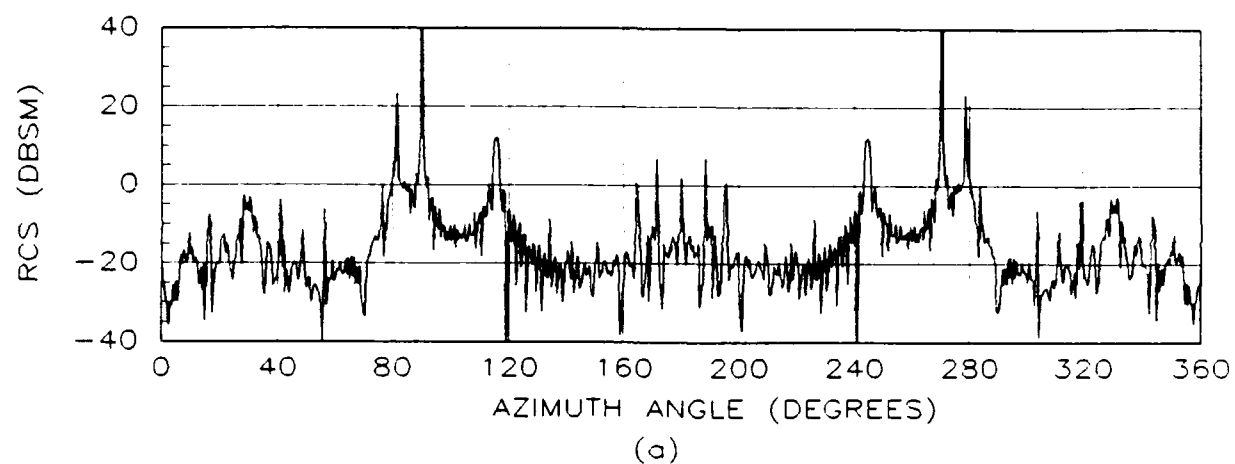
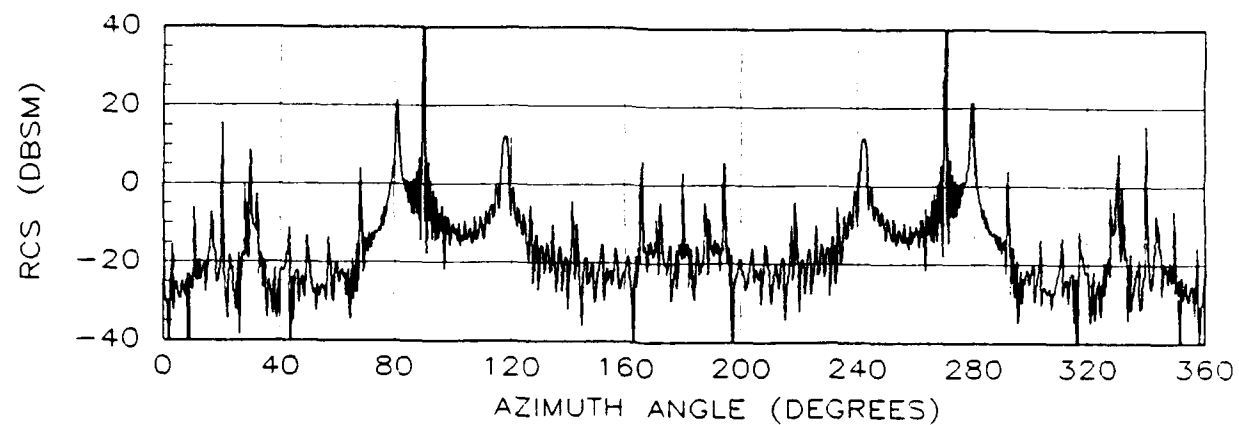
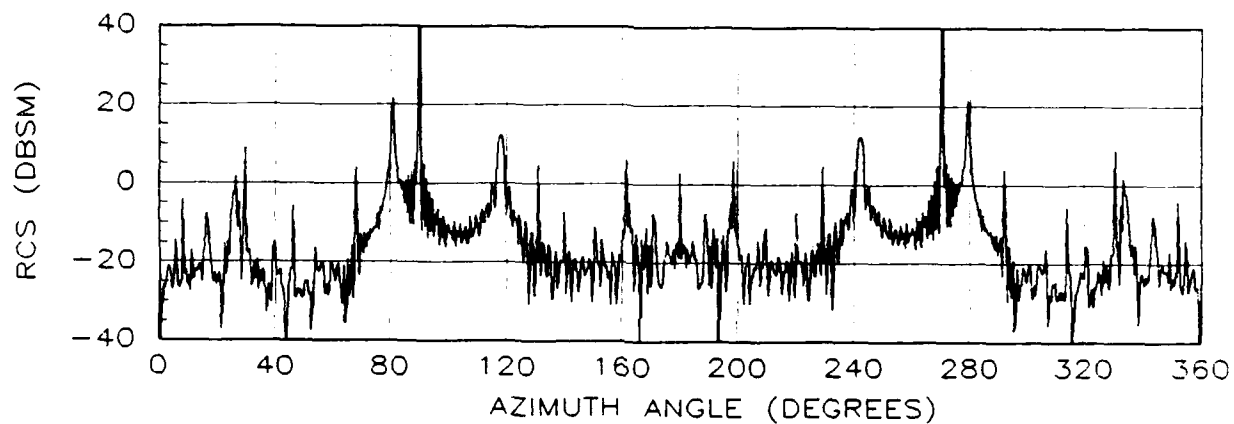


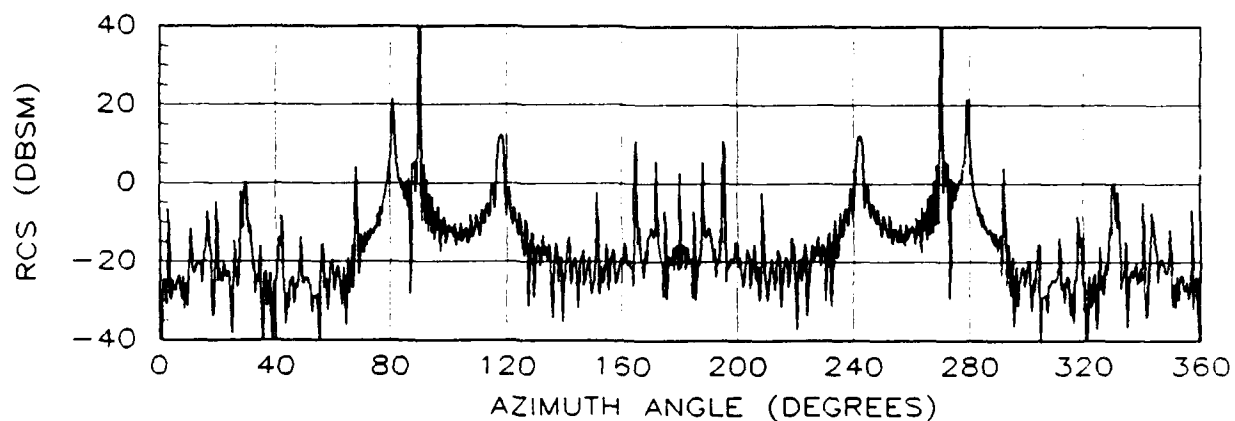
Figure D.3. Raw RCS of a C-5A Aircraft for: (a) Non-deformed Airframe, (b) PSM deformation, and (c) NSM deformation. 20 Degrees Elevation : Vertical Polarization



(a)

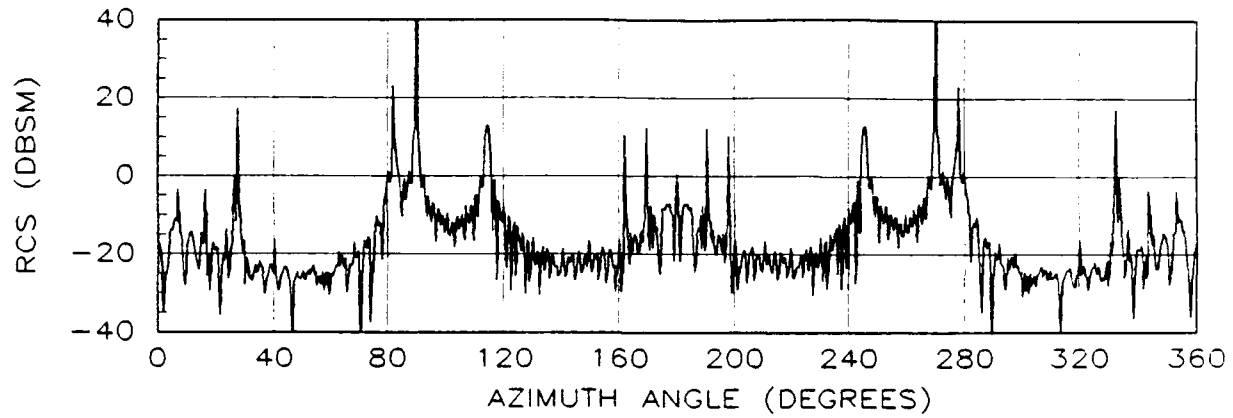


(b)

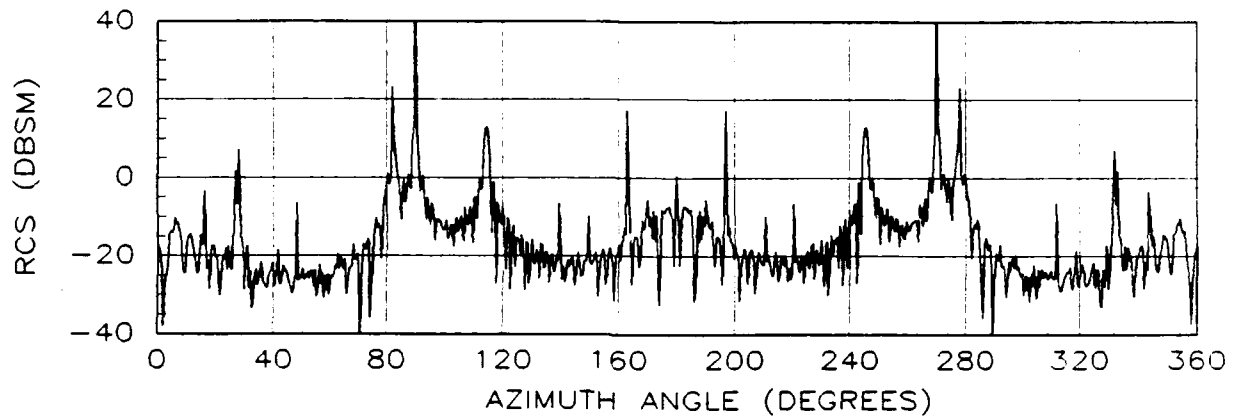


(c)

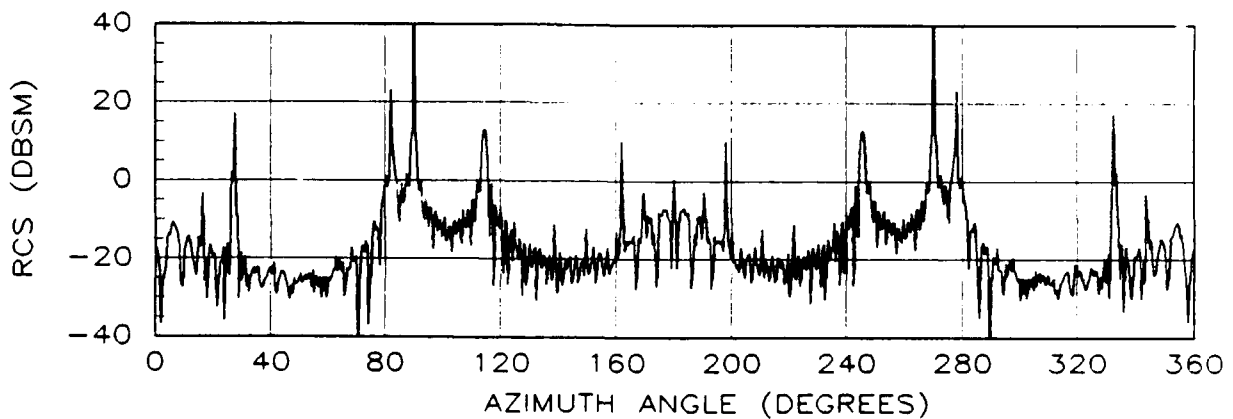
Figure D.4. Raw RCS of a C-5A Aircraft for: (a) Non-deformed Airframe, (b) PSM deformation, and (c) NSM deformation. 30 Degrees Elevation : Vertical Polarization



(a)



(b)



(c)

Figure D.5. Raw RCS of a C-5A Aircraft for: (a) Non-deformed Airframe, (b) PSM deformation, and (c) NSM deformation. -10 Degrees Elevation : Vertical Polarization



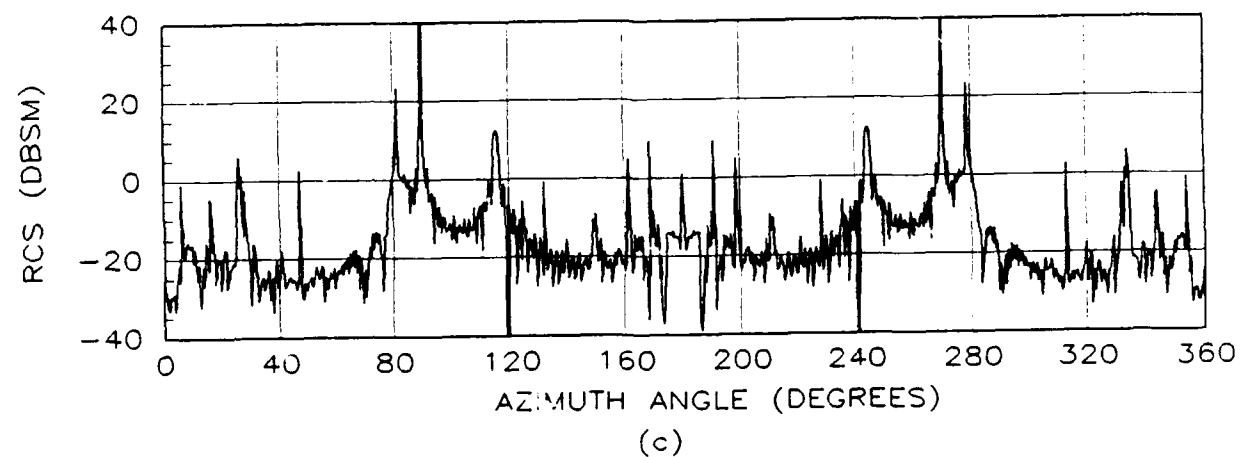
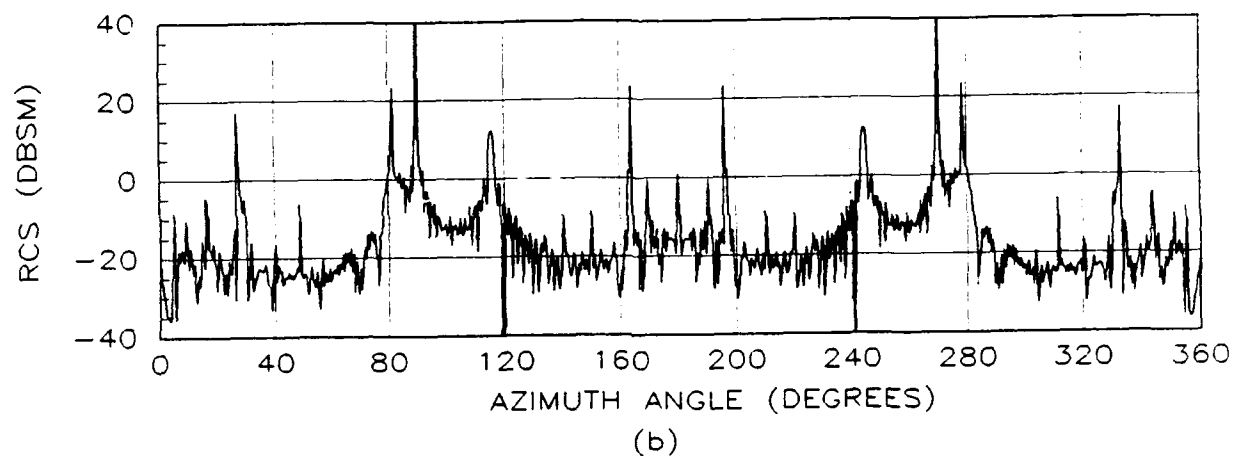
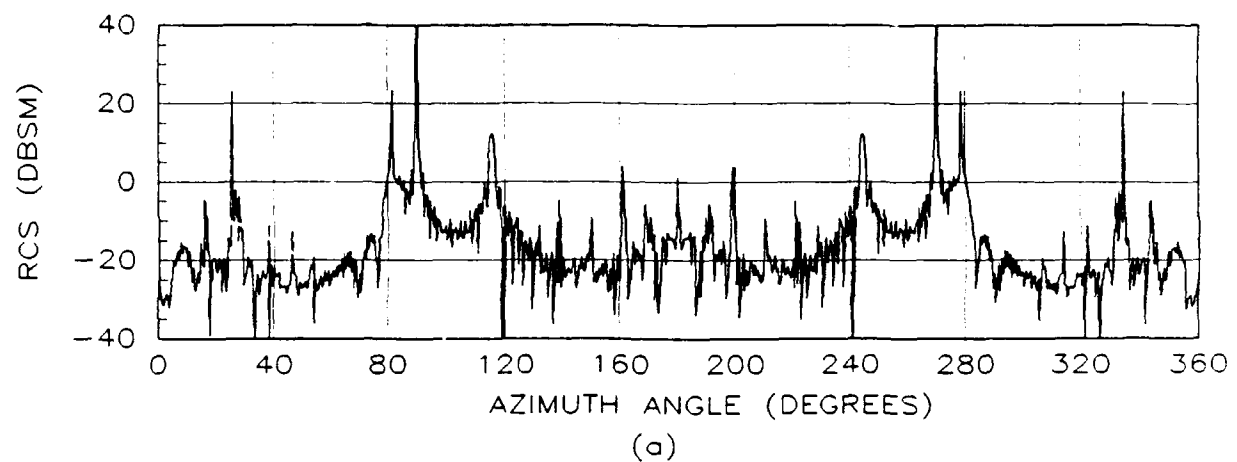


Figure D.6. Raw RCS of a C-5A Aircraft for: (a) Non-deformed Airframe, (b) PSM deformation, and (c) NSM deformation. -20 Degrees Elevation : Vertical Polarization

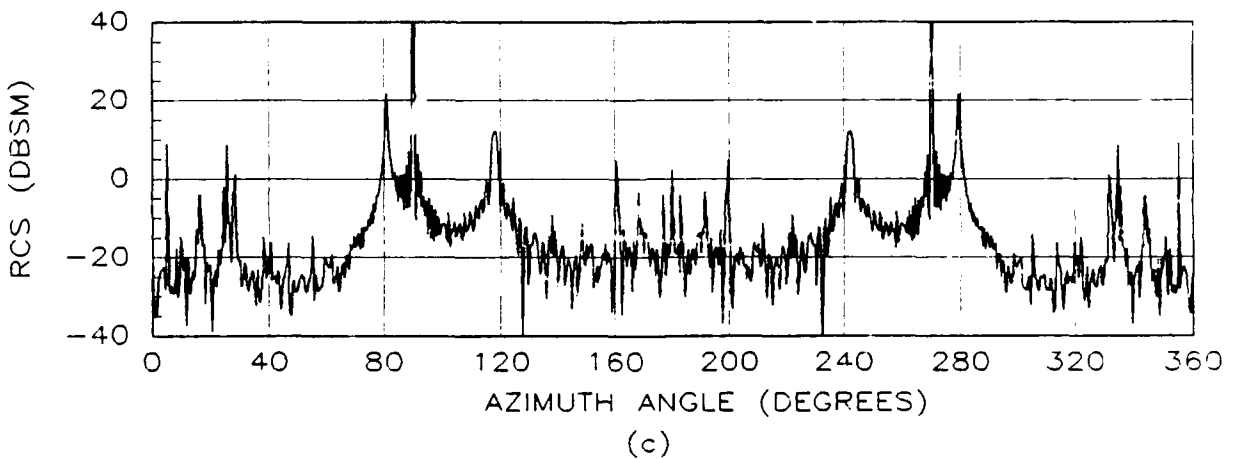
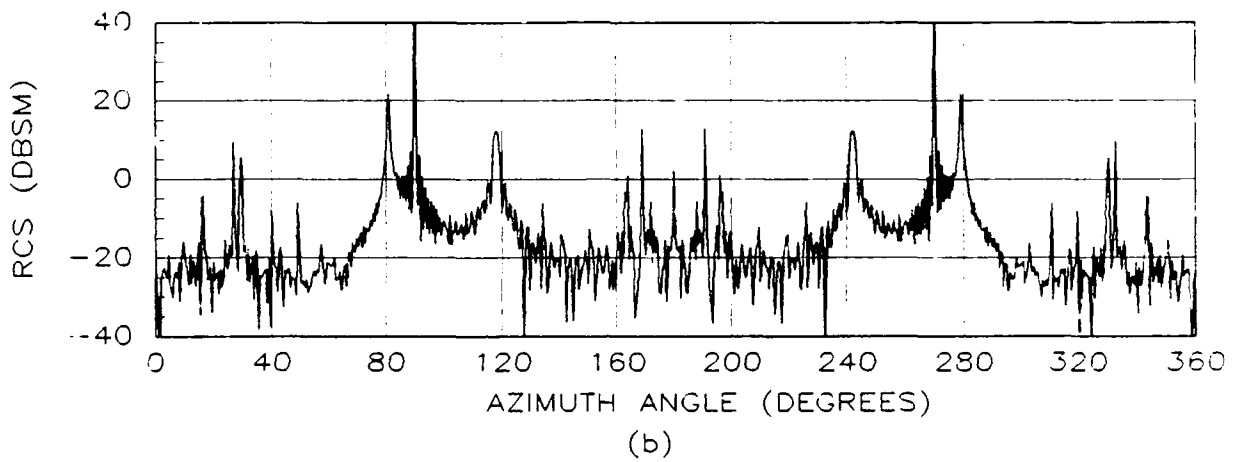
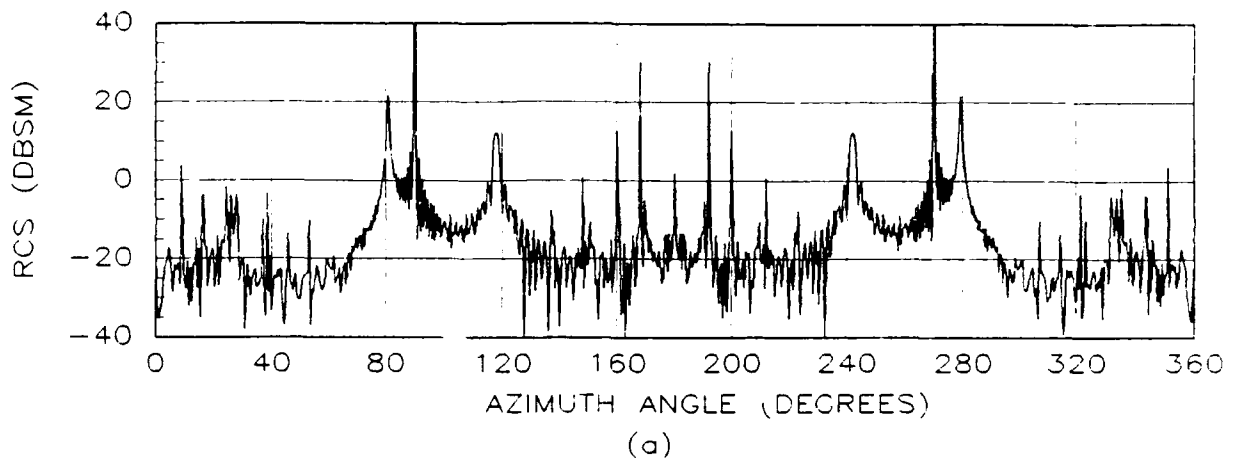
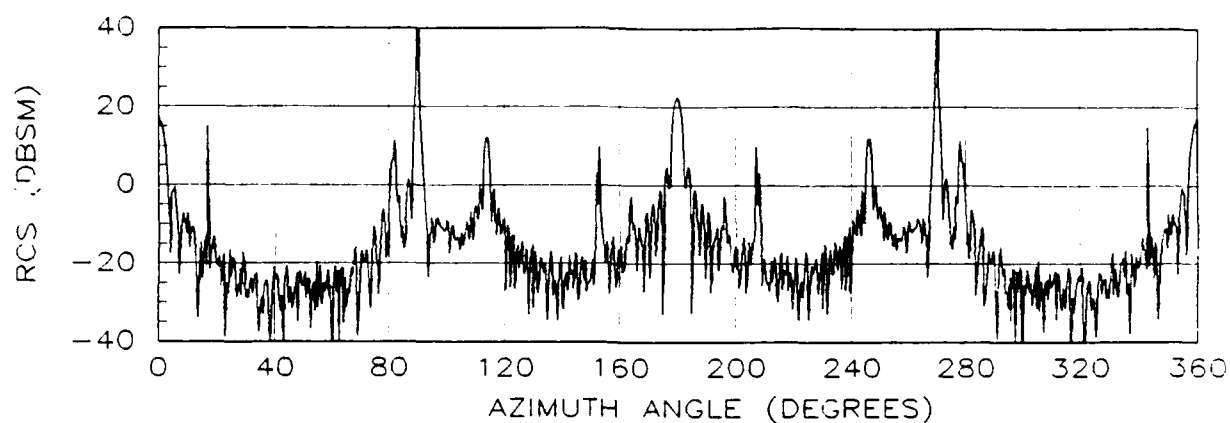
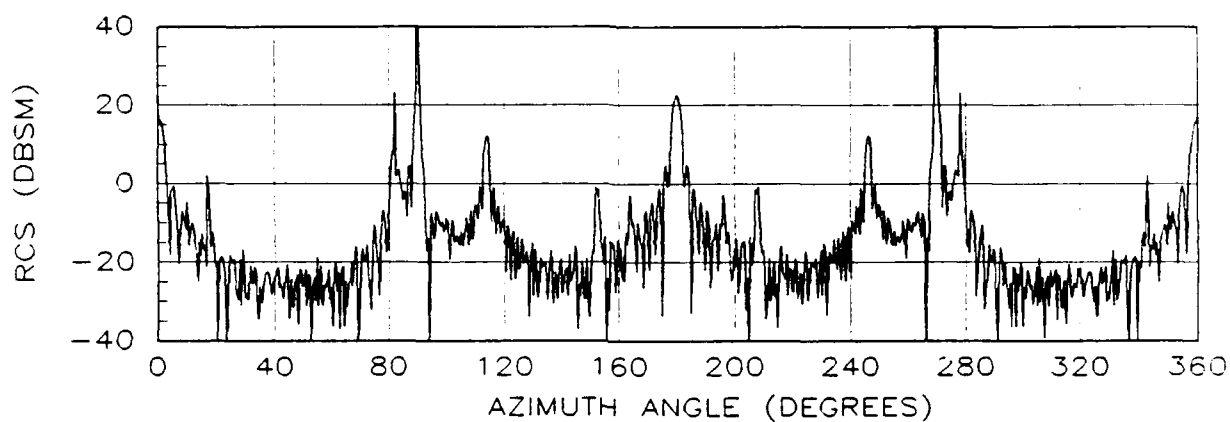


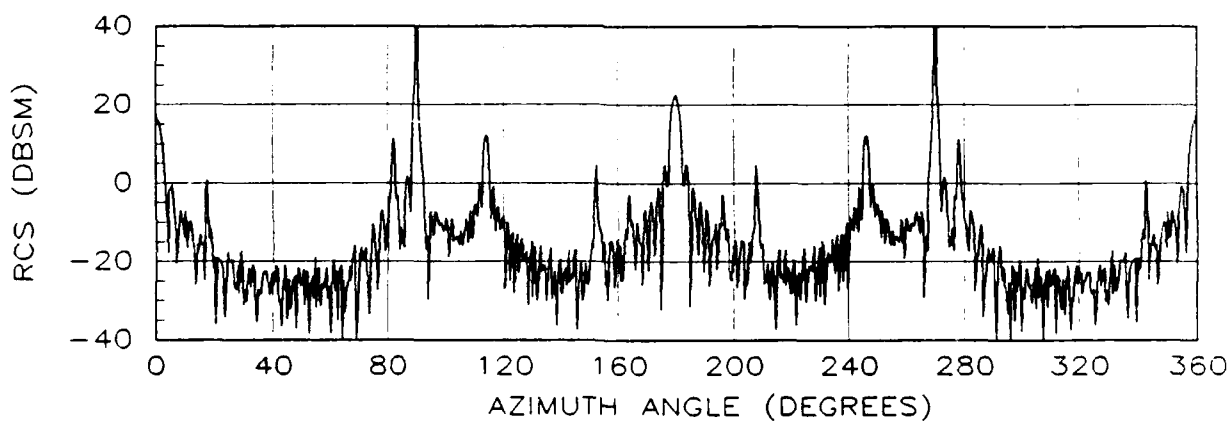
Figure D.7. Raw RCS of a C-5A Aircraft for: (a) Non-deformed Airframe, (b) PSM deformation, and (c) NSM deformation. -30 Degrees Elevation : Vertical Polarization



(a)

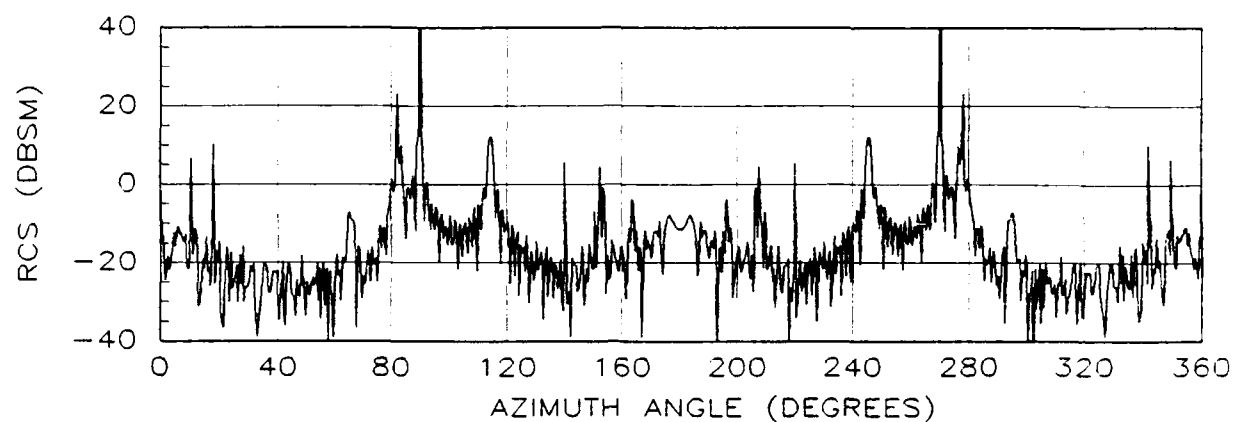


(b)

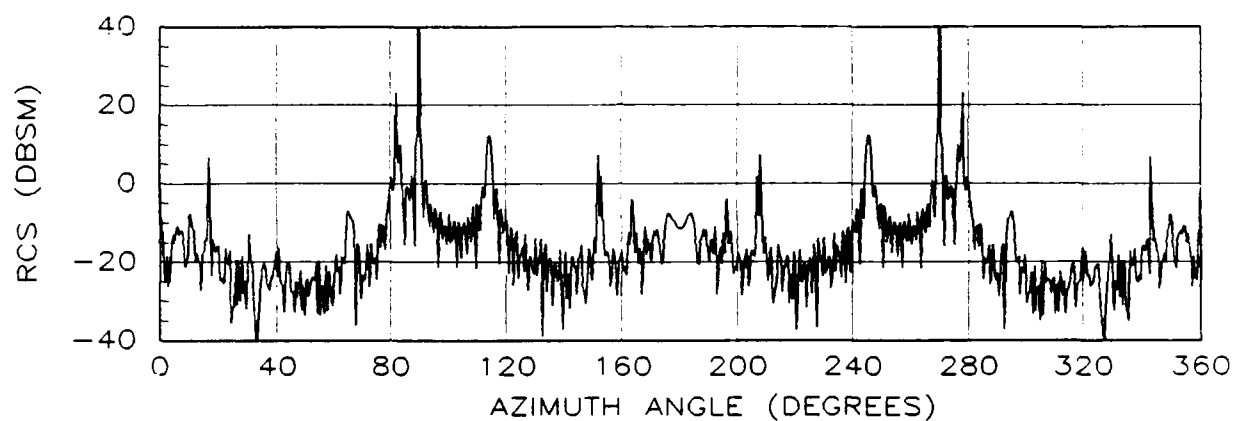


(c)

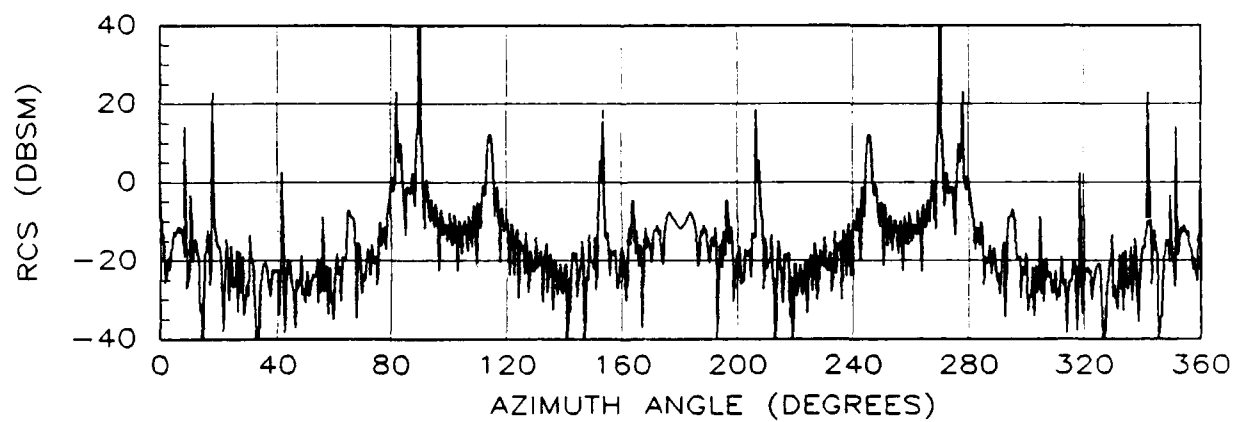
Figure D.8. Raw RCS of a C-5A Aircraft for: (a) Non-deformed Airframe, (b) PSM deformation, and (c) NSM deformation. 0 Degrees Elevation : Horizontal Polarization



(a)



(b)



(c)

Figure D.9. Raw RCS of a C-5A Aircraft for: (a) Non-deformed Airframe, (b) PSM deformation, and (c) NSM deformation. 10 Degrees Elevation : Horizontal Polarization

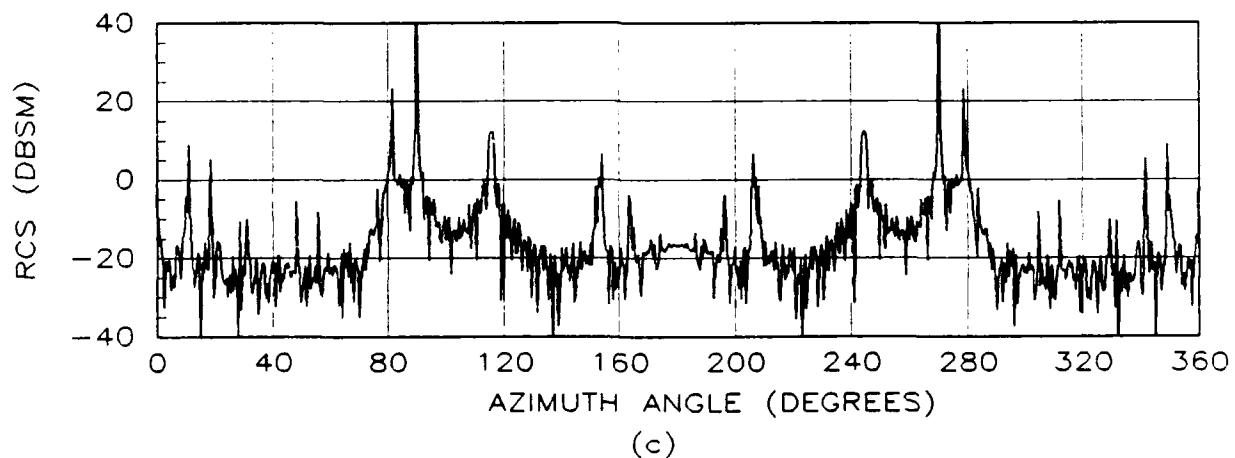
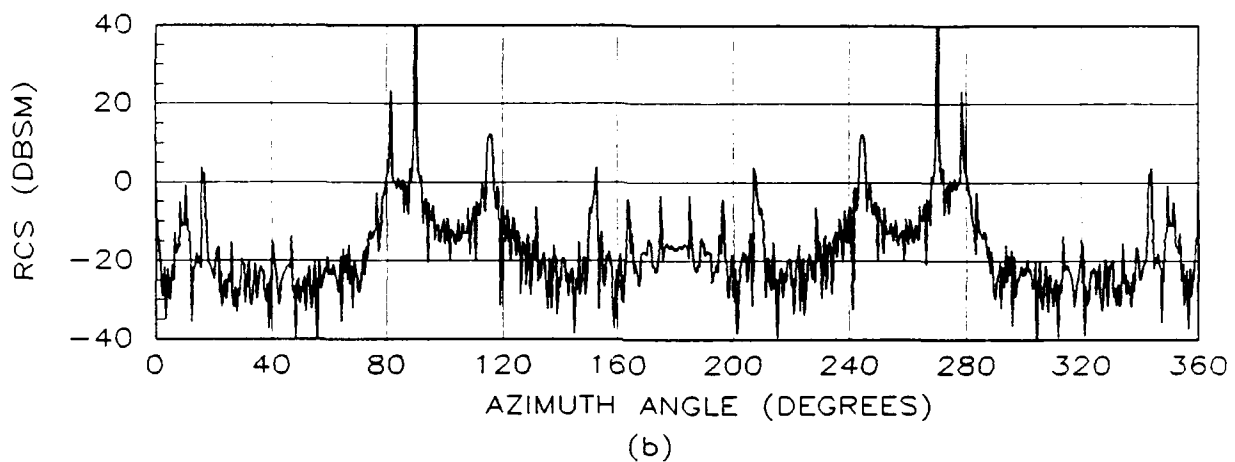
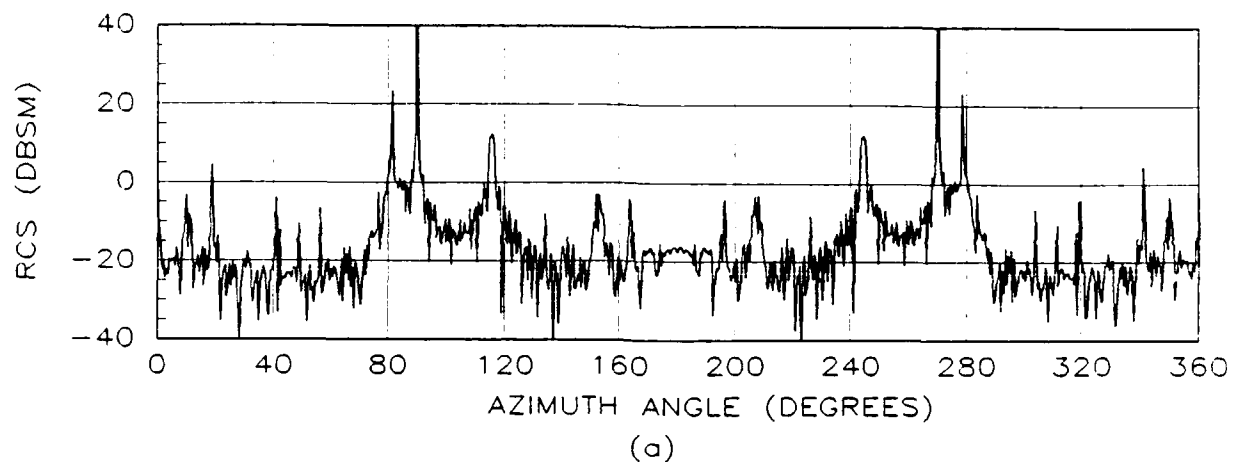


Figure D.10. Raw RCS of a C-5A Aircraft for: (a) Non-deformed Airframe, (b) PSM deformation, and (c) NSM deformation. 20 Degrees Elevation : Horizontal Polarization

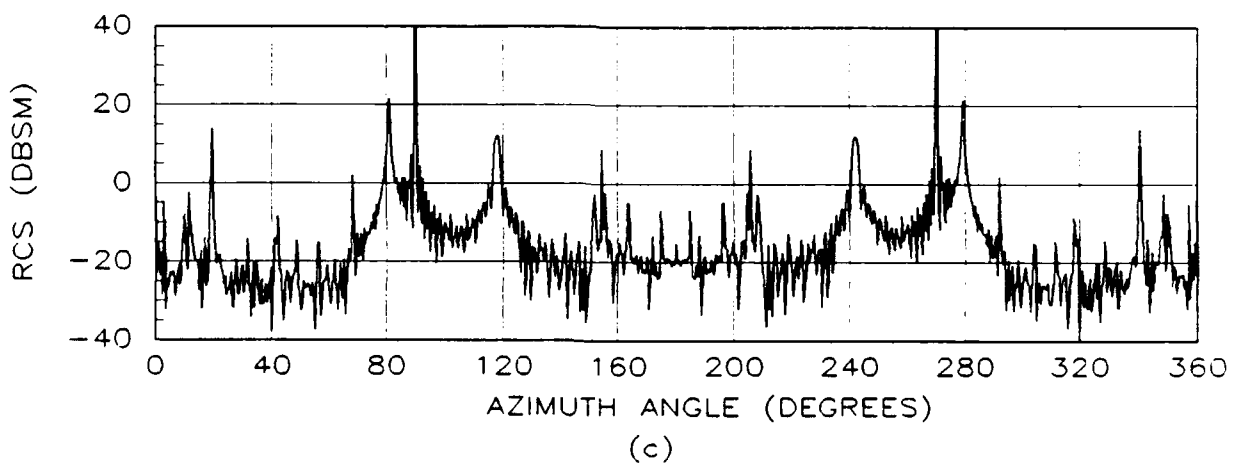
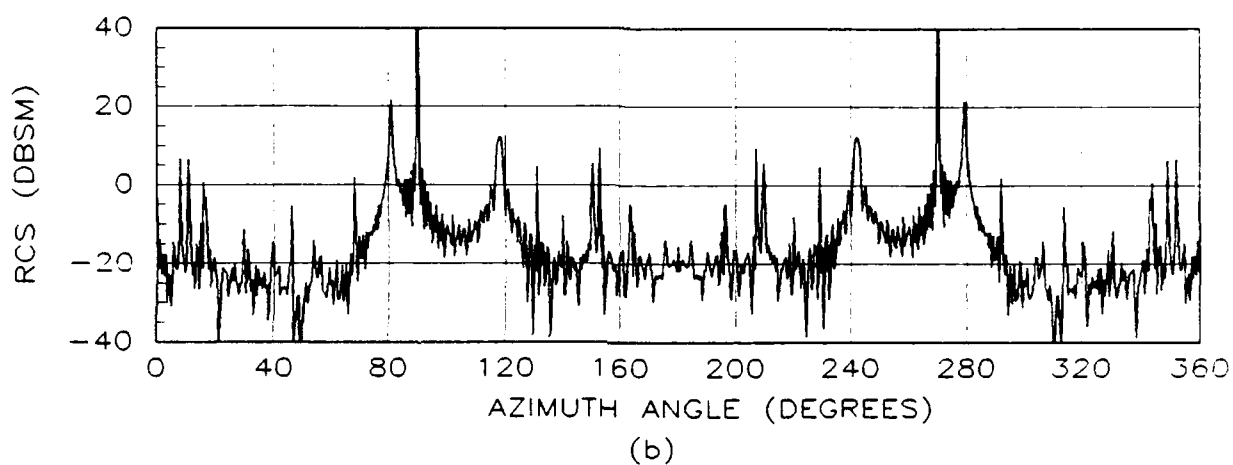
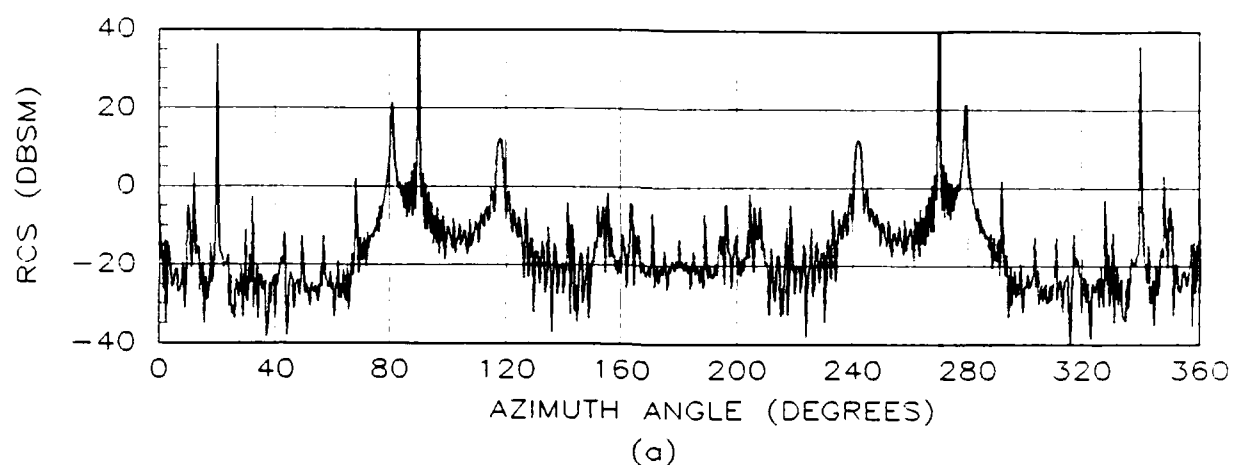
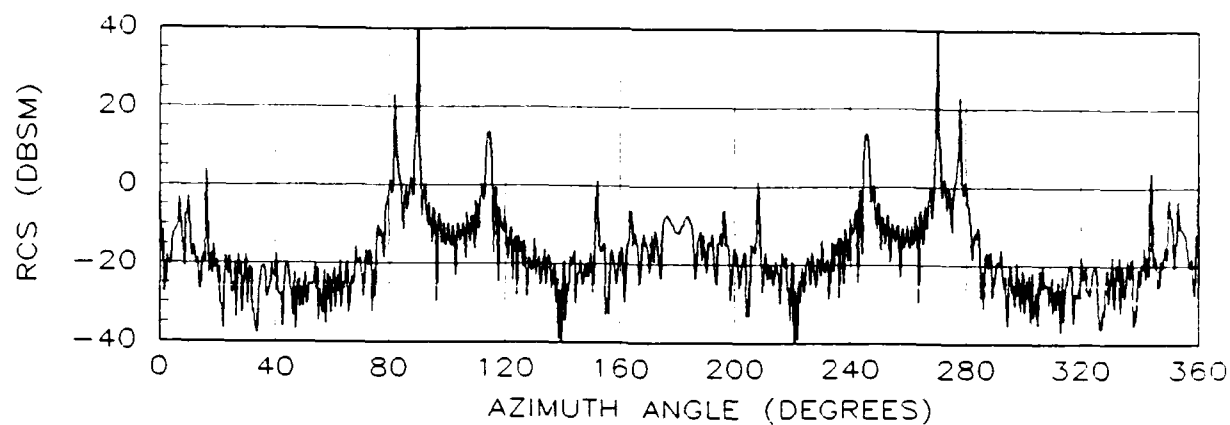
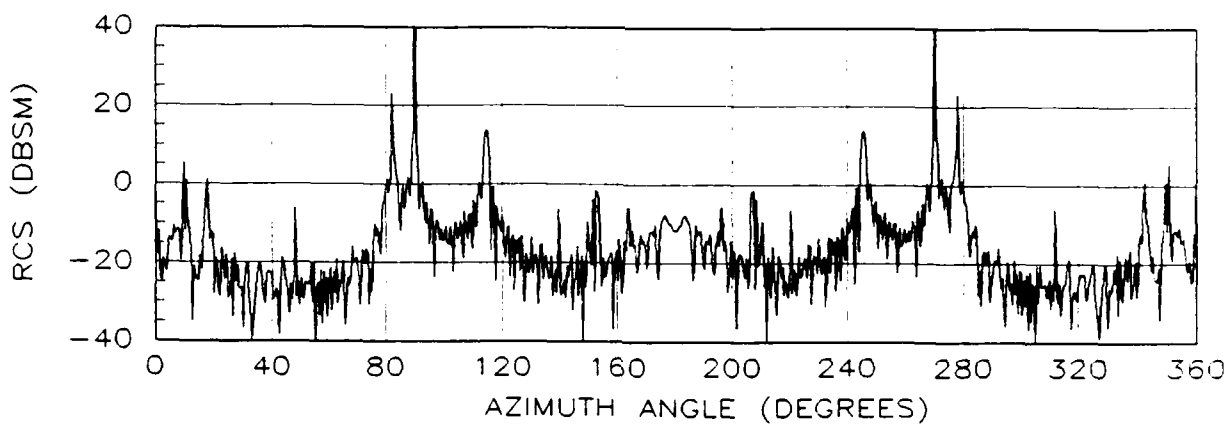


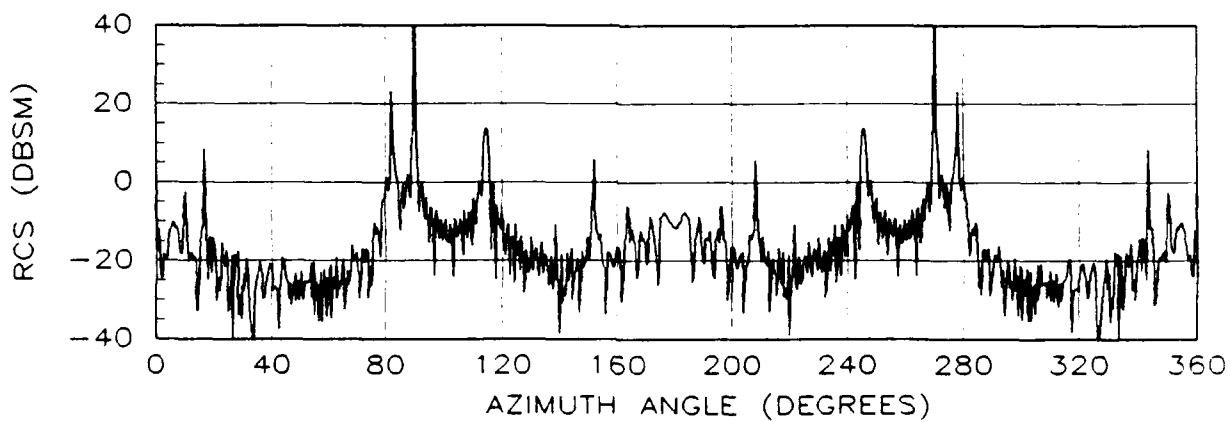
Figure D.11. Raw RCS of a C-5A Aircraft for: (a) Non-deformed Airframe, (b) PSM deformation, and (c) NSM deformation. 30 Degrees Elevation : Horizontal Polarization



(a)

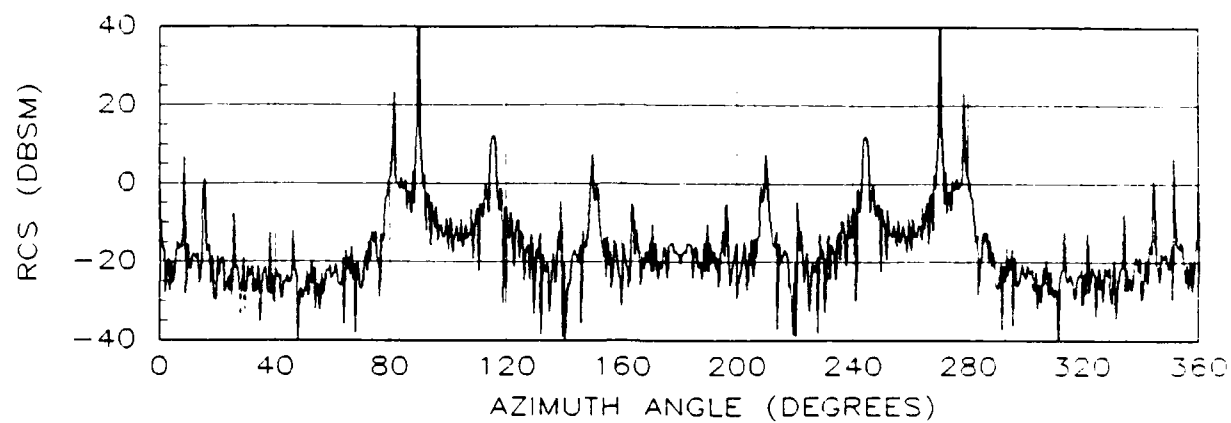


(b)

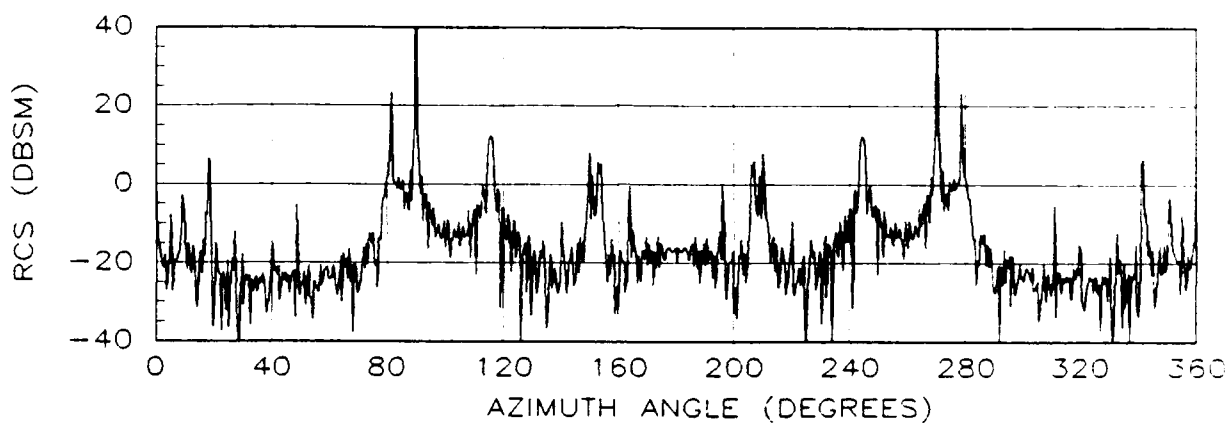


(c)

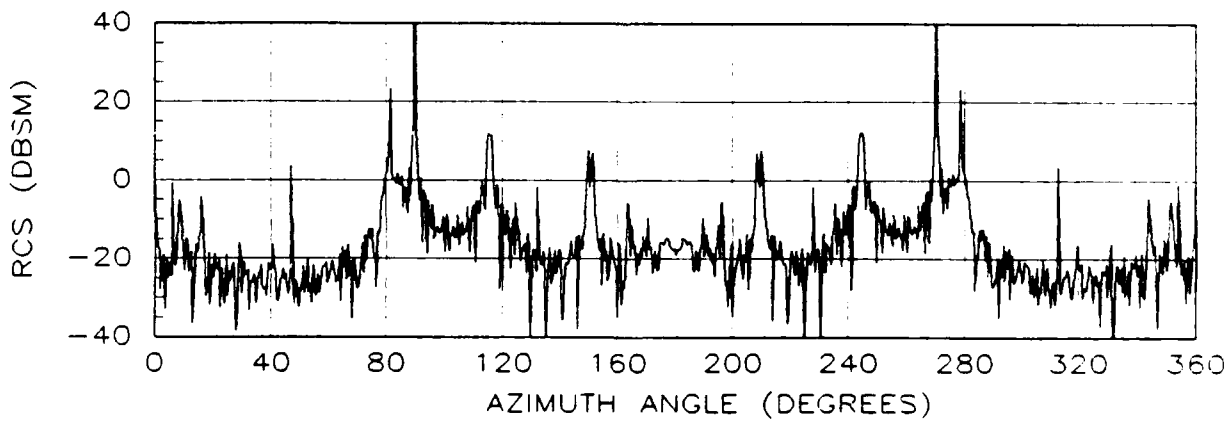
Figure D.12. Raw RCS of a C-5A Aircraft for: (a) Non-deformed Airframe, (b) PSM deformation, and (c) NSM deformation. -10 Degrees Elevation : Horizontal Polarization



(a)



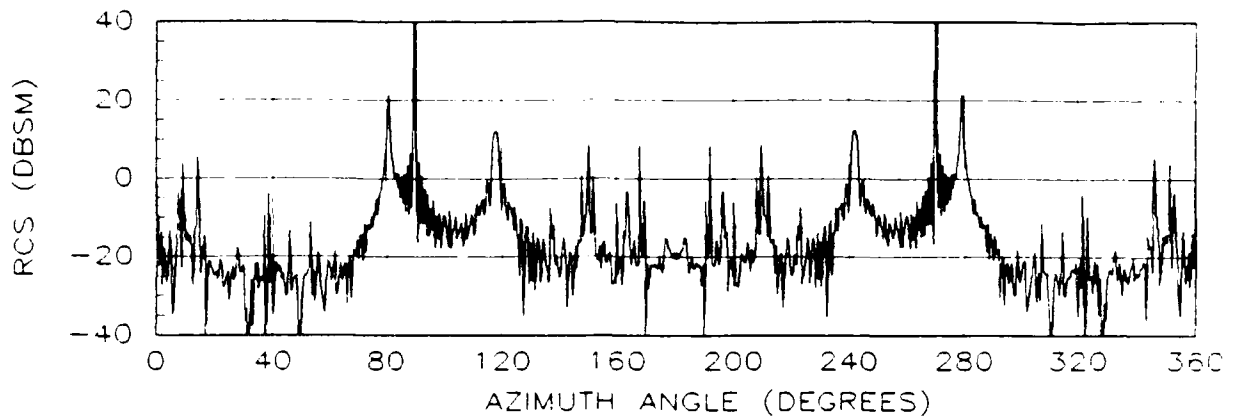
(b)



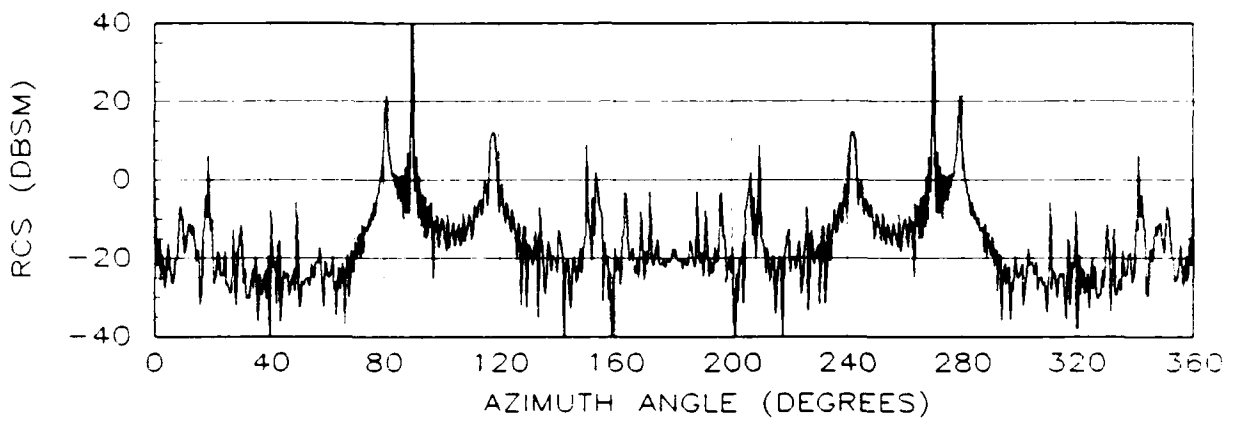
(c)

Figure D.13. Raw RCS of a C-5A Aircraft for: (a) Non-deformed Airframe, (b) PSM deformation, and (c) NSM deformation. -20 Degrees Elevation : Horizontal Polarization

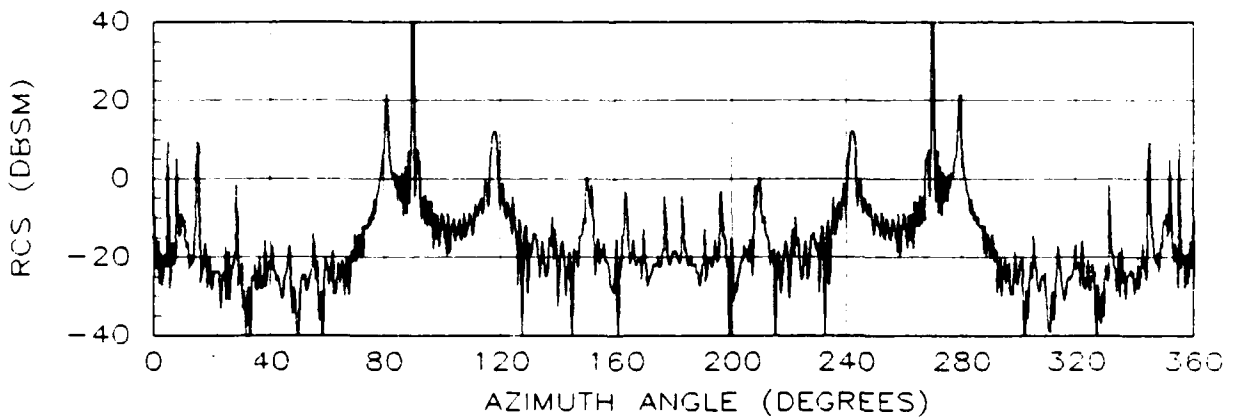




(a)



(b)



(c)

Figure D.14. Raw RCS of a C-5A Aircraft for: (a) Non-deformed Airframe, (b) PSM deformation, and (c) NSM deformation. -30 Degrees Elevation : Horizontal Polarization

## Bibliography

1. Beck, Capt Allan R. Investigation of Electromagnetic Scattering Effects From Aeroelastic Wing Deformations. MS Thesis, AFIT/GAE/AA/86D-1. School of Engineering, Air Force Institute of Technology (AU), Wright-Patterson AFB OH, December 1986.
2. Knott, Eugene F. "A Progression of High-Frequency RCS Prediction Techniques," Proceedings of the IEEE, 73: 252-264 (February 1985).
3. Youssef, Nazih N. "Radar Cross Section of Complex Targets," Proceedings of the IEEE, 77: 722-734 (May 1989).
4. Newman, Edward H. and Ronald J. Marhefka. "Overview of MM and UTD Methods at the Ohio State University," Proceedings of the IEEE, 77: 700-708 (May 1989).
5. Shankar, Vijaya, William R. Hall, and Alireza H. Mohammadian. "A Time-Domain Differential Solver for Electromagnetic Scattering Problems," Proceedings of the IEEE, 77: 709-721 (May 1989).
6. Taflov, Allen and Korada R. Umashankar. "Review of FD-TD Numerical Modeling of Electromagnetic Wave Scattering and Radar Cross Section," Proceedings of the IEEE, 77: 682-699 (May 1989).
7. Anderson, William J. Finite Element Method in Mechanical Design. Lecture Notes that Accompanied the Engineering Short Course "Finite Elements: Linear Static Analysis," The University of Michigan, Ann Arbor MI, June 1991.
8. Brauer, John R. What Every Engineer Should Know About Finite Element Analysis. New York and Basel: Marcel Dekker, Inc. 1988
9. MSC/NASTRAN Version 66. "Users Manual," The Macneal-Schwendler Corporation. 1988
10. Marhefka, Ronald J. Radar Cross Section - Basic Scattering Code, RCS-BSC (Version 2.0). Users Manual. Developed Under Government Contract F33615-86-K-1023 with the Ohio State University Electroscience Laboratory, Department of Engineering, Columbus OH, February 1990.
11. Keller, J. B. "Geometric Theory of Diffraction," Journal of the Optical Society of America, 52: 116-130 (February 1962).

12. Kouyoumjian R. G. and P. H. Pathak, "A Uniform Geometric Theory of Diffraction for an Edge in a Perfectly Conducting Surface," Proceedings of the IEEE, 62: 1448-1461 (November 1974).
13. Joseph, Phillip J. Class Notes Distributed in EENG 630, Electromagnetic Radiation and Scattering. School of Engineering, Air Force Institute of Technology (AU), Wright-Patterson AFB OH, January 1991.
14. Welsh, Bryon M. "Statistical Processing of Radar Cross Section Data," Presented at the Annual Joint Electronic Warfare Conference, Las Cruces NM. May 1985

REPORT DOCUMENTATION PAGE			Form Approved OMB No. 0704-0188	
1. AGENCY USE ONLY (Leave blank)		2. REPORT DATE December 1991	3. REPORT TYPE AND DATES COVERED Master's Thesis	
4. TITLE AND SUBTITLE Investigation of the Effects of Aeroelastic Deformations on the Radar Cross Section of Aircraft			5. FUNDING NUMBERS	
6. AUTHOR(s) Samuel D. McKenzie, Capt, USAF				
7. AUTHORING OR MONITORING AGENCY NAME(S) AND ADDRESS(ES) Air Force Institute of Technology, WPAFB OH 45433-6583			8. PERFORMING ORGANIZATION REPORT NUMBER AFIT/GE/ENG/91D-40	
9. PERFORMING ORGANIZATION MONITORING AGENCY NAME(S) AND ADDRESS(ES) 6585th Test Group/RX Holoman AFB NM, 88330-5000			10. PERFORMING ORGANIZATION REPORT NUMBER	
11. SUPPLEMENTARY NOTES				
12a. DISTRIBUTION AVAILABILITY STATEMENT Approved for Public Release; Distribution Unlimited			12b. DISTRIBUTION STATEMENT	
13. ABSTRACT (Maximum 200 words) The effects of aeroelastic deformations on the radar cross section (RCS) of a T-38 trainer jet and a C-5A transport aircraft are examined and characterized. Realistic representations of structural wing deformations are obtained from a mechanical/computer aided design software package called "NASTRAN". NASTRAN is used to evaluate the structural parameters of the aircraft as well as the restraints and loads associated with realistic flight conditions. Geometries for both the non-deformed and deformed airframes are obtained from the NASTRAN models and translated into RCS models. The RCS is analyzed using a numerical modeling code called the "Radar Cross Section - Basic Scattering Code, version 2" which was developed at the Ohio State University and is based on the uniform geometric theory of diffraction. The code is used to analyze the effects of aeroelastic deformations on the RCS of the aircraft by comparing the computed RCS representing the deformed airframe to that of the non-deformed airframe and characterizing the differences between them.				
14. SUBJECT TERMS radar, radar cross section, electromagnetic scattering, aircraft, aeroelastic deformations			15. NUMBER OF PAGES 131	
			16. PRICE CODE	
17. SECURITY CLASSIFICATION OF REPORT Unclassified	18. SECURITY CLASSIFICATION OF THIS PAGE Unclassified	19. SECURITY CLASSIFICATION OF ABSTRACT Unclassified	20. LIMITATION OF ABSTRACT UL	